



Max-Planck-Institut für Intelligente Systeme
(ehemals Max-Planck-Institut für Metallforschung)
Stuttgart

Nitriding of Fe-Mo Alloys and Maraging Steel: Structure, Morphology and Kinetics of Nitride Precipitation

Holger Selg

Dissertation
an der
Universität Stuttgart

Bericht Nr. 242
November 2012

Nitriding of Fe-Mo Alloys and Maraging Steel: Structure, Morphology and Kinetics of Nitride Precipitation

Von der Fakultät Chemie der Universität Stuttgart zur Erlangung der
Würde eines Doktors der Naturwissenschaften (Dr. rer. nat.)
genehmigte Abhandlung

vorgelegt von

Holger Selg

aus Riedlingen/Donau

Hauptberichter: Prof. Dr. Ir. E. J. Mittemeijer

Mitberichter: Prof. Dr. J. Bill

Prüfungsvorsitzender: Prof. Dr. T. Schleid

Tag der Einreichung: 04.09.2012

Tag der mündlichen Prüfung: 12.11.2012

MAX-PLANCK-INSTITUT FÜR INTELLIGENTE SYSTEME, STUTTGART
(ehemals MAX-PLANCK-INSTITUT FÜR METALLFORSCHUNG)
INSTITUT FÜR MATERIALWISSENSCHAFT DER UNIVERSITÄT STUTTGART

Contents

1.	Introduction.....	7
1.1	Nitriding.....	7
1.2	Gaseous nitriding	8
1.2.1	Thermodynamics of gas nitriding.....	10
1.3	The microstructure of the nitrided zone.....	12
1.4	Nitriding of Fe-Me alloys.....	15
1.5	Excess nitrogen.....	17
1.6	Residual stress.....	20
1.7	Maraging steels	22
1.8	Outlook of the thesis.....	23
2.	Molybdenum-nitride precipitation in recrystallized and cold rolled Fe-1at.% Mo alloy.....	27
2.1	Introduction.....	28
2.2	Experimental	30
2.2.1	Specimen preparation.....	30
2.2.2	Nitriding.....	31
2.2.3	Specimen characterization.....	32
2.3	Results and discussion.....	34
2.3.1	Recrystallized specimens.....	34
2.3.2	Cold rolled specimens	51
2.4	Conclusions.....	57
3.	Defect-dependent nitride surface-layer development upon nitriding of Fe-1 at.% Mo alloys	59
3.1	Introduction.....	60
3.2	Experimental	61
3.2.1	Specimen preparation.....	61
3.2.2	Nitriding.....	62
3.2.3	Specimen characterization.....	62
3.3	Cold rolled specimens; results and discussion.....	65
3.3.1	X-ray diffraction; phase analysis	65
3.3.2	Microstructure; growth of the γ' -Fe ₄ N _{1-x} layer	68
3.3.3	γ' -nitride layer-growth kinetics	72

Content

3.4	Recrystallized specimens; results and discussion	78
3.4.1	X-ray diffraction – phase analysis	78
3.4.2	Occurrence of plate-like morphology of the γ' phase; the role of dissolved Mo	84
3.4.3	Orientation relationship γ' nitride/ferrite.....	93
3.5	Conclusions.....	97
4.	Microstructural and surface residual stress development during low-temperature gaseous nitriding of Fe-3.07at.%Mo alloy	99
4.1	Introduction.....	100
4.2	Experimental	101
4.2.1	Specimen preparation.....	101
4.2.2	Nitriding.....	102
4.2.3	Specimen characterization.....	102
4.3	Results and discussion.....	104
4.3.1	Microstructure	104
4.3.2	Concentration-depth and microhardness-depth profiles.....	108
4.3.3	Residual macrostress.....	111
4.4	Conclusion	113
5.	Nitriding behaviour of maraging steel: experiments and modelling	116
5.1	Introduction.....	116
5.2	Modelling the kinetics of growth of the nitrided zone	117
5.3	Experimental	121
5.3.1	Specimen preparation.....	121
5.3.2	Nitriding.....	122
5.3.3	Determination of nitrogen-absorption isotherms	123
5.3.4	Specimen characterization.....	125
5.4	Results and discussion.....	127
5.4.1	Nitrogen-absorption isotherms.....	127
5.4.2	Nitriding of solution annealed maraging steel (specimens “A”)..	131
5.4.3	Nitriding of age-hardened maraging steel (specimens “B”)	141

5.5	Final remarks on the difference in nitriding response of solution annealed (“A”) and age-hardened (“B”) specimens	151
5.6	Conclusions.....	152
5.7	Acknowledgement	153
6.	Summary.....	155
6.1	Introduction.....	155
6.2	Experimental	156
6.3	Nitriding.....	157
6.4	Specimen characterization.....	157
6.5	Results	158
6.5.1	Molybdenum-nitride precipitation in recrystallized and cold rolled Fe-1at.% Mo alloy	158
6.5.2	Defect-dependent nitride surface-layer development upon nitriding of Fe-1 at.% Mo alloys	159
6.5.3	Microstructural and surface residual stress development during low-temperature gaseous nitriding of Fe-3.07at.% Mo alloy	160
6.5.4	Nitriding behaviour of maraging steel: experiment and modelling.....	161
7.	Zusammenfassung.....	163
7.1	Einleitung.....	163
7.2	Experimentaltteil	164
7.3	Nitrieren	165
7.4	Probencharakterisierung.....	165
7.5	Ergebnisse	166
7.5.1	Molybdänitrid-Ausscheidungen in rekristallisierter und kalt gewalzter Fe-1at.% Mo-Legierung	166
7.5.2	Defekt-abhängige Bildung nitrierter Oberflächenschichten beim Nitrieren von Fe-1at.% Mo Legierungen.....	167
7.5.3	Entwicklung der Mikrostruktur und Oberflächen-Eigen- spannungen beim Niedertemperatur-Nitrieren einer Fe-3,07at.% Mo Legierung	169
7.5.4	Nitrierverhalten von Maragingstählen: Experiment und Modellierung.....	169

Content

CHAPTER 1

Introduction

The increasing demand for advanced materials along with the necessity to improve the (surface-) properties of such materials often requires appropriate thermochemical surface treatments. These treatments involve the simultaneous diffusion of interstitial elements such as nitrogen and/or carbon into the surface of the specimen during processing. Among them, nitriding, carburizing and nitrocarburizing are one of the most important treatments to improve the surface properties of materials, such as resistance to wear, fatigue and corrosion properties, while the core of the material is not (deliberately) affected. Thus, a core-shell like (micro-)structure results with largely improved surface properties (as this is usually the most affected location of loading and thus requires higher hardness) and a ductile and tough core (to bear impact loads).

Although these surface heat treatments are often employed in practical applications in industry, there is still a lack of fundamental understanding of the underlying processes. This is based on the use of technical steels containing several (nitride forming-) alloying elements which lead to complex reactions and interactions between the inwardly diffusing species (such as N or C) with the alloying elements. Thus, for relatively simple binary [1-4] and ternary iron-based alloys [5-7], fundamental studies have been carried out to understand the mechanism of the underlying change in substrate microstructure.

1.1 Nitriding

Nitriding is the most widely applied thermochemical surface treatment to improve the surface mechanical (e.g. wear and fatigue) and chemical (corrosion) properties of iron-based workpieces. Nitriding is usually performed at temperatures ranging from 400 °C to 580 °C. Thus, no phase transition of the ferrite matrix occurs (as the maximum nitriding temperature is kept below the Ac1 temperature of steel) as compared to the ferrite-austenite transition (followed by martensite/bainite transformation) occurring

upon hardening. This is also one of the reasons for the large applicability of nitriding in industrial practice as the absence of such matrix-phase transformations only yields to minimum distortions and therefore to a very good control of the workpiece dimensions. One of the major advantages of nitriding as compared to carburizing is thus the low demand of post-machining treatments due to the occurrence of only minor dimensional changes upon nitriding.

Typical nitriding steels are low to medium carbon containing steels alloyed with nitride forming elements such as Al, Ti, V, Cr, and Mo. These elements can form nitrides in the ferrite matrix resulting in improved surface properties.

Upon nitriding, nitrogen is introduced in the surface of the iron-based workpiece through a nitrogen donating species. Nitriding can be performed in plasma (plasma nitriding), gas phase (gaseous nitriding) and liquid phase (salt bath nitrocarburizing, i.e. nitrogen *and* carbon are imposed simultaneously).

Gaseous nitriding is the only nitriding method that allows a precise process control of the nitrogen uptake via the chemical potential of nitrogen in the gas phase (see sec. 1.2).

1.2 Gaseous nitriding

Gas nitriding is usually carried out in ammonia/hydrogen gas mixtures at atmospheric pressure. The nitrogen donating species, ammonia, dissociates catalytically at the surface of the workpiece leading to atomic nitrogen diffusing into the ferrite matrix.

The gaseous nitriding treatments were carried out in pure ammonia (99.998 vol.%) and pure hydrogen (99.999 vol.%) gas. In order to keep the nitrogen activity in the gas phase constant during the heat treatment, it is indispensable to control the flow of the gases precisely and to ensure that within the furnace, no changes in the chemical composition of the gas phase occurs. To this end, a total gas flow rate of 500 ml/min was used corresponding to a linear gas velocity of 13.5 mm/s for the furnace used in the present work (see Fig. 1.1). The nitriding facility is schematically shown in Fig. 1.1 and consists of

a vertical, multizone quartz-tube furnace (diameter: 28 mm) with a temperature accuracy of ± 1 K (within each of the three zones). The nitriding gas mixture is adjusted by mass-flow controllers (one for each gas component). The nitriding sample is suspended to the sample rod by a quartz fibre, which is broken mechanically to terminate the nitriding process and the sample falls through an opened valve into the quenching bottle filled with water (and flushed with nitrogen in order to avoid oxidation of the sample upon quenching).

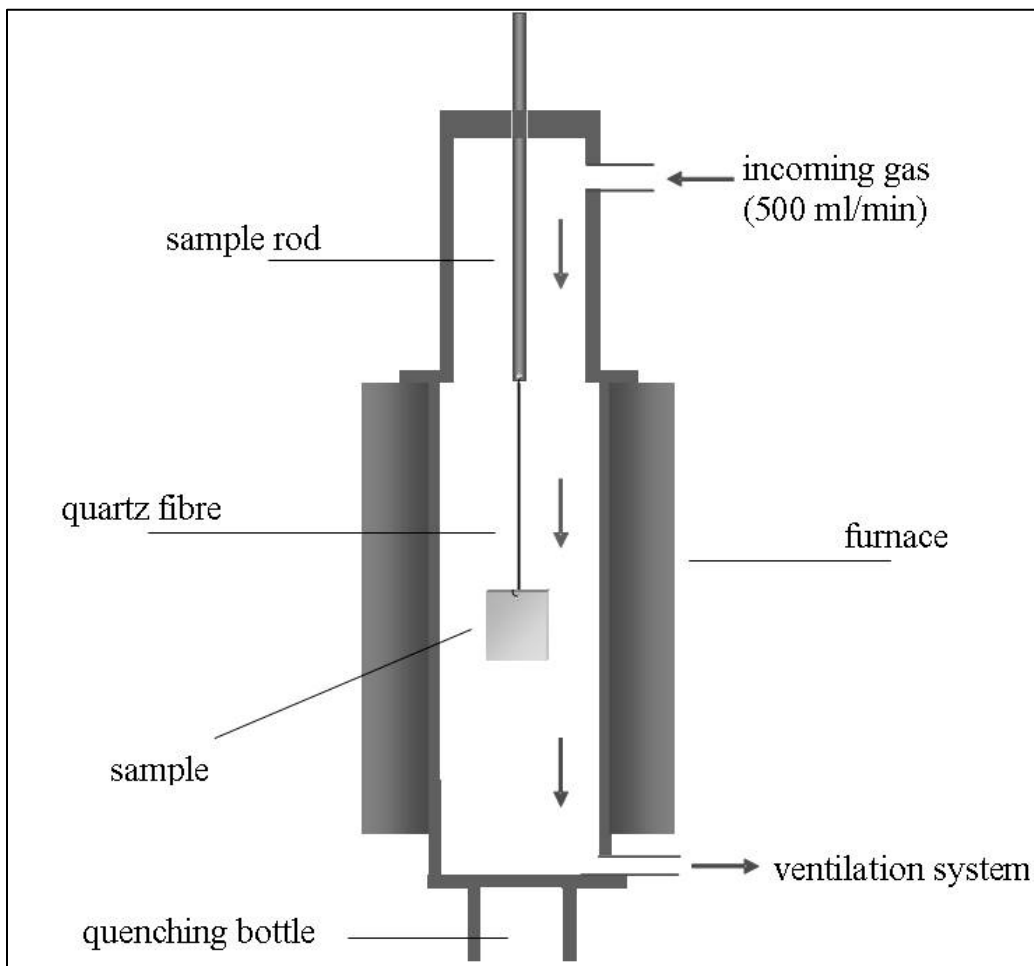


Fig. 1.1: Schematic illustration of the vertical quartz-tube furnace (diameter: 28 mm) used for gaseous nitriding. Individual mass-flow controller for each gas component adjust the composition of the incoming gas. The sample is suspended with a quartz fibre to the sample rod and mechanically broken to terminate the nitriding process.

1.2.1 Thermodynamics of gas nitriding

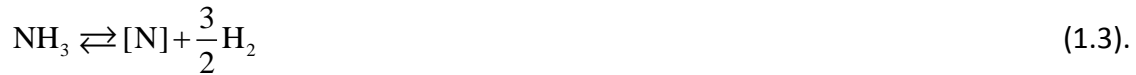
As described above, gas nitriding is usually performed in ammonia/hydrogen gas mixtures. This process can be regarded as the sum of the following hypothetical reactions, as the Gibbs free energy (and therefore the chemical potential) is a state variable and thus, the value of the Gibbs free energy is independent of the route taken to reach a particular state.

To this end, nitriding in ammonia/hydrogen gas mixtures can formally be conceived as the sum of the following reactions [8, 9]



with [N] representing nitrogen dissolved in the matrix.

Combining reactions (1.1) and (1.2) yields to



Under the assumption of local equilibrium between the nitriding atmosphere and the specimen's surface, the (hypothetical) pressure of N_2 gas can be calculated from the equilibrium (1.2) as follows:

$$p_{\text{N}_2}^{1/2} = K^{(2)} p_{\text{NH}_3} / p_{\text{H}_2}^{3/2} \quad (1.4)$$

where p_{NH_3} and p_{H_2} denote the partial pressures of ammonia and hydrogen, respectively and $K^{(2)}$ is the equilibrium constant for reaction (1.2).

The equilibrium condition between the gas phase and the surface of the specimen requires

$$\frac{1}{2} \mu_{\text{N}_2, \text{g}} = \mu_{\text{N}, \text{s}} \quad (1.5)$$

with the chemical potential μ of nitrogen in the gas phase and (dissolved) in the matrix, respectively. This thermodynamic equilibrium implies that the flow rate of the ammonia/hydrogen gas mixture is high enough in order to avoid both the thermal

decomposition of ammonia (Eq. 1.2) as well as the recombination of nitrogen (according to Eq. 1.1) at the specimen's surface [8, 9].

With the definition of the chemical potential it follows that

$$\frac{1}{2} \mu_{N_2,g}^0 + \frac{1}{2} RT \ln \left(p_{N_2} / p_{N_2}^0 \right) = \mu_{N,s}^0 + RT \ln a_N \quad (1.6)$$

If an the same reference state for nitrogen in the gas phase and the solid is selected, the activity of nitrogen, a_N , is then given by

$$a_N = p_{N_2}^{1/2} / \left(p_{N_2}^0 \right)^{1/2} \quad (1.7)$$

With Eq. (1.1) and (1.2) the activity of nitrogen can be expressed as

$$a_N = K^{(3)} \left(p_{NH_3} / p_{H_2}^{3/2} \right) = K^{(3)} r_N \quad (1.8)$$

where r_N denotes the nitriding potential.

Hence, the activity of nitrogen at a given temperature depends on the applied nitriding potential.

Considering the usual nitriding temperatures (450 - 590 °C), it becomes clear that the activity of nitrogen can be much larger than 1 (Eq. 1.8). Therefore, (hypothetical) pressures of several thousands of atmospheres would be required to cause the same activity of nitrogen when using nitrogen gas instead of ammonia and hydrogen gas mixtures (note the square root dependence of activity and pressure in Eq. 1.7). From this it follows that pure nitrogen gas is not suitable to use as nitrogen donating atmosphere.

With the help of (calibrated) mass flow controllers, the desired nitriding potential can be set in the gas nitriding furnace. This feature makes gas nitriding to a unique, well-controllable process as the desired microstructure can be set by selecting appropriate process conditions. This is essential to obtain optimal properties for gas nitrided components.

1.3 The microstructure of the nitrided zone

By choosing appropriate nitriding conditions (temperature and nitriding potential) any phase shown in the Fe-N phase diagram (Fig. 1.2) can be produced at the surface of an iron specimen. The phase γ' -Fe₄N_{1-x} has a quite narrow homogeneity range, whereas the ϵ -Fe₃N_{1+y} phase exists within a broad compositional range. In order to avoid the formation of austenite upon nitriding, the temperature is usually kept below 592 °C.

The equilibrium phases at the surface between a pure α -Fe specimen and the gas phase consisting of an ammonia and hydrogen gas mixture have been determined by Lehrer [10]. In the so-called Lehrer diagram, the borders of the phase fields are drawn as a function of nitriding potential and temperature (see Fig. 1.3). In this diagram, besides the phase boundaries, iso-concentration lines have been indicated [11].

The microstructure of the nitrided zone that develops upon nitriding a pure iron specimen under conditions thermodynamically allowing the formation of ϵ -Fe₃N_{1+y} (i.e. a combination of temperature and nitriding potential lying in the ϵ -phase field of the Lehrer diagram, cf. Fig. 1.3) is schematically drawn in Fig. 1.4. Directly at the surface, a so-called compound layer develops consisting of iron nitrides. This layer, which is also known as “white layer” due to its appearance in the microscope after metallographic etching (with Nital) can be subdivided into an ϵ -Fe₃N_{1+y}-layer (Fe atoms are arranged in a hcp-structure, N occupies the octahedral sites in an ordered manner; in the following referred to as ϵ) and a γ' -Fe₄N_{1-x}-layer underneath (with Fe atoms being arranged in a fcc-structure and N atoms orderly occupying the octahedral interstitial sites; in the following referred to as γ'). Beneath the compound layer, the so-called diffusion zone develops upon nitriding in which nitrogen is dissolved interstitially in the octahedral sites of the bcc matrix. Upon cooling and subsequent aging, α'' -Fe₁₆N₂ (iron atoms are arranged in a bct-structure with N occupying the octahedral interstices in an ordered manner) and γ' can precipitate as (small) needles. The compound layer and the diffusion zone together are called “nitrided zone”.

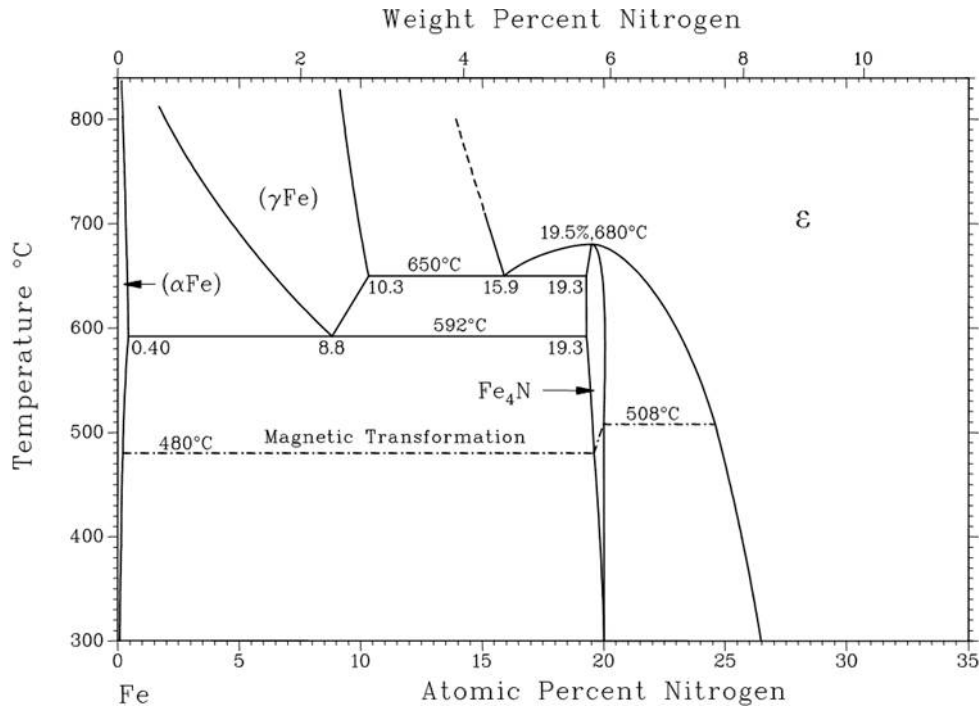


Fig. 1.2: Part of the (metastable) binary Fe-N phase diagram redrawn according to Ref. [12].

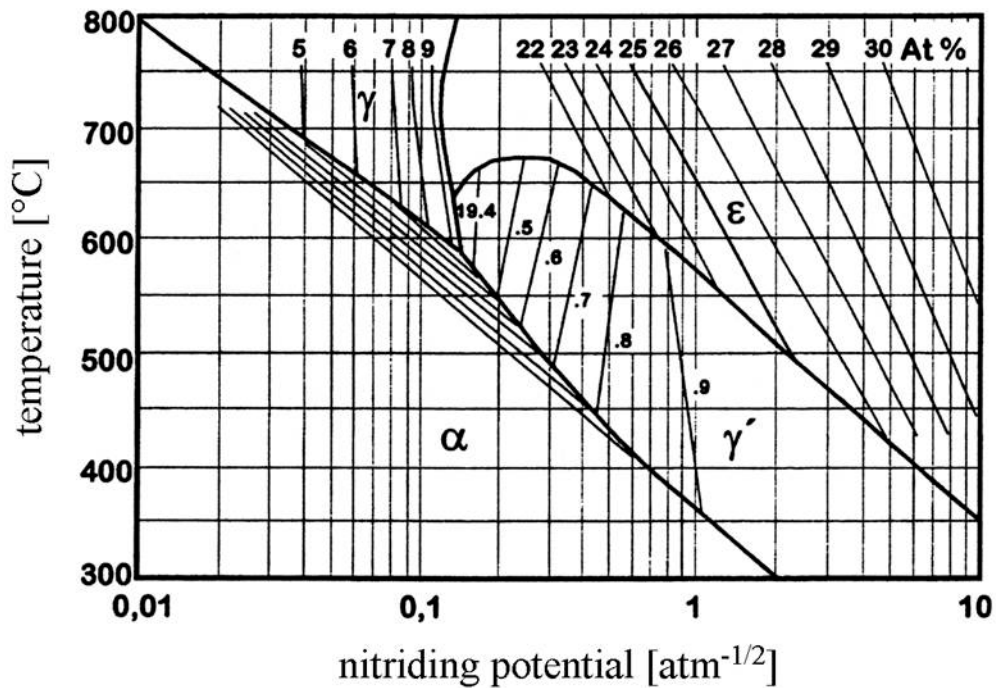


Fig. 1.3: Extended Lehrer diagram [11] showing the phase in equilibrium with the gas atmosphere upon nitriding of pure iron as a function of temperature and nitriding potential. In addition to the phase boundaries, the corresponding iso-concentration lines within a phase are indicated.

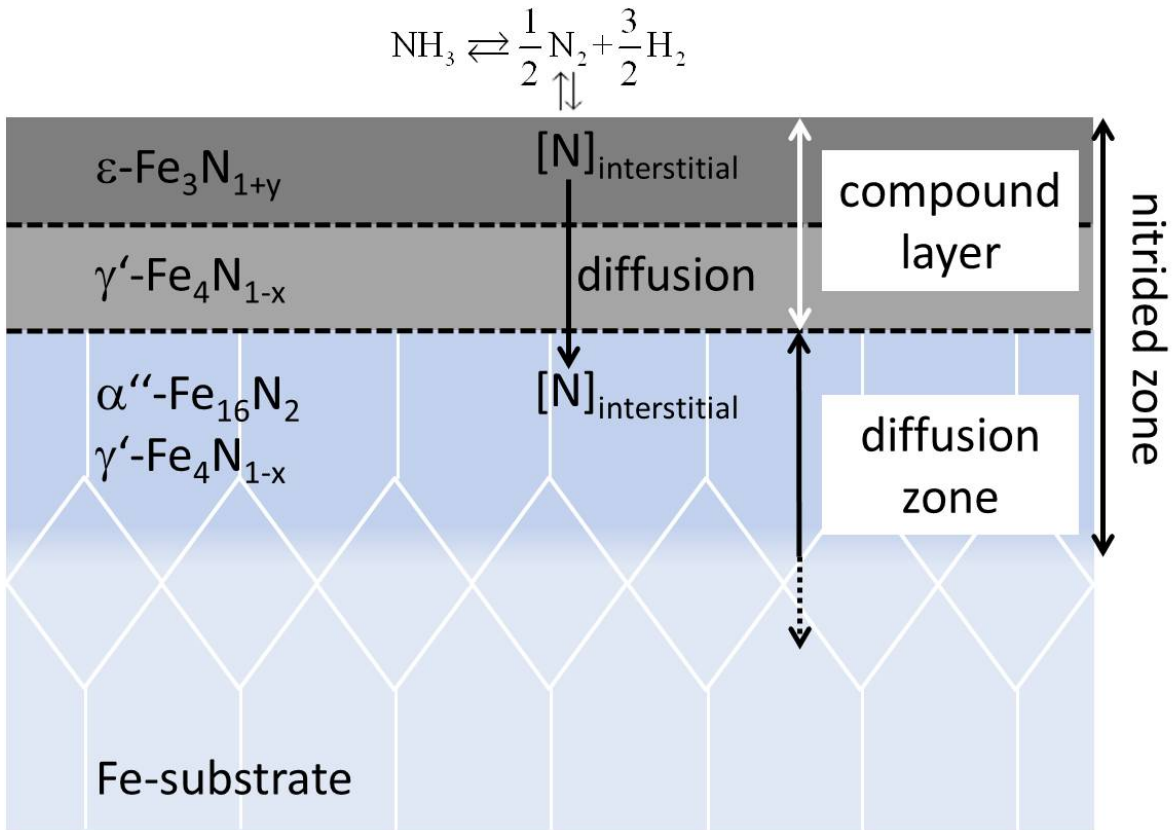


Fig. 1.4: Schematic illustration of the microstructure developing upon nitriding a pure Fe-specimen in the ϵ -region of the Lehrer diagram. The nitrided layer consists of the surface-adjacent compound layer (can be subdivided into $\epsilon\text{-Fe}_3\text{N}_{1+y}$ and $\gamma'\text{-Fe}_4\text{N}_{1-x}$) and the diffusion zone underneath, where N dissolves interstitially and may be precipitated as $\alpha''\text{-Fe}_{16}\text{N}_2$, or $\gamma'\text{-Fe}_4\text{N}_{1-x}$.

1.4 Nitriding of Fe-Me alloys

In case of nitriding of Fe-Me alloys containing one or more nitride forming elements (=Me) such as Al [1, 4, 13, 14], Cr [15-19], Mo [20-26], Ti [27-29] and V [3, 25, 30] under conditions thermodynamically allowing the formation of a compound layer, these elements have to be incorporated into the compound layer either as ternary nitrides (Fe-Me-N), or, especially in case of high affinity between Me and nitrogen, as precipitated nitrides Me-N. Thus, in case of alloying element precipitation as nitride prior to the formation of a compound layer, the development of γ' gets delayed. In case of less strong interaction between alloying element and nitrogen the formation of the compound layer can be difficult and even suppressed until all nitride forming elements have precipitated, or γ' has to grow under para-equilibrium conditions with Me dissolved.

Within the diffusion zone, Me precipitates with interstitially dissolved nitrogen as alloying element nitrides due to their affinity for nitrogen.

The compound layer considerably improves the tribological (resistance to wear and abrasion) and chemical properties (improvement of the corrosion resistance) due to its ceramic-like character. A typical area of application for nitrided parts having a compound layer is in applications of motor production (such as crankshafts). If the main demand of the nitriding process is to increase the fatigue life time of a component, usually bright (or "internal") nitriding is employed; the nitriding parameters are chosen such that only a diffusion zone develops (i.e. no compound layer can be thermodynamically formed at the surface). In this case, the development of compressive residual stresses due to the volume misfit of formed nitrides with the ferrite matrix is highly beneficial for the improvement of the fatigue properties. Such nitriding process is often applied for components such as springs of parts of the power transmission system in vehicles.

Depending on the strength of the affinity between nitride forming alloying element and nitrogen (i.e. thermodynamic driving force for the precipitation of Me-

nitrides) the nitride forming elements can be classified as follows, according to the resulting nitrogen concentration-depth profile (see schematically in Fig. 1.5):

- (i) *Strong nitride formers:* the nitrogen concentration-depth profile reveals a rectangular profile which is characterized by an increasing depth as function of nitriding time. The “height” of the concentration-depth profile remains unaffected of the nitriding time. In the surface-adjacent region, (nearly) all Me has precipitated as Me-N. The rate of precipitation is controlled by the diffusion of nitrogen in the ferrite matrix. As a result, a sharp boundary between the nitrified case and the unnitrified core exists, where nitrogen is virtually absent. The elements Ti and V belong to this group.
- (ii) *Weak nitride formers:* The nitrogen concentration-depth profile reveals ideally-weak nitriding kinetics, i.e. the rate of nitride development is independent of the distance from the surface (“bucket that fills up”). Thus, the nitrogen concentration is constant throughout the whole cross-section. As a result, no case-core boundary can be found. Therefore, an increase in nitriding time leads to an increase in nitrogen concentration *throughout* the cross-section, independent of the distance from the surface. The nitriding kinetics are controlled by the diffusion of the nitride forming alloying element. Alloying elements belonging to this category are Al and Si.
- (iii) *Nitride formers of intermediate strength:* the nitriding behaviour of such elements varies, depending on temperature and alloying element concentration, between the above mentioned extreme cases.

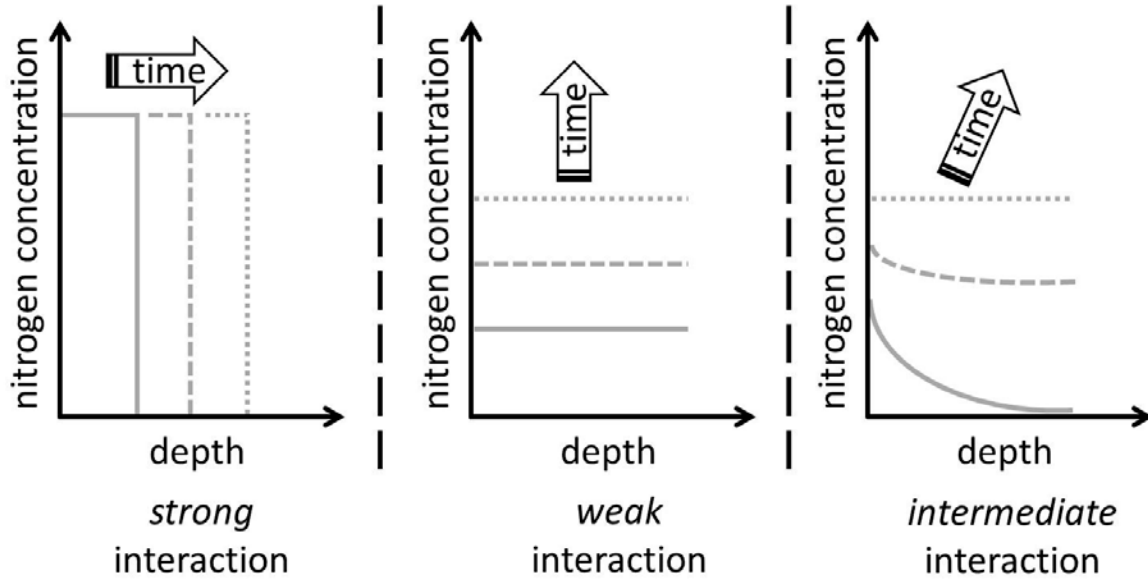


Fig. 1.5: Schematic illustration of the different kinds of interaction between nitrogen and nitride forming alloying element Me resulting in a different development of the nitrogen concentration-depth profile as function of nitriding time.

1.5 Excess nitrogen

It has often been reported that the total uptake of nitrogen in a Me-containing iron-based alloy, $[N]_{\text{tot}}$, can exceed the normal nitrogen uptake by far. *Normal* nitrogen uptake denotes the nitrogen that is strongly bonded to stoichiometric Me-nitrides, $[N]_{\text{Me-N}}$, and interstitially dissolved in the (unstrained) ferrite matrix, $[N]_{\alpha}^0$ in equilibrium with the nitriding gas atmosphere. The amount of nitrogen exceeding this normal nitrogen is called *excess nitrogen* [28, 29, 31].

Such excess nitrogen atoms can be found at different locations in nitrated Fe-Me alloys:

- (i) adsorbed at the (coherent) interface between coherent nitride precipitate and the surrounding ferrite matrix, $[N]_{\text{interface}}$
- (ii) trapped in the strain fields of dislocations, $[N]_{\text{dislocation}}$
- (iii) additionally dissolved in the strained matrix, $[N]_{\text{strain}}$, caused by the volumetric misfit between nitride precipitate and the surrounding matrix leading to a hydrostatic tensile stress component in the matrix thus increasing the solubility of nitrogen [31].

Excess nitrogen of type (i) and (ii) are denoted as *immobile* excess nitrogen as they do not take part in the (inward) diffusion of nitrogen, whereas nitrogen that tends to increase the diffusion zone is called *mobile* excess nitrogen. Type (iii) belongs to this mobile excess nitrogen.

The different kinds of (chemically) bonded nitrogen, taken up by a specimen upon nitriding, can be differentiated by generating an absorption isotherm. Any point in such a nitrogen concentration versus nitriding potential diagram indicates the equilibrium content of nitrogen absorbed by the specimen at a given nitriding potential. The generation of an absorption isotherm requires a homogeneous nitrogen concentration (i.e. constant concentration throughout the whole cross-section) and a nitride morphology that does not change upon determination of the absorption isotherm. Thus, in order to ensure a constant precipitation morphology, a pre-nitriding treatment is performed at a temperature exceeding the temperature for the generation of the absorption isotherm. Such nitrogen absorption-isotherm is schematically presented in Fig. 1.6. Three different types of absorbed nitrogen can be distinguished:

- (i) Type I nitrogen corresponds to nitrogen strongly chemically bonded to Me in the corresponding stoichiometric MeN nitride platelets. The amount of nitrogen required to cause full precipitation of all Me as MeN is denoted as “level A” in Fig. 1.6a. Type I nitrogen cannot be removed upon denitriding in pure H₂.

- (ii) Type II nitrogen is the nitrogen that is adsorbed at the interface between nitride platelet and the surrounding ferrite matrix ($[N]_{\text{interface}}$). This nitrogen can often be (partially) removed upon denitriding as it is less strongly bonded. The amount of interfacially adsorbed nitrogen corresponds to the difference between “level B” and “level A” in Fig. 1.6a.
- (iii) Type III nitrogen corresponds to nitrogen that is dissolved at octahedral sites of the ferrite matrix lattice, the amount of which depends linearly on the nitriding potential [8, 9]. The difference between the total amount of dissolved nitrogen and the solubility of nitrogen in a pure, unstrained ferrite matrix, $[N]_{\text{strain}}$, is indicated in Fig. 1.6a. Type III nitrogen can be easily removed by denitriding.

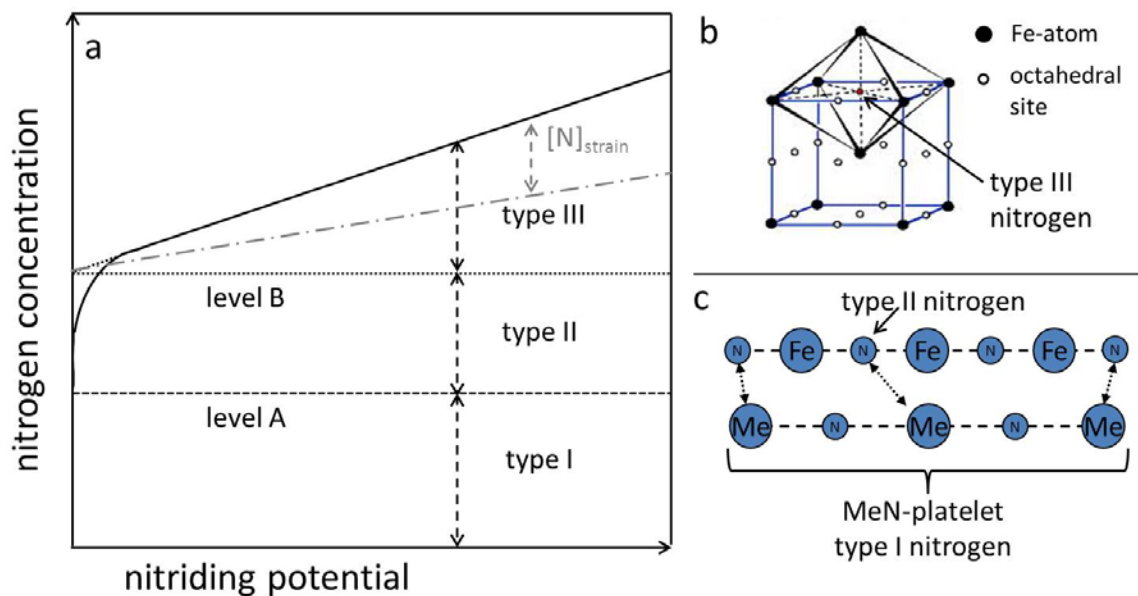


Fig. 1.6: (a) Schematic illustration of a nitrogen absorption isotherm, (b) type III nitrogen is interstitially dissolved in the matrix, (c) type II nitrogen is adsorbed at the precipitates/matrix interface (dissolved in the ferrite matrix) and type I nitrogen is (strongly) bonded in Me-N nitride platelets.

1.6 Residual stress

Residual stresses are self-equilibrating existing in materials at constant temperature and in the absence of external loading [32]. Residual stresses can have various kinds of origins, such as mechanical, thermal, plastic, or caused by phase transformations such as martensitic transformations or the precipitation of inner nitrides. However, residual stresses are always the result of misfit that can occur between different phases or different regions [33]. Depending on the length scale over which the lattice parameter varies, the distinction between *micro*- and *macro*stresses can be made [34]. Lattice parameter variations over large distances are denoted as macrostresses. The presence of both, micro- and macrostresses can strongly influence the fatigue behaviour of components [34]. Upon nitriding, nitrogen dissolves in the ferrite matrix and can form inner nitrides, both leading (theoretically) to an expansion of the nitrided zone due to the volumetric mismatch between precipitated nitrides and ferrite matrix (see Fig. 1.7b). As the nitrided zone and the unnitrided core are attached to each other, a compressive residual stress develops in the nitrided zone (as a result of a self-equilibrating stress state). The mechanical equilibrium between the nitrided zone and the unnitrided core requires the development of tensile stresses in the unnitrided core (Fig. 1.7c). Upon nitriding, a (thin) specimen can become through nitrided (homogeneously nitrided), and thus does not exhibit macrostresses (-depth profile), as indicated in Fig. 1.7d.

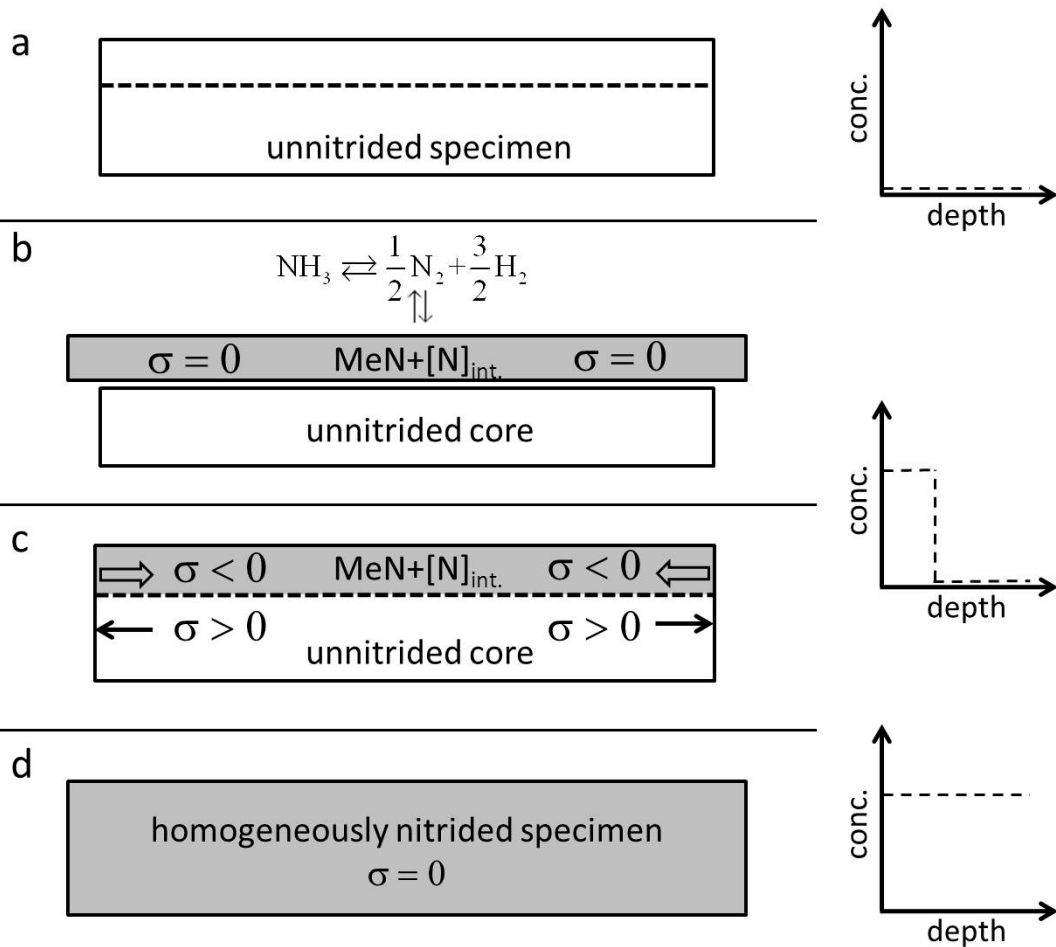


Fig. 1.7: Schematic illustration of the development of residual stresses upon nitriding (left side) and the corresponding nitrogen concentration-depth profiles. An unnitrided, macrostress-free specimen is considered in the initial stage (a), where nitrogen diffuses during nitriding. This leads theoretically to an expansion of the nitrided zone due to nitrogen dissolved in the octahedral interstices and due to the formation of inner nitrides MeN (b). As a result, a case-core nitrogen concentration-depth profile develops. The resulting equilibrium stress state (c) induces compressive macrostresses in the nitrided zone and tensile macrostresses in the unnitrided core. After through nitriding, the specimen is macrostress free, but strained (d).

1.7 Maraging steels

Maraging steels belong to the group of ultra-high strength martensitic steels which are age hardened by the precipitation of intermetallic compounds [35, 36] (*martensite+aging* → maraging). These steels have a low carbon content along with a high content of Ni and (usually) Co. In contrast to conventional high-strength steels, maraging steels possess certain distinctive characteristics such as lack of distortion during hardening, good weldability as well as good combinations of strength and toughness. These advantages have made them attractive for many technical applications [37, 38] since their development in the early 1960s by the International Nickel Company (INCO).

The transformation of austenite to martensite depends on austenite composition. If the carbon content is sufficiently low, this transformation forms a lath type martensite characterized by a high density of dislocations and the absence of transformation twins. This martensitic structure typically has a yield strength in the order of 700 MPa and, more importantly, has excellent ductility and toughness. Subsequently after the formation of martensite, these steels are precipitation hardened (aged) at a temperature of about 400 – 520 °C. In the beginning of age hardening, intermetallic compounds such as Ni_3X ($\text{X} = \text{Ti}, \text{Mo}, \text{V}, \text{W}$) are formed ([35, 36]). This precipitation leads to a strong increase in hardness due to the coherency between the precipitates and the surrounding matrix. Upon prolonged heat treatment, the more stable phase Fe_2Y ($\text{Y} = \text{Mo}, \text{W}$) forms, characterized by a decrease in hardness (overaging) [35, 36, 39, 40].

Maraging steels are subdivided into classes (so-called “grades”) depending on their nominal yield strength (in ksi), e.g. 200, 250, 300 or 350.

In general, it is also difficult to heat treat a single grade of maraging steel to widely different strength levels. Thus, several different grades of steels, each tailored to a specific strength level, are needed.

1.8 Outlook of the thesis

Gaseous nitriding provides a very powerful tool to improve the mechanical and chemical surface properties of iron-based workpieces and steels. Despite its wide application in practice, which is often mainly based on experience and empiricism, fundamental knowledge of the underlying processes occurring upon nitriding is lacking. To this end, there is a great scientific as well as technical interest in fundamental understanding of the processing methods in combination with the predictability of material properties.

Investigations of the precipitation morphology and kinetics have been started on simple binary [1-4] and ternary [5-7] iron-based alloys in the past. With these systems it is possible to gain a very fundamental approach as there is no other interaction than that of nitrogen with the nitride forming alloying element (Me) and the pure ferrite matrix.

However, there is still a great scientific interest in detailed understanding of binary iron-based alloys, especially for relatively weak nitride formers (such as Mo, W, Si), as these systems are not very well understood. The literature results, if at all available, often contradict each other, especially in case of molybdenum (e.g. [26] and [41]).

The nitriding behaviour of this (binary) system is dealt with in chapters 2, 3 and 4 of the present thesis with the aim to clarify these contradicting literature results and to provide a detailed understanding in the precipitation kinetics of Mo as nitride.

With the thus gained knowledge about the precipitation sequence of Mo-nitride, it is possible to understand the nitriding kinetics of technical steels containing Mo as (only) nitride forming element and, moreover, *model* the resulting nitrogen concentration-depth profiles. Such model was applied for a maraging steel for which, for the very first time in case of a technical steel, an absorption isotherm could be created (chapter 5).

For microstructural examinations, apart from weight gain measurements based on weighing the specimens before and after nitriding with a high accuracy microbalance (accuracy: 1 µg), light microscopy, scanning electron- and transmission electron

microscopy were employed as well as hardness measurements, electron probe micro analysis and glow discharge optical emission spectroscopy. Additionally, X-ray diffraction was used for the examination of the microstructure.

In chapter 2, the phenomenon of discontinuous precipitation, occurring upon nitriding of Fe-1at.% Mo alloy under conditions such that no compound layer develops at the surface, is described. Hereby, the role of the degree of deformation on the kinetics of nitride precipitation is investigated in detail. The submicroscopical, fcc Mo₂N-type nitrides, initially largely coherent with the matrix, obeying a Bain-type orientation relationship, transform in a discontinuous reaction into the incoherent, hcp MoN-type lamellar precipitates. In case of low dislocation density, a continuous, but slow increase in nitrogen concentration is observed. However, the corresponding microstructure finally shows a complete discontinuous transformation, whereas in case of a high dislocation density, only partial transformation of Mo₂N to MoN occurs. The mechanism underlying this effect is explained with the difference in driving force for the discontinuous precipitation reaction, depending on the degree of coherency of the initially formed nitrides.

The effect of the presence of substitutionally dissolved nitride forming alloying element with relatively weak (as compared to V, Ti) interaction with nitrogen on the morphology of the formed compound layer consisting of γ' -Fe₄N is discussed in chapter 3. An unusual morphology of the compound layer was observed upon nitriding of Fe-1at.% Mo alloy in the recrystallized (low defect density) state. This effect was ascribed to the delayed precipitation kinetics of Mo as nitride thus delaying the formation of γ' as the solubility of γ' for substitutional elements is very low. In case of nitriding cold deformed material, a microstructure develops similar to nitriding of pure iron. This can be ascribed to the much faster precipitation kinetics of Mo as nitride. A detailed kinetic analysis of the growth of the compound layer in case of cold deformed specimen is presented and discussed in this chapter.

A microstructural analysis of an Fe-3.07at.% Mo alloy is described in chapter 4. The role of the precipitation of Mo-nitrides, obeying a Bain-type orientation relationship

with the matrix, on the resulting microstructure upon low-temperature nitriding is discussed. Strongly asymmetric broadening of ferrite reflections along with pronounced streaking in the selected area diffraction patterns were indicative for largely coherent precipitates.

Finally, the nitriding behaviour of maraging steel (grade 300) is reported in chapter 5. The nitriding kinetics of specimens nitrided in the solution annealed condition were compared to the nitriding kinetics of specimens that were age hardened prior to nitriding. The nitrogen concentration-depth profiles were, in both cases, successfully fitted with a numerical model to the experimentally determined concentration-depth profiles. As fitting parameters, the diffusion coefficient of nitrogen in the matrix, the surface concentration, the stoichiometric parameter of the formed nitrides and the solubility product of the alloying element and nitrogen dissolved in the matrix were used. Nitrogen-absorption isotherms determined for the maraging steel allowed distinction of different kinds of (excess-) nitrogen taken up and thus provided starting values of the fitting parameters for the kinetic model.

CHAPTER 2

Molybdenum-nitride precipitation in recrystallized and cold rolled Fe-1at.% Mo alloy

H. Selg, E. Bischoff, R. Schacherl, T. Waldenmaier, E.J. Mittemeijer

Abstract

Nitriding of recrystallized and cold rolled Fe-1at.% Mo-alloy at 580 °C in a NH₃/H₂ gas mixture using a nitriding potential of 0.104 atm^{-1/2} leads to the formation of small, cubic-type nanometer-sized precipitate platelets of the type Mo₂N having a Bain-type orientation relationship with the ferrite matrix. After prolonged nitriding, micrometer-sized colonies of lamellae consisting of a hexagonal MoN-type nitride and ferrite develop in a discontinuous precipitation reaction; these nitride lamellae have a Burgers-type orientation relationship with the ferrite lamellae. As compared to the recrystallized specimens, in the cold rolled specimens the precipitation of the initial Mo₂N-type platelets occurs much faster and moreover, leads to (largely) incoherent(ly diffracting), instead of coherent(ly diffracting) precipitates, and is followed by an also much earlier but only partial occurring transition of Mo₂N-type to MoN-type precipitates. The results indicate that incorporation of iron in the nitrides can occur, if at all, only up till a negligible level, thereby invalidating earlier data.

2.1 Introduction

Nitriding is a thermochemical surface engineering treatment which is of great industrial importance in order to improve the mechanical (e.g. fatigue, wear) and chemical (e.g. corrosion) (surface) properties of ferritic steel components. Ammonia can be used as nitrogen donor, due to its dissociation at the surface of iron-based alloys at temperatures between 450 °C and 590 °C [42, 43]. Subsequent inward diffusion of the adsorbed nitrogen leads to the development of a nitrided zone beneath the surface. The nitrided surface layer, depending on the nitriding conditions ([10, 23]) can be subdivided into a compound layer adjacent to the surface, composed of iron nitrides, and a diffusion zone beneath the compound layer [44]. Within the diffusion zone, nitrogen is dissolved in the octahedral sites of the ferrite lattice, or has precipitated as internal nitrides MeN_x , if nitride forming elements, such as Ti, Cr, Al, V are present ([4, 7, 27, 29, 45]). The improvement of the fatigue resistance of nitrided workpieces can be ascribed to the precipitation of these nitride forming elements, whereas the enhancement of the chemical resistivity and the improvement of the tribological properties is mainly caused by the compound layer.

Usually, Mo is not added deliberately to nitriding steels, to induce nitride precipitation, but it is often introduced to improve the tempering brittleness, strength and weldability [46]. Although a distinct driving force for the precipitation of molybdenum nitride exists, relatively little of conclusive nature is known about the precipitation of Mo as nitride upon gaseous nitriding of a Mo-containing iron-based alloy.

It was claimed for an Fe-5wt.% Mo alloy nitrided at temperatures in the range of 480 °C – 590 °C that intermediate precipitates of structure type α'' - $Fe_{16}N_2$ would develop, superseded, upon overaging at elevated temperatures (in the range of 700 - 800 °C), by a (more or less) equilibrium precipitate identified differently as fcc Mo_2N [21, 23] or η - Fe_3Mo_3N [47]. The composition of the nitrides, for nitrided Fe-3at.% Mo alloy, was indicated as $Fe_3Mo_3N_2$ [20], but also as $Fe_{10}Mo_6N_2$ [21], $(Mo, Fe)_2N$ and $(Mo, Fe)N$

[26] (where the last two compositions would pertain to nitrides appearing later in the precipitation sequence). These composition data have all been based on field-ion-microscopy (FIM)-atom probe analyses. It is noted that this type of composition analysis, of platelets/discs of thickness only a few atomic layers, can be subject to severe errors. Indeed, in a very recent study [48], it was shown that surface-diffusion processes of interstitials, but also of substitutional dissolved elements, can affect the accuracy of *local* composition analysis by this technique. The only other work providing composition data of the nitrides concerned, *not* based on FIM-atom probe analysis, relies on a combination of Mössbauer spectroscopy and mass change and indicated that the nitrides do *not* incorporate Fe atoms and have the composition MoN [41].

The nature of the microstructure of the iron-based alloy can have dramatic consequences for the type of nitride that develops. This has been shown for Fe-Al alloy: in case of a recrystallized matrix hexagonal (wurtzite) AlN may precipitate preferentially, whereas in case of a deformed (cold rolled) matrix cubic (rock salt) AlN precipitates are formed [1, 49].

Recognizing the above sketched confusion and controversy regarding the precipitation sequence and the type of nitride precipitates developing upon nitriding Fe-Mo alloys, the present project has been designed to clarify the precipitation process in Fe-Mo alloy upon nitriding and to investigate the effect of the state of deformation of the microstructure on the precipitation process of nitrides.

2.2 Experimental

2.2.1 Specimen preparation

For the production of an alloy with the composition Fe-1at.% Mo appropriate amounts of iron (purity: 99.98 wt.%) and molybdenum (purity: 99.99 wt.%) were weighed, pre-alloyed in an arc furnace and melted in an Al₂O₃ crucible by means of an inductive furnace under a protective argon gas atmosphere (purity: 99.999 vol.%). The melt was cast in a copper mould to obtain a cylindrical rod (\varnothing : 10 mm, l : 100 mm). The chemical composition and the amount of impurities were determined by chemical analysis (inductively coupled plasma - optical emission spectroscopy (for Mo); combustion method (for C and S) and carrier gas hot extraction (for O and N)). The results are shown in Table 2.1.

Table 2.1: Amounts of molybdenum and light element impurities for the alloy used in this work (balance: Fe).

element	Mo	O	N	C	S
content [wt.%]	1.800±0.020	0.009±0.002	0.003±0.001	0.006±0.001	<0.001
content [at.%]	1.057±0.012	0.032±0.007	0.012±0.004	0.028±0.005	<0.002

The cast rod was cut into 3 pieces of which the shells were removed by grinding. The remaining pieces were cleaned with ethanol in an ultrasonic bath and then cold rolled to sheets of a thickness of about 0.12 mm (degree of deformation: 98.8 %). Out of these sheets, rectangular specimens were cut (dimensions: about 15 x 10 mm²) into which a hole was drilled (\varnothing : 1.5 mm) for suspending each specimen during nitriding (see below). The specimens were ground, cleaned in an ultrasonic bath using ethanol and then encapsulated in a quartz tube which was filled with argon gas (purity: 99.999 vol.%). Subsequently, a number of specimens were recrystallized in a muffle furnace at 800 °C for 90 min in order to eliminate the deformation introduced by the cold rolling.

2.2.2 Nitriding

For nitriding, a gas atmosphere composed of ammonia and hydrogen is often used. Gaseous nitriding allows an accurate control of the chemical potential of nitrogen in the nitriding atmosphere. The nitriding potential $r_N = \frac{P_{NH_3}}{P_{H_2}^{3/2}}$ is proportional with the chemical potential/activity of nitrogen in the atmosphere [8]. If so-called local equilibrium prevails at the surface, it holds that the chemical potential of nitrogen in the gas atmosphere is equal to the chemical potential of dissolved nitrogen at the surface. Thus, formation of a compound layer (composed of iron-based nitrides) can be avoided by control of the nitriding potential [9].

Before nitriding, the specimen surfaces were polished mechanically (final step: 1 μm diamond suspension), cleaned with ethanol in an ultrasonic bath and dried in a nitrogen gas flow.

The nitriding experiments were performed at a temperature of 580 ± 1 °C for nitriding times up to 734 h (the time required to achieve through nitriding of a pure ferrite specimen of thickness 120 μm (see above) is about 5h) in a vertical, multizone quartz-tube furnace (\varnothing : 28 mm) employing a NH_3/H_2 gas-mixture with a flux of 500 ml/min (purity NH_3 : > 99.998 vol.%, purity H_2 : 99.999 vol.%). The gas fluxes were adjusted by mass flow controllers and correspond to a nitriding potential $r_N = 0.104 \text{ atm}^{-1/2}$. The nitriding potential was chosen such that no iron nitrides develop at the surface (see above), i.e. the nitrated surface region consists only of the diffusion zone (possibly) exhibiting alloying element nitride precipitation. The nitriding process was terminated by breaking mechanically the quartz fibre at which the specimen was suspended in the furnace so that the specimen fell through an opened valve into a flask filled with water, flushed with N_2 , where the specimen was quenched to room temperature.

2.2.3 Specimen characterization

2.2.3.1 Light microscopy (LM), scanning electron microscopy (SEM) and electron backscatter diffraction (EBSD)

For these investigations a piece of each nitrided specimen was cut off (Struers Accutom 50, Al₂O₃ cut-off wheel), embedded in Struers PolyFast, ground and polished (final polishing step: 1 μm diamond suspension). Each cross-section was etched with 2 % Nital (2 vol.% HNO₃ in ethanol) at room temperature for about 10 s.

LM micrographs were taken using a Zeiss Axiophot microscope equipped with a digital camera (Olympus ColorView IIIu). SEM was performed employing a Jeol JSM 6300F using an acceleration voltage of 3 kV.

EBSD was performed on the same cross-sections of the specimens used for the LM and SEM investigations (final polishing step: 0.05 μm OPS-suspension) applying a Zeiss Leo 438 VP scanning electron microscope equipped with an EDAX TSL EBSD measurement system. For the analysis, the software OIM version 5 was used.

2.2.3.2 Electron probe microanalysis (EPMA)

For the determination of the nitrogen concentration-depth profiles EPMA was performed on the same cross-sections as for the LM, SEM and EBSD investigations. For these measurements, a Cameca SX100 microprobe (acceleration voltage $U = 10$ kV, current $I = 100$ nA, spot size about 1 μm) equipped with five wavelength-dispersive spectrometers was used. The line scans were performed perpendicular to the surface, starting at the surface across the cross-section towards the centre of the specimen. To obtain the element contents at each measurement point, the intensities of the characteristic X-ray emission peaks were measured and divided by the corresponding intensities obtained from standard samples of pure Fe, Mo and γ' -Fe₄N (for N-K_α). Elemental concentrations were calculated from the intensity ratios applying the $\Phi(\rho z)$ approach [50].

2.2.3.3 Microhardness measurement

Microhardness measurements were carried out on cross-sections of the nitrided specimens applying a Vickers microhardness tester (Leica VMHT Mot) applying a load of 490 mN and a dwell time of 10 s.

2.2.3.4 X-ray diffractometry (XRD)

Phase analysis by means of X-ray diffraction (from the surface of the specimens) was performed for all specimens before and after nitriding using a PANalytical X'Pert Multi-Purpose Diffractometer (MPD) with Co-K α radiation. This instrument is based on a Bragg-Brentano geometry and is equipped with a graphite monochromator in the diffracted beam. The diffraction-angle (2θ) range ($30^\circ < 2\theta < 120^\circ$) was scanned in steps of 0.06° 2θ with a counting time of 320 s per step. For the identification of the phases, based on the positions of the diffraction peaks, the ICDD database was used [51].

2.2.3.5 Transmission electron microscopy (TEM)

Electron transparent foils for TEM from the centre of the nitrided zone were prepared as follows: Self-supporting discs (\varnothing 3 mm) were stamped with a mechanical punch from sheets produced by removing material mechanically from both faces of the nitrided specimens (sheets; cf. section 2.2.1). The discs were ground mechanically, dimpled and subsequently, Ar-ion milled (4 kV, 5 mA, angle of ion incidence: 8° , time: 4.5 h; liquid nitrogen cooling stage).

TEM analysis was performed on a Philips CM 200 operated at 200 kV. Bright field (BF) images, dark field (DF) images and selected area diffraction patterns (SADPs) were recorded using a CCD camera incorporated in the TEM apparatus.

2.3 Results and discussion

2.3.1 Recrystallized specimens

2.3.1.1 Morphology; discontinuous transformation

Although nitrogen is taken up by the specimen, no change in morphology can be seen in the light optical micrographs in the early stages of nitriding (i.e. until a nitriding time of 50 h); yet a distinct increase in hardness is observed (see Fig. 2.1). The observed increase in hardness is much larger than the hardness increase that can be attained by dissolved nitrogen (i.e. about 100 HV, due to solid solution strengthening). Thus, (slow) submicroscopical Mo-nitride precipitation is assumed to occur (see below).

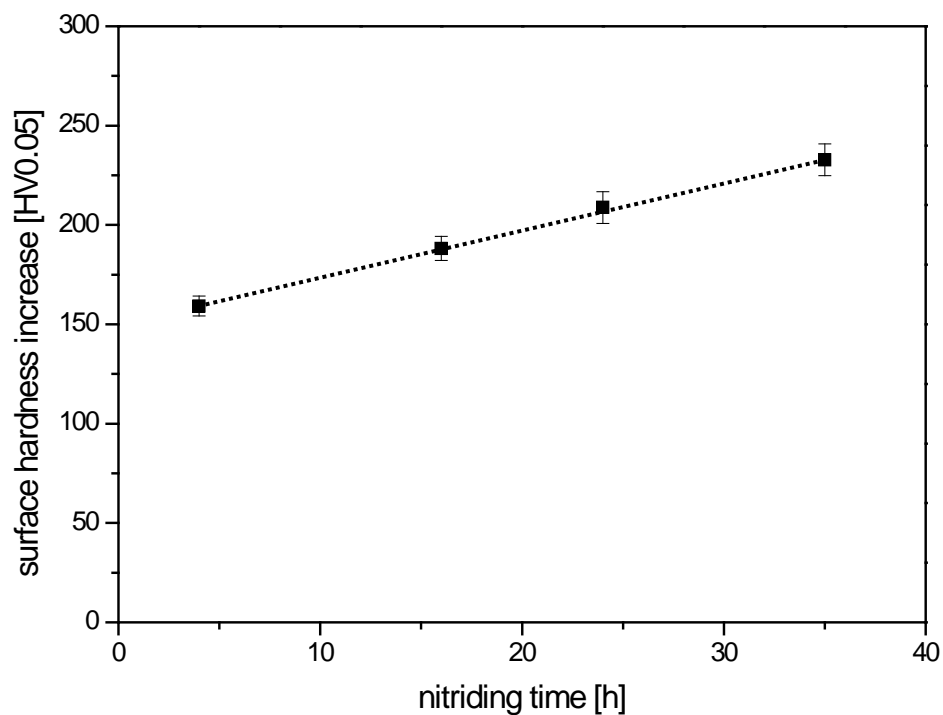


Fig. 2.1: Increase of surface microhardness, as compared to the initial, recrystallized state, as function of nitriding time at 580 °C for the early stage of nitriding. Dotted line has been drawn to guide the eye.

The morphological changes occurring upon nitriding for times > 50 h are revealed by light optical micrographs (LM) as well as scanning electron micrographs (SEM); see Figs. 2.2 and 2.4. In the homogeneously nitrated surface zone (see Fig. 2.3) regions exhibiting a lamellar-like microstructure, apparently evolving from grain boundaries, can be observed (Fig. 2.2). Such a microstructure is indicative of the occurrence of a discontinuous precipitation/coarsening reaction [52].

The EPMA line scan across a region showing discontinuous precipitation/coarsening (Fig. 2.3) indicates an overall nitrogen concentration in the lamellar region which is distinctly larger than that of the surrounding matrix. In the matrix, the nitrogen concentration is at the level of 0.45 at.%, thereby exceeding the maximum (at the nitriding temperature of 580 °C) solubility of nitrogen in pure ferrite (which is about 0.3 at.%; cf. Ref. [9]), suggesting that precipitation of submicroscopical nitrides has taken place already within these regions. Apparently, starting from the ferrite-matrix grain boundaries, these submicroscopical, fine nitrides are replaced by a (much coarser) lamellar microstructure composed of nitride and ferrite lamellae (for TEM evidence, see below); i.e. a discontinuous precipitation/coarsening reaction has occurred.

The nitrogen concentration in the lamellar regions is about twice that in the core regions of the ferrite-matrix grains where no discontinuous precipitation/coarsening was observed. This already suggests that the composition of the nitrides in the discontinuously precipitated/coarsened regions is different: the discontinuous precipitation/coarsening requires additional (i.e. continued) inward diffusion of nitrogen. This can explain the long time required to achieve complete transformation: only after 734 h of nitriding at 580 °C, virtually all grains had transformed by discontinuous precipitation/coarsening (see Fig. 2.4).

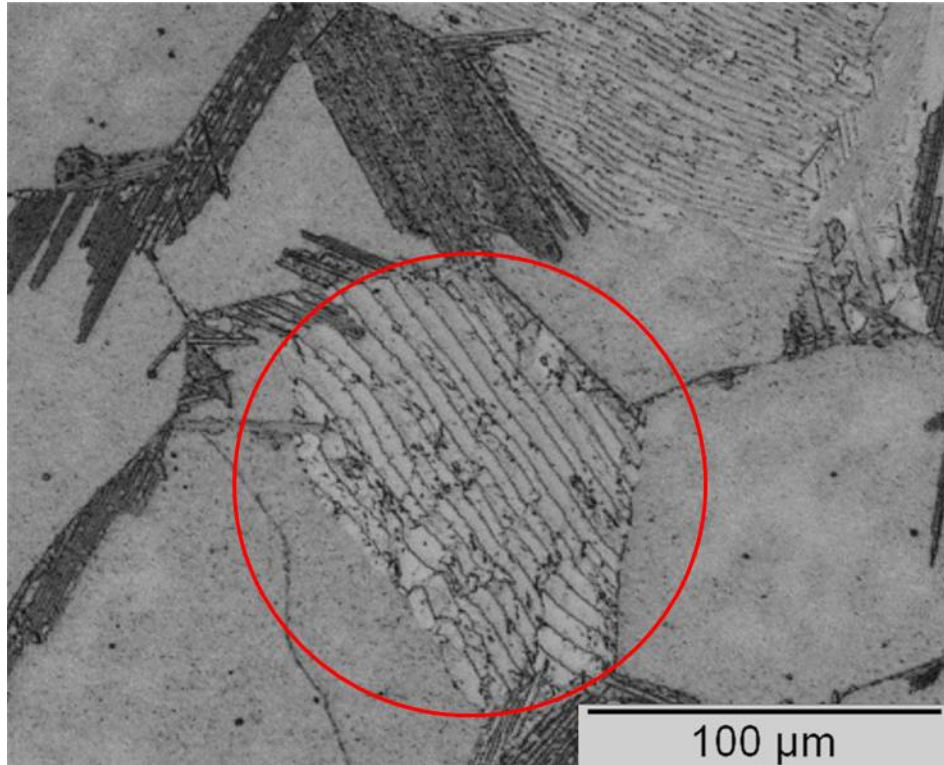


Fig. 2.2: LM-micrograph of a cross-section of a specimen nitrided for 150 h at 580 °C. The red circle indicates the area used for the EBSD analysis presented in Fig. 2.10.

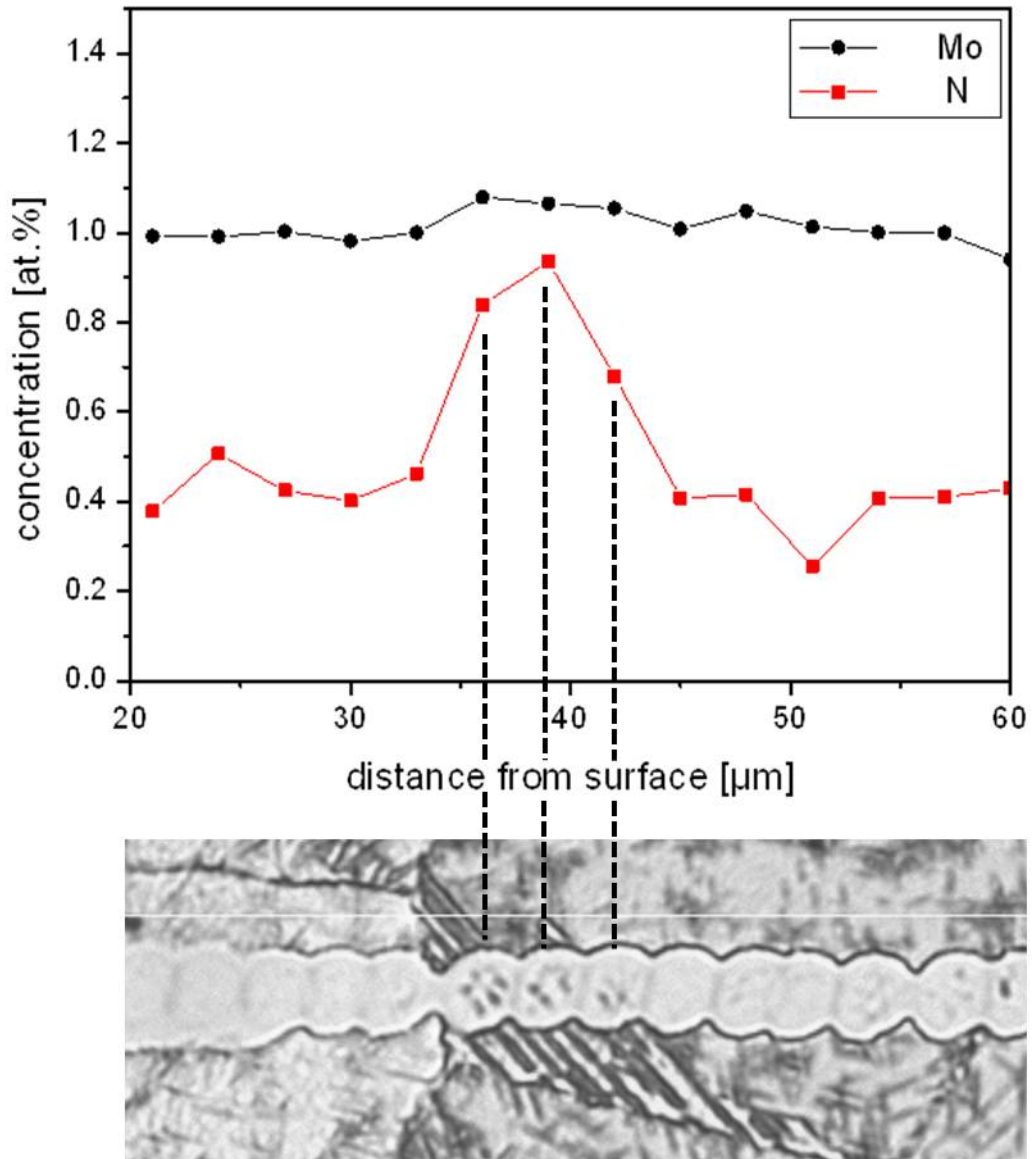


Fig. 2.3: EPMA concentration-depth profiles (N and Mo) of a specimen nitrided for 150 h at 580 °C, determined on a cross-section of the specimen. The corresponding light optical micrograph is given underneath showing the location of the EMPA line scan by the associated trace of carbon contamination.

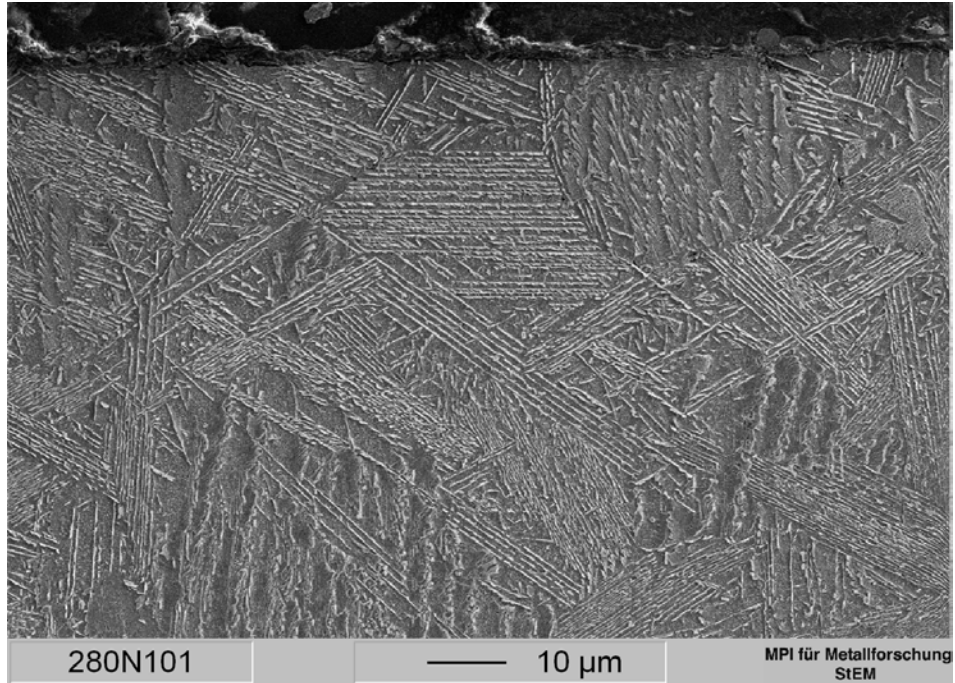


Fig. 2.4: SEM-micrograph of a cross-section of a specimen nitrided for 734 h at 580 °C showing a (completely) discontinuously transformed microstructure.

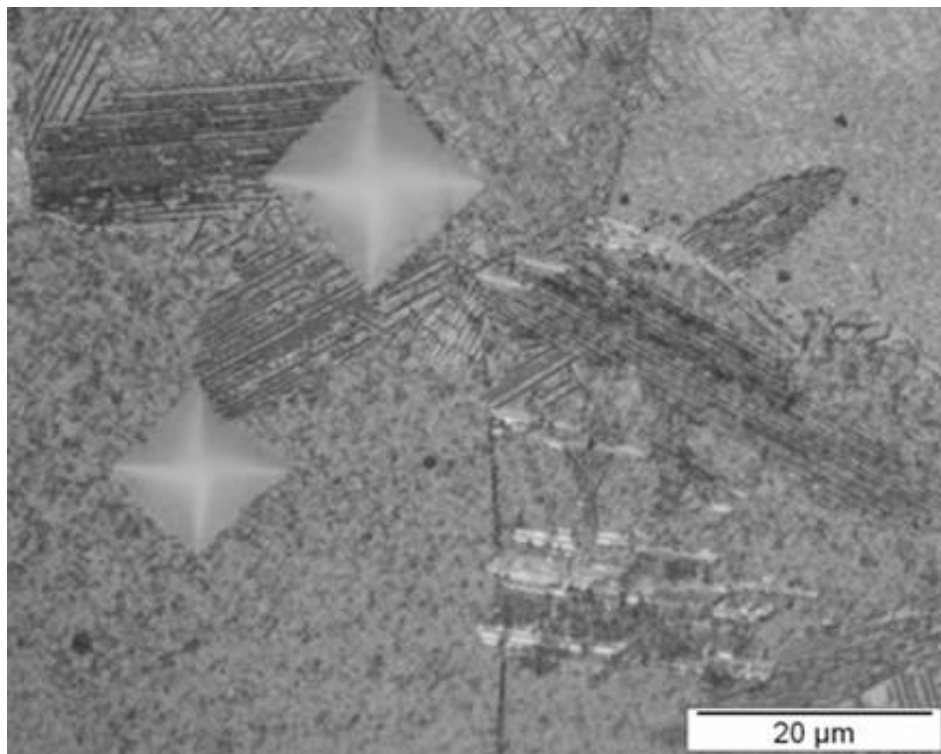


Fig. 2.5: LM-micrograph of a cross-section of a specimen nitrided for 282 h at 580 °C. The hardness indents

are much larger in a lamellar region than in a not transformed region; i.e. the hardness in the lamellar region is about 200 HV lower.

The discontinuous precipitation/coarsening leads to a distinct decrease of hardness (see Fig. 2.5): the hardness difference is more than 200 HV_{0.05}: 470 HV_{0.05} for the matrix as compared to 260 HV_{0.05} in the discontinuously precipitated/coarsened region.

2.3.1.2 Identification of precipitates

In the TEM bright field image recorded from a specimen nitrated for 70 h (no discontinuous precipitation/coarsening had occurred at that stage), at a depth of about 20 μm beneath the surface, disc-shaped precipitates can be discerned having a thickness of only a few nanometers whereas their (lateral) length can be several hundreds of nanometres and developing with their faces parallel to the $\{001\}_{\alpha\text{-Fe}}$ lattice planes (Fig. 2.6a). The selected area diffraction patterns (SADPs) reveal streaks (see e.g. Fig. 2.6c) along the $\langle 100 \rangle_{\alpha\text{-Fe}}$ directions. Apart from streaking, intensity maxima occur on the streaks in the selected area diffraction pattern which can be ascribed to reflections by nitrides of the type Mo_2N having a fcc crystal structure (defect-NaCl structure with N occupying half of the octahedral interstices); see dark field image (Fig. 2.6b) taken with the Mo_2N 200 spot. The SADP is compatible with a Bain-type orientation relationship for nitride (Mo_2N -type) precipitates and the matrix [1]: $(001)_{\alpha\text{-Fe}} // (001)_{\text{nitride}}$; $[100]_{\alpha\text{-Fe}} // [110]_{\text{nitride}}$.

The (theoretical) positions of diffraction spots of Mo_2N , oriented according to a Bain-type orientation relationship with the ferritic matrix, are shown in Fig. 2.6d. Indeed, apart from Mo_2N 200 reflections, indications for Mo_2N 111 spots can be seen in the experimental SADP as well (Fig. 2.6c), marked with white arrows.

The misfit between the precipitate and the matrix in directions parallel to the habit plane is relatively small, whereas the misfit perpendicular to the platelet is very large (cf. section 2.3.1.3 and see [45]). Thus, the development of streaks along the

$\langle 100_{\alpha\text{-Fe}} \rangle$ directions as a consequence of strain broadening in particular in the $\langle 100_{\alpha\text{-Fe}} \rangle$ matrix directions can be understood.

Similar observations (i.e. the presence of the fcc-type nitride Mo_2N , evidenced by reflections occurring from fcc Mo_2N -type precipitates together with strong streaking in the $\langle 100_{\alpha\text{-Fe}} \rangle$ directions), could still be made after a nitriding time of 282 h at 580 °C in regions where no discontinuous precipitation/coarsening had occurred (see Figs. 2.7a and b). TEM analysis after the same nitriding time (i.e. 282 h) but from a different region, where discontinuous precipitation/coarsening had occurred (Figs. 2.8a and b) and after longer nitriding times (e.g. see Figs. 2.9a and b), shows reflections originating from hexagonal MoN-type, lamellar precipitates. Thus, at such intermediate stages, both types of nitrides (i.e. Mo_2N as well as MoN) occur concurrently, but in different regions of the specimen. No streaks occur in the SADPs taken from such regions. The MoN/ $\alpha\text{-Fe}$ lamellae have a length of more than 20 μm and a distance of about 1 μm between the lamellae. The lamellae are oriented such that $\{001\}_{\text{MoN}} // \{110\}_{\alpha\text{-Fe}}$; i.e. close packed planes are parallel.

EBSD confirms this TEM analysis: the EBSD image (Fig. 2.10) taken from the region showing discontinuous precipitation/coarsening in the LM-image (marked with a red circle in Fig. 2.2), indicates the presence of a hexagonal (MoN-type) phase. The orientation relationship of the hexagonal MoN-type phase with respect to the ferrite matrix complies with the Burgers orientation relationship [53]:

$$(0001)_{\text{MoN}} \parallel (110)_{\alpha\text{-Fe}}, \langle 2110 \rangle_{\text{MoN}} \parallel \langle 111 \rangle_{\alpha\text{-Fe}}$$

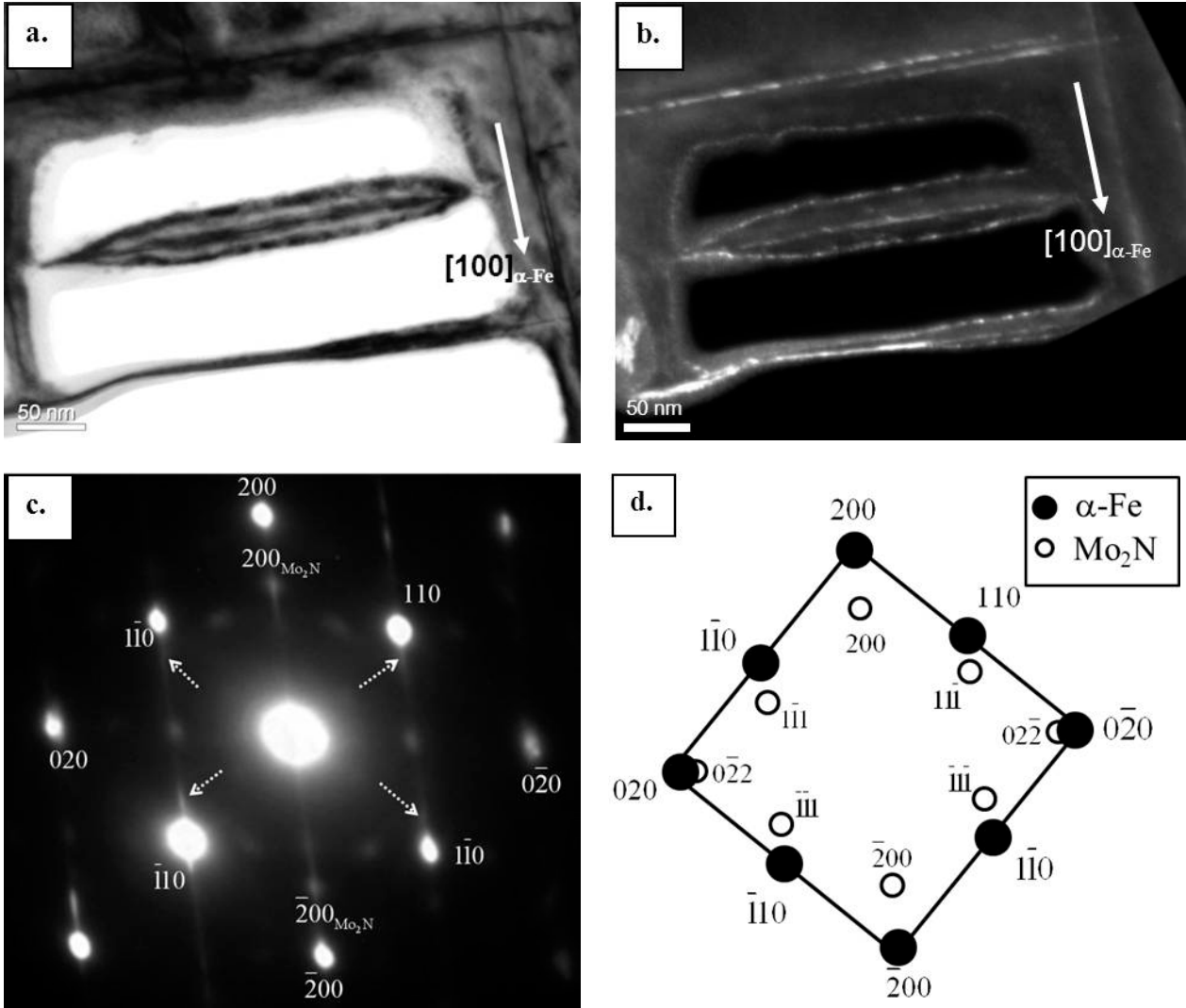


Fig. 2.6: TEM bright field image (a) of a specimen nitrided for 70 h at 580 °C, taken from a region before discontinuous precipitation/coarsening had started. The dark field image (b) was made with the Mo_2N 200 spot. The corresponding SADP is shown in (c) (zone axis/electron beam direction: $001_{\alpha\text{-Fe}}$). Extra reflections originating from fcc Mo_2N -type have been indicated. The white arrows indicate the location of the $111_{\text{Mo}_2\text{N}}$ spots. The theoretical diffraction pattern is schematically given in (d) denoting the positions of the reflections of the nitride precipitates and the ferrite matrix according to a Bain-type orientation relationship. The non-indicated spots in this and the other SADPs shown in this chapter are caused by an iron-oxide layer that developed on the surface of the foil during TEM specimen preparation; see discussion in sec. 2.5 of Ref. [1].

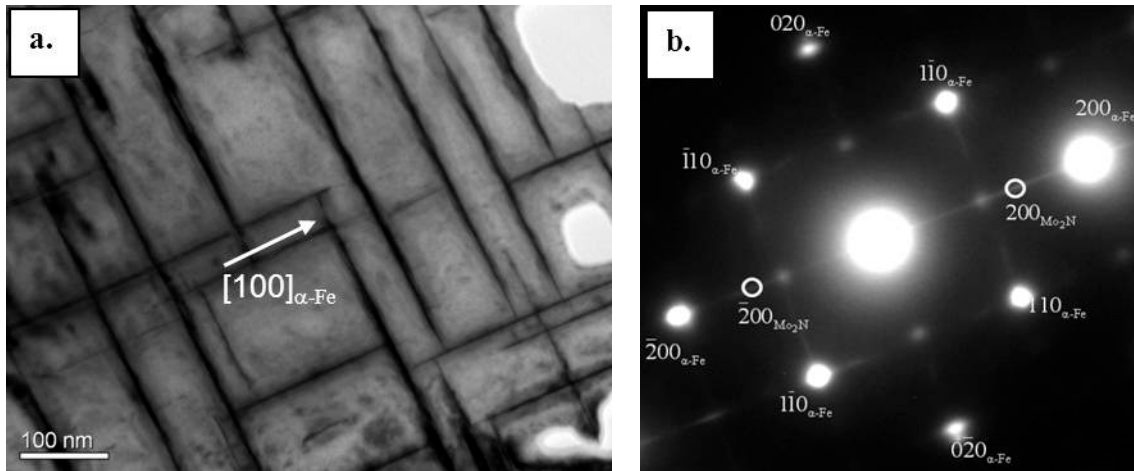


Fig. 2.7: TEM bright field image (a) and corresponding SADP (b), taken from a not discontinuously precipitated/coarsened region (zone axis/electron beam direction: $001_{\alpha\text{-Fe}}$) after a nitriding time of 282 h at 580 °C.

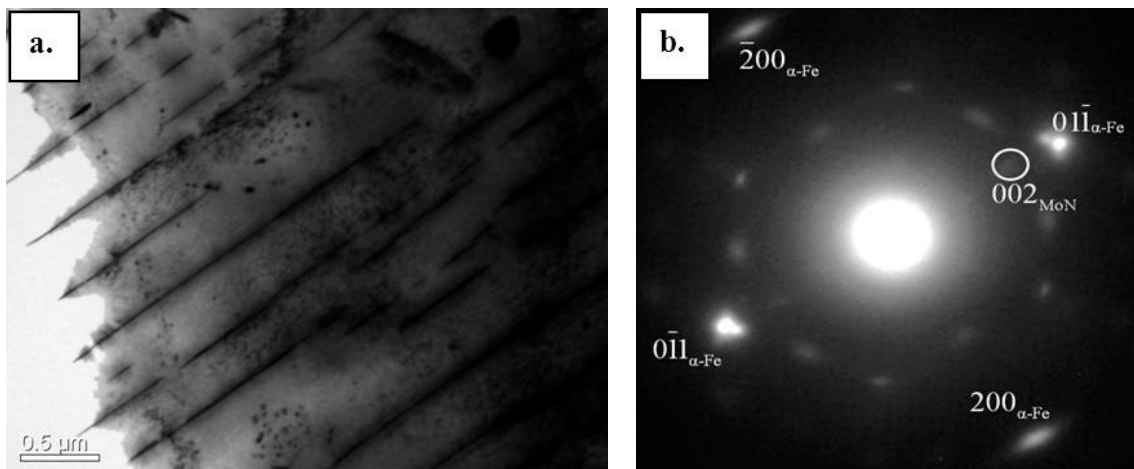


Fig. 2.8: TEM bright field image (a) and corresponding SADP (b), taken from a discontinuously precipitated/coarsened region (zone axis/electron beam direction: $011_{\alpha\text{-Fe}}$) after a nitriding time of 282 h at 580 °C.

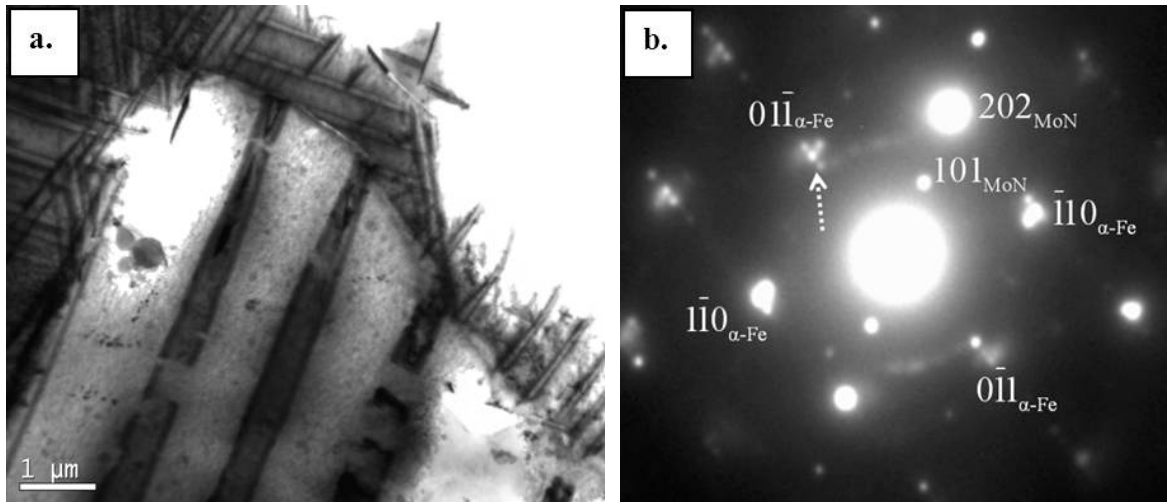


Fig. 2.9: TEM bright field image (a) and corresponding SADP (b), taken from a lamellae within the discontinuously precipitated/coarsened region (zone axis/electron beam direction: $111_{\alpha\text{-Fe}}$) after a nitriding time of 420 h at 580 °C. The white arrow marks the position of a MoN 200 reflection.

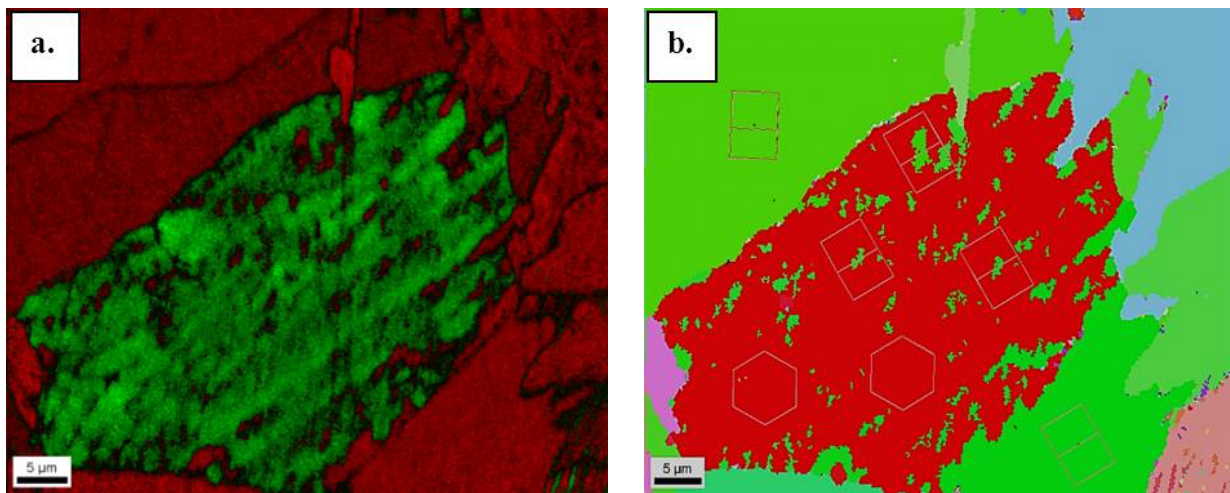


Fig. 2.10: EBSD image of the region marked with a red circle in Fig. 2.2. The phase map (a) indicates the presence of a hexagonal (MoN-type) phase by a green colour, while a cubic (α-Fe-type) phase is presented with a red colour. The orientation map (b) led to determination of a Burgers orientation relationship of the hexagonal (MoN-type) phase (red colour) and the bcc ferritic matrix (green colour).

2.3.1.3 Anisotropic matrix distortion

In the early stages of nitriding, i.e. before discontinuous precipitation/coarsening can be detected in the microstructure, in the X-ray diffraction patterns (recorded from the surface of the specimen) only reflections belonging to ferrite can be observed (see Fig. 2.12; diffraction pattern after 88 h of nitriding). The absence of reflections of the cubic, fcc-type nitride Mo_2N (see the TEM results; section 2.3.1.2) could be due to the small size of these precipitates (see Figs. 2.6 and 2.7), and also be a consequence of the coherent nature of these nitride precipitates: coherent diffraction of the nitrides with the ferritic matrix can occur [45, 54]. Then, because of the correspondingly, anisotropically, tetragonally distorted ferrite matrix [45], due to the mismatch of ferrite matrix and nitride platelets (see Fig. 2.13), strongly broadened tetragonal 200/002 doublets in the diffractograms can occur, as observed (see Fig. 2.11): the strongly asymmetric broadened, originally 200 reflections of the bcc α -Fe matrix cannot be fitted with a single peak. The best result is obtained with a fitting procedure adopting one peak for the cubic ferrite and one (of doublet nature) for nitride particle and the tetragonally distorted surrounding matrix (see Fig. 2.11). As starting values for the fitting procedure applied to this composite peak, data given in [55] were used for the cubic, ferrite reflection as well as for the tetragonal doublet reflection (nitride + surrounding matrix). The intensity “hump” at the high angle side of the measured, composite reflection (at a 2θ value of about 77.4° ; see arrow) is caused by the $\text{Co-K}\alpha_2$ component in the incident radiation.

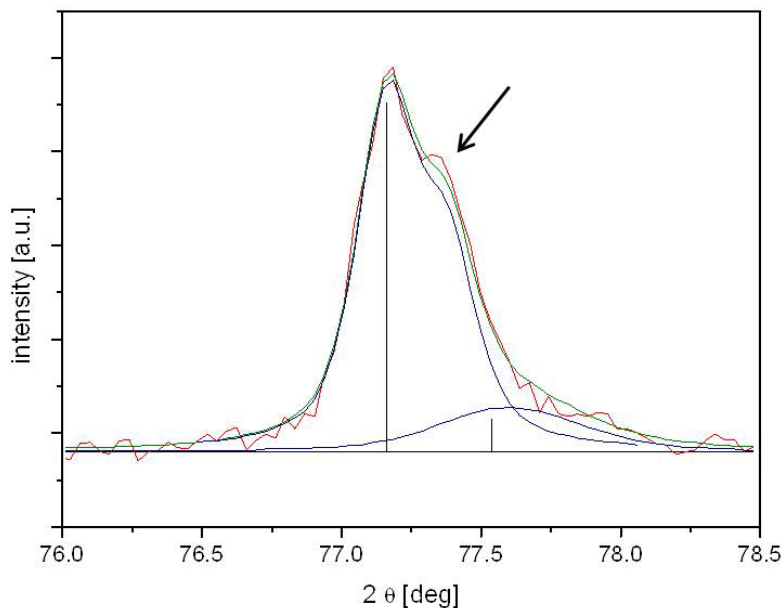


Fig. 2.11: Measured (red line) diffraction profile of a specimen (homogeneously) nitrified for 156 h at 580 °C. A fitting procedure was applied adopting one peak for the cubic ferrite and one (of doublet nature) for nitride particle and the tetragonally distorted surrounding matrix (blue line). The corresponding overlapped, calculated diffraction profile (green line) corresponds well with the measured one. The arrow indicates the contribution of the Co- $K\alpha_2$ component in the incident radiation.

Upon nitriding until about 150 h the intensity ratio of the tetragonal to cubic “ferrite” reflections increases suggesting that the fraction of (partially) coherent Mo_2N precipitates (leading to this tetragonal distorted “ferrite” reflection) increases until a nitriding time of about 150 h. The transition of Mo_2N (fcc, submicroscopical) to MoN (hexagonal, lamellar), taking place in a discontinuous manner (cf. section 2.3.1.1), becomes dominant after 150 h of nitriding and is associated with an abrupt drop of this intensity ratio.

Upon continued nitriding additional reflections emerge in the X-ray diffraction patterns which can be identified as reflections of the hexagonal MoN-type nitride (e.g. see results for 268 h and 734 h in Fig. 2.12). This stage is therefore characterized by the presence of mainly MoN precipitates, which well agrees with the result of the TEM analysis from discontinuous precipitated/coarsened regions (cf. Figs. 2.8 and 2.9) and is

compatible with the recognition that at this stage the largest part of the specimen had experienced the discontinuous precipitation/coarsening reaction.

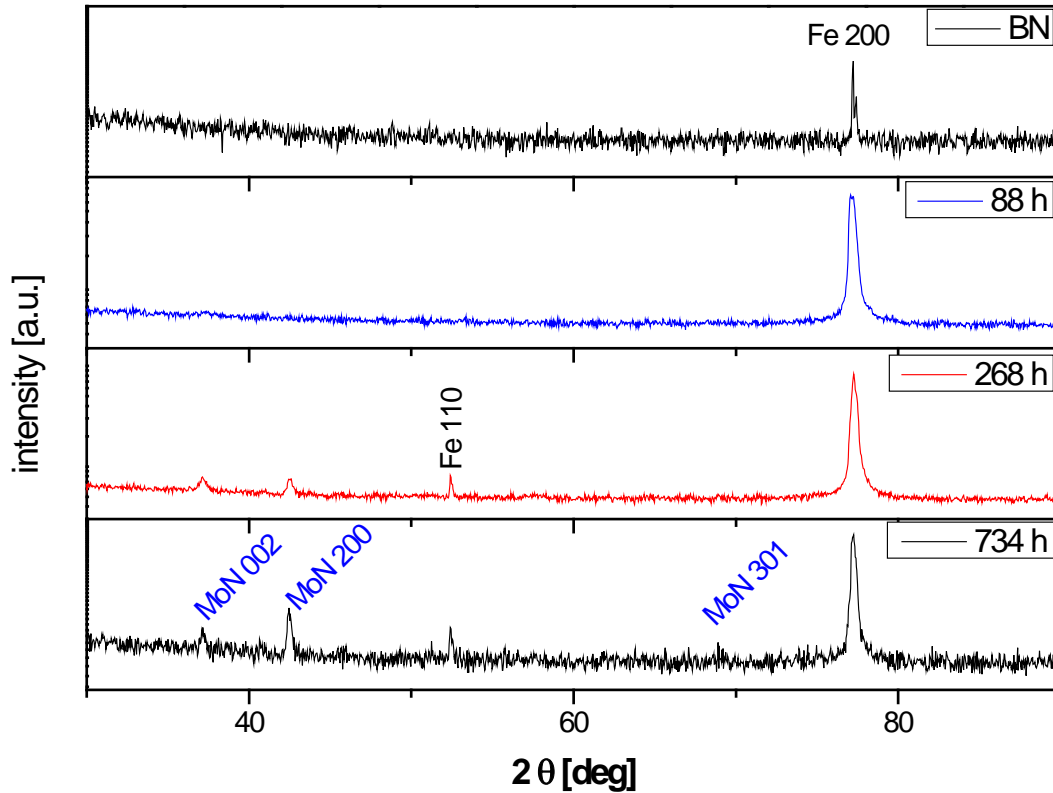


Fig. 2.12: X-ray diffraction pattern of the recrystallized specimen before nitriding (BN), and after nitriding at 580 °C for 88 h, 268 h and 734 h showing reflections belonging to ferrite and the hexagonal MoN-type nitride (the 200 and 002 reflections of MoN have a relative intensity of 100 % and 49 %, respectively, according to Ref. [51]).

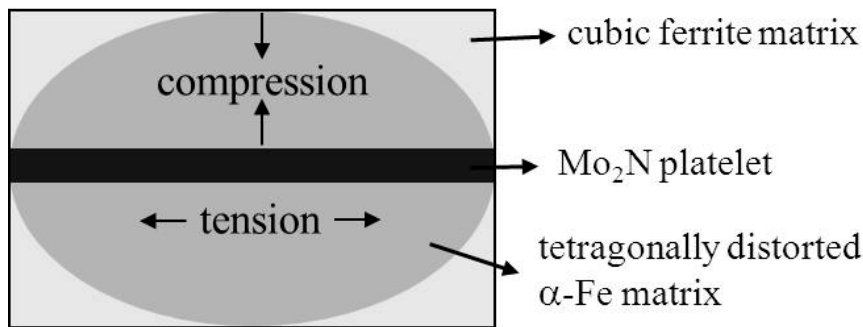


Fig. 2.13: Schematic view of a Mo_2N platelet coherent with the matrix leading to an expansion of the ferrite lattice-plane spacing in directions parallel to the platelet and a corresponding compression of the lattice-plane spacing in directions perpendicular to the platelet: the ferrite matrix surrounding the platelet is distorted tetragonally.

The lattice parameter of the unnitrided, annealed specimen, as calculated from the ferrite-matrix peak positions, is slightly larger than the stress-free equilibrium lattice parameter of pure iron [51] (see Fig. 2.14), as a consequence of Mo initially being dissolved in the ferritic matrix [56]. The increase of the lattice parameter in the early stages of nitriding, as indicated by a shift of the ferrite-matrix peak position to lower 2θ values, can be ascribed to nitrogen becoming dissolved in the ferrite lattice and to the elastically accommodated misfit of the Mo-nitride with the ferrite matrix leading to an overall hydrostatic tensile stress component [31]. The coherent to incoherent transition of the nitride precipitates, associated with the occurrence of the discontinuous precipitation/coarsening, then leads to an abrupt decrease of the ferrite-lattice parameter and thus a shift of the ferrite-matrix peak position to higher 2θ values. The finally reached value of the lattice parameter corresponds to that of pure ferritic iron, implying that all Mo present in the specimen has precipitated as (incoherent) nitride.

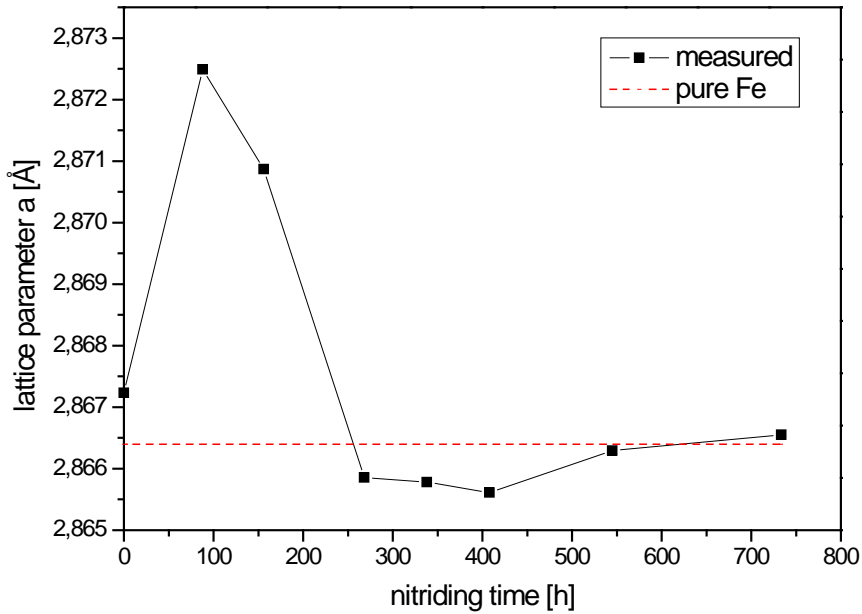
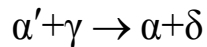


Fig. 2.14: Lattice parameter of ferrite depending on nitriding time at 580 °C. The black points represent the lattice-parameter values derived from the measured peak positions of the 200 reflection. The dotted line represents the lattice parameter of pure, unstrained ferrite [51].

2.3.1.4 The discontinuous transformation

The results presented in the preceding subsections can be summarized as follows. The nitride precipitation starts with the formation of submicroscopical Mo₂N-type precipitates (no indication of α' -(Fe, Mo)₁₆N₂-type precursors (cf. section 2.3.1.2) was obtained) followed by a discontinuous transformation of the type [57, 58]:



where α' denotes the supersaturated, distorted ferrite-matrix (cf. section 2.3.1.2), γ represents the submicroscopical likely largely coherent Mo₂N-type precipitates and α and δ represent the ferrite and MoN-type lamellae in the colonies produced by the discontinuous transformation starting from (mobile) grain boundaries in the ferrite matrix. Because the crystal structures of γ and δ are not identical, the discontinuous transformation in this case is a pure discontinuous *precipitation* reaction and cannot be considered as a discontinuous *coarsening* reaction (of the type $\alpha' + \beta' \rightarrow \alpha + \beta$ as observed and discussed for nitrated Fe-Cr and Fe-V alloys [2, 3]).

2.3.1.5 Nitrogen uptake

The nitrogen uptake of the specimen was determined by weight gain measurements at 580 °C as function of nitriding time. After about 5 h of nitriding the specimen (thickness approximately 120 μm) is through nitrated and exhibits an overall compositional homogeneity (cf. section 2.2.2). Thereafter the mass change by nitrogen uptake represents the overall homogeneous change of the nitrogen content. The mass uptake curve (Fig. 2.15) can thus be interpreted recognizing three stages of nitriding:

- (i) Nitrogen taken up rapidly by the specimen in an initial stage of nitriding till about 20 h. This nitrogen is mainly dissolved in the octahedral interstices of the ferritic lattice: saturation of the matrix is achieved after less than 20 h.
- (ii) The continuous, slow increase in nitrogen content between 20 h and about 200 h of nitriding can be ascribed to the slow precipitation of Mo as the

extremely small, initially coherent nitrides of Mo_2N -type (see Figs. 2.6 and 2.7).

- (iii) Discontinuous transformation starts after a nitriding time of about 200 h, leading to an acceleration of the nitrogen-uptake rate which is ascribed to the obviously larger capacity per Mo atom for nitrogen incorporation in MoN-type precipitates, as lamellae in the discontinuously transformed regions, than in the (submicroscopical) Mo_2N -type precipitates. Due to the change in stoichiometry (Mo_2N -type \rightarrow MoN-type), nitrogen has to diffuse from the gas phase to the growing lamellae. The theoretically expected nitrogen content in the specimen, if all Mo has precipitated as MoN, plus the amount of nitrogen that can be dissolved in the unstrained ferritic matrix ([9]), has been marked with a red dotted line in Fig. 2.15. Indeed, the measured nitrogen content asymptotically reaches this value upon prolonged nitriding. This result (a) contradicts earlier FIM-atom probe data [26] that a substantial amount of Fe would be incorporated in the MoN-type precipitates (at positions of the Mo atoms in the crystal structure) (see also section 2.1) and (b) agrees with results obtained in [41].

It is remarked that such controversy about the whether or not incorporation of Fe in nitride precipitates also exists regarding the precipitation of CrN during nitriding of Fe-Cr alloys. FIM-atom probe data suggest such Fe incorporation [59], whereas mass-change data for homogeneously nitrated specimens clearly indicate that all Cr has precipitated as CrN [17]. It may be that the occurrence of surface diffusion of atoms on the FIM-atom probe specimens invalidates the local composition analysis by the FIM-atom probe [48]. It strikes that composition analyses based on other techniques, albeit not based on local composition determination, indicate that the alloying element nitrides do not incorporate iron atoms from the matrix [17, 30, 41]. Yet, at the present state of knowledge, it cannot be excluded that some iron is taken up in the nitrides especially at very early stages of precipitation.

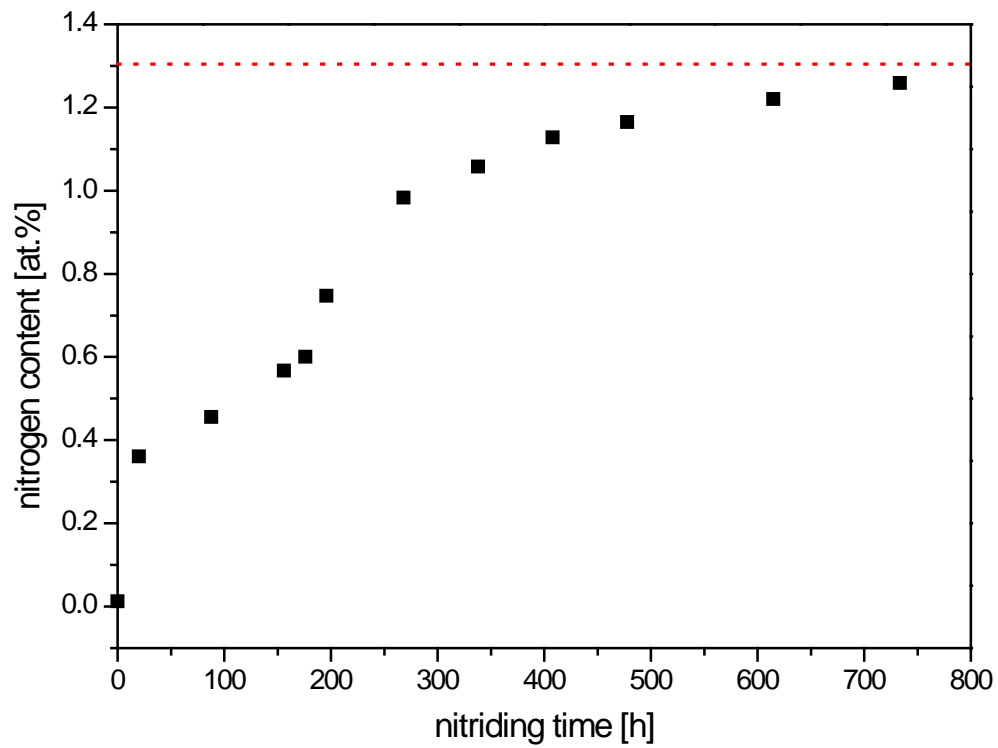


Fig. 2.15: Nitrogen uptake as function of nitriding time at 580 °C for the recrystallized specimen. The red dotted line represents the calculated nitrogen content under the assumption that all molybdenum in the specimen precipitates as MoN plus the amount of nitrogen that can be dissolved in the unstrained, ferritic matrix.

2.3.2 Cold rolled specimens

2.3.2.1 Morphology; discontinuous precipitation reaction

The microstructure of the cold rolled specimen after nitriding is shown in the light optical micrograph taken after a nitriding time of 90 h (Fig. 2.16). Regions exhibiting a lamellar-like microstructure due to discontinuous precipitation, as observed for the recrystallized specimen, can be discerned (cf. Fig. 2.2). The nitrogen concentration-depth profile, determined by EPMA after nitriding for 90 h and subsequent denitriding for 70 h at 470 °C (see discussion immediately below), indicates an enhanced nitrogen concentration within the lamellar-like region, as compared to the surrounding matrix (also as observed for the recrystallized specimen; cf. Fig. 2.3).

The denitriding treatment was carried out under pure hydrogen in order to remove the interstitially dissolved nitrogen in the ferritic matrix (and possibly (excess) nitrogen adsorbed to the faces of the nitride platelets (cf. [30, 31])). Then, the measured nitrogen concentration in regions where no discontinuous precipitation had taken place equals about 0.5 at.%. This amount of nitrogen well corresponds to full precipitation of Mo as nitrides of stoichiometry Mo_2N . This suggests that also the (nitrided) Mo_2N -type precipitates incorporate no significant amount of Fe atoms (see discussion in section 2.3.1.5). In the lamellar-like, discontinuously transformed regions, the nitrogen concentration is distinctly higher than in the surroundings which is due to the change in nitride stoichiometry from Mo_2N to MoN .

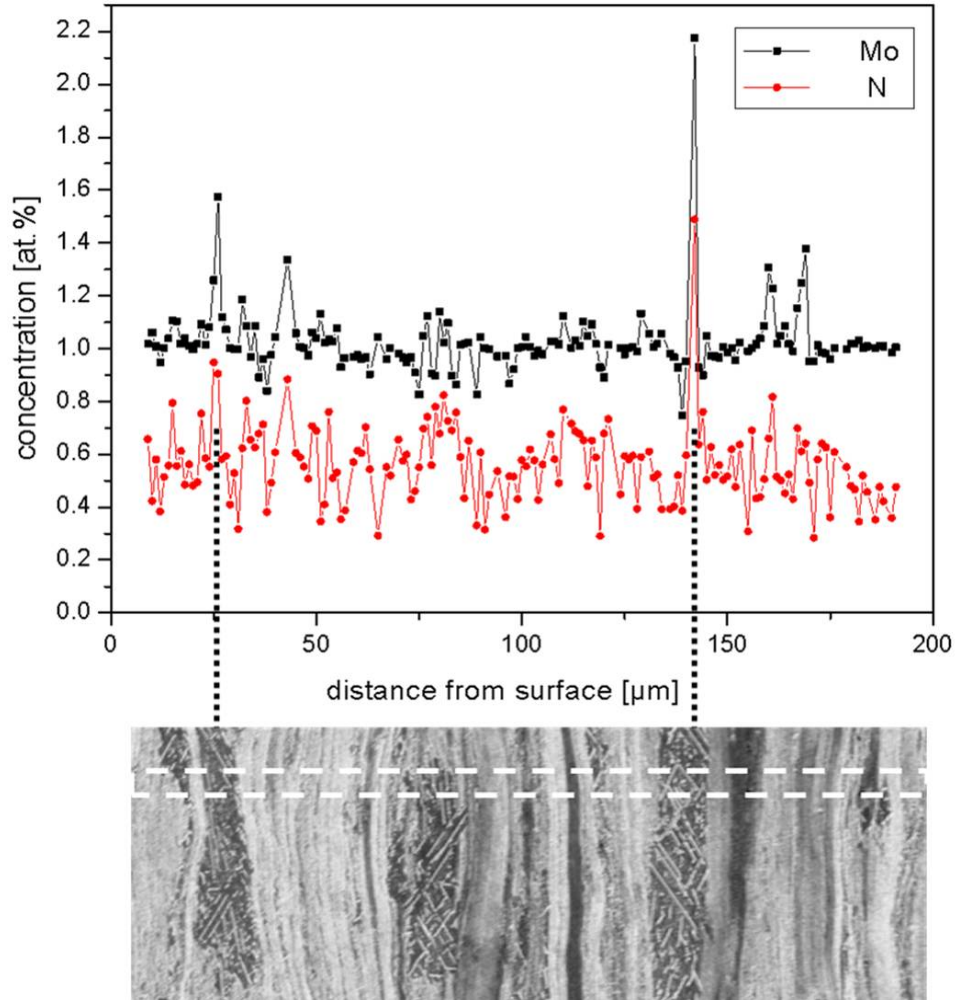


Fig. 2.16: EPMA concentration-depth profiles of nitrogen and molybdenum of a specimen nitrified for 90 h at 580 °C and subsequently denitrified for 70 h at 470 °C, as determined on a cross-section of the specimen. The corresponding light optical micrograph is given underneath showing the location of the EPMA line scan (marked with white dashed lines). An enhanced nitrogen concentration is observed at locations in the microstructure where a lamellar morphology prevails.

2.3.2.2 Identification of precipitates

TEM analysis of a region not subjected to discontinuous transformation (note the relatively short nitriding time of the specimen pertaining to Fig. 2.17) leads to similar results, as for the recrystallized specimen: a high density of platelet-type precipitates is observed. These platelets have a length of several hundreds of nanometers and a thickness of only a few nanometers. These precipitates are oriented along the $(100)_\alpha$

planes of the ferritic matrix (the platelets shown in Figs. 2.17a and b are parallel to a (001) plane of the α -Fe matrix which is inclined with respect to the surface of the foil). Apart from modest streaks along the $\langle 100 \rangle_{\alpha}$ directions a weak-intensity maximum (on these streaks) can be identified as a Mo_2N -type 200 reflection. As compared to the recrystallized specimens, streaking is less pronounced for the cold-deformed material, suggesting a more incoherent nature of the Mo_2N -type precipitates (cf. Figs. 2.7b and 2.17b); see further below.

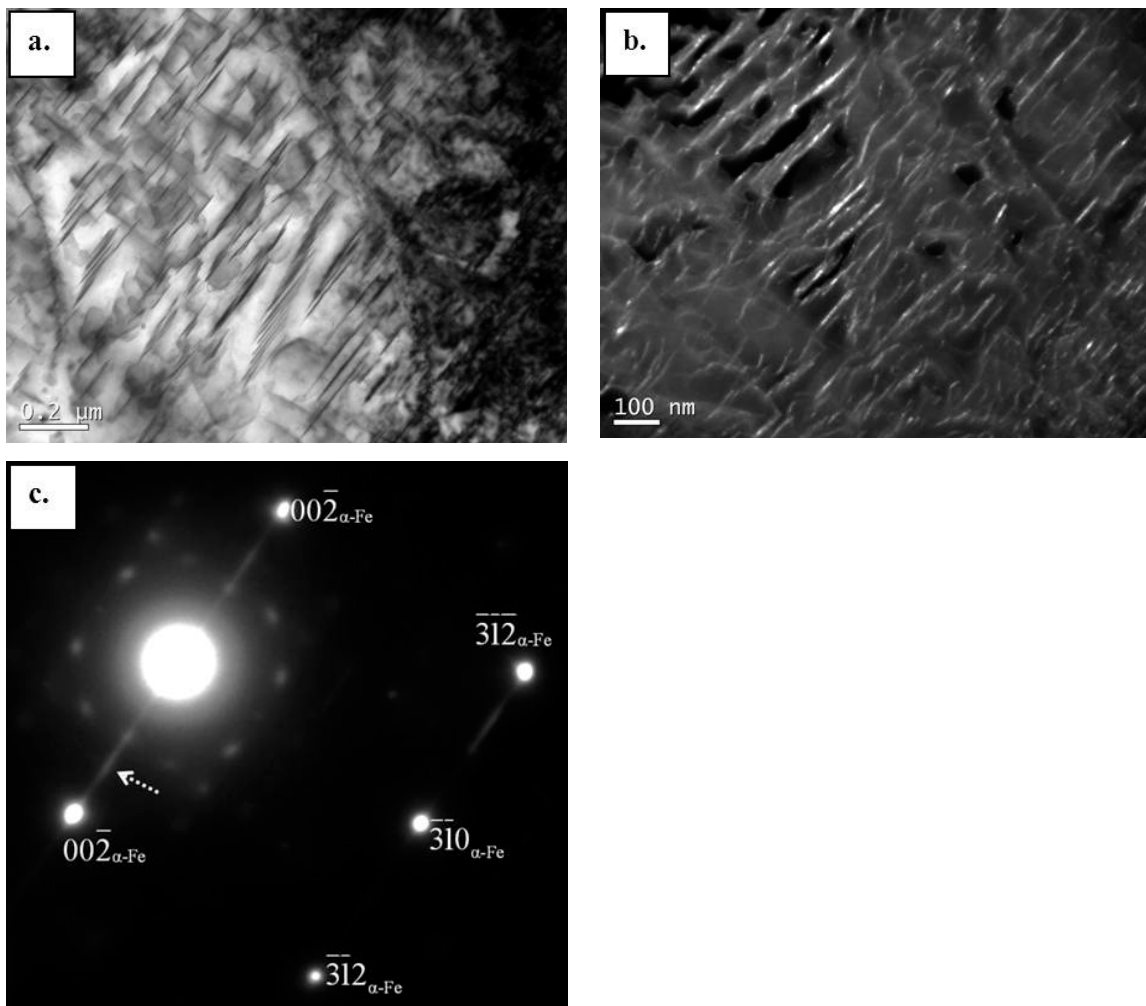


Fig. 2.17: TEM bright field image (a) of a specimen nitrided for 55 h at 580 °C, taken from a region before discontinuous precipitation/coarsening had started. The dark field image (b) was made with a Mo_2N 200 spot marked with a white arrow in the corresponding SADP (c) (zone axis/electron beam direction: $[\bar{1}\bar{3}0]_{\alpha\text{-Fe}}$).

In contrast with the recrystallized specimens, the X-ray diffraction patterns taken from the surface of the cold rolled specimens (Fig. 2.18) do reveal reflections from Mo_2N -type precipitates, already after a comparatively short nitriding time of about 1.5 h. This indicates that the Mo_2N -type precipitates formed upon nitriding of cold rolled specimens diffract incoherently with the matrix: An incoherent nature of the Mo_2N -type in the cold rolled specimens can be a consequence of the high defect density of the cold rolled specimen: heterogeneous nucleation of the Mo_2N -type precipitates can occur onto these defects such as dislocations (this is consistent with the above discussion of TEM results).

Upon continued nitriding (beyond 1.5 h), the diffracted intensities of the Mo_2N -type nitrides increase until, after 10 h, additional reflections belonging to the hexagonal type nitride MoN emerge.

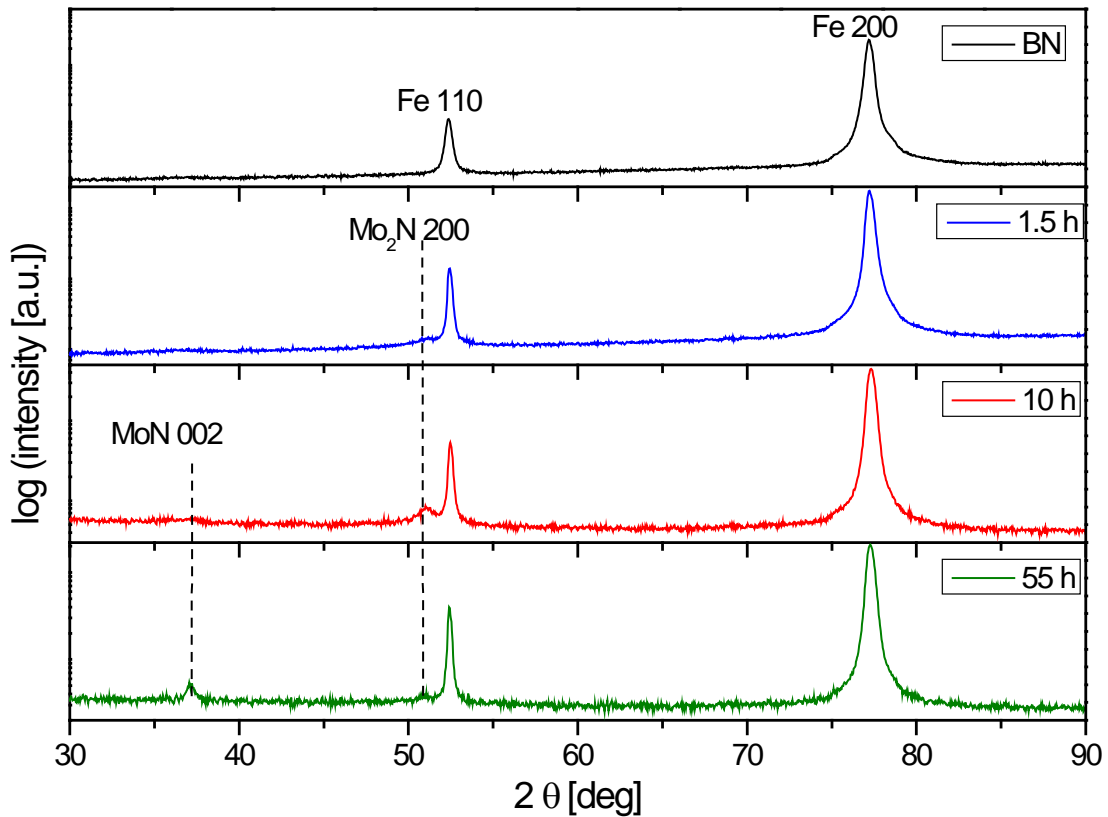


Fig. 2.18: X-ray diffraction patterns of the cold rolled specimen before nitriding (BN) and after nitriding for 1.5 h, 10 h and 55 h at 580 °C.

Confirmation of the more incoherent nature of the Mo₂N-type precipitates in the cold rolled alloy is also obtained from the microhardness data (see Fig. 2.19). The maximum hardness increase is reached after a relatively short nitriding time (about 10 h) and amounts to about 200 HV0.05. Compared to the maximum hardness increase for the recrystallized specimen due to Mo₂N-type precipitation (see Fig. 2.1) this hardness increase is smaller, which is compatible with the observation of, likely at least partially, incoherent Mo₂N-type precipitates in case of the cold rolled specimens.

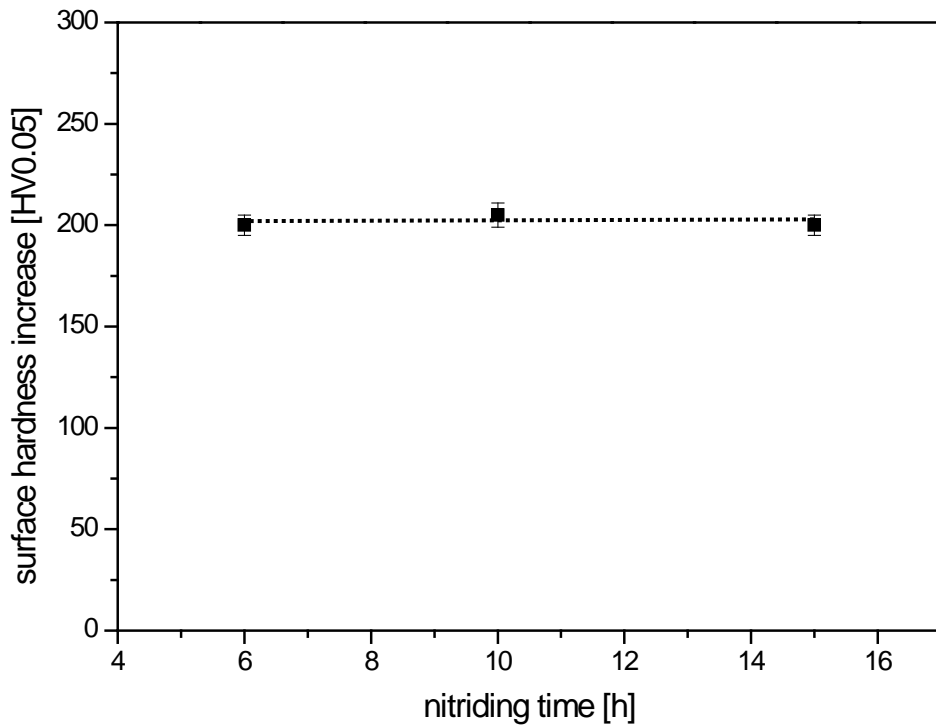


Fig. 2.19: Increase of surface microhardness, as compared to the initial, cold rolled state, as function of nitriding time at 580 °C. Dotted line has been drawn to guide the eye.

2.3.2.3 Nitrogen uptake

The mass increase as function of nitriding time is shown in Fig. 2.20. The time required to saturate a pure ferrite specimen of the same thickness (approximately 120 μm) applying the same nitriding conditions would amount to about 5 h.

The solubility limit of nitrogen in the (Mo-containing) ferritic matrix is already surpassed after a nitriding time of less than 5 h (for the recrystallized specimens this took about 20 h), suggesting that Mo₂N-type precipitation takes place much faster in the cold rolled specimen.

In order to precipitate all Mo present in the specimen as Mo₂N an amount of 0.5 at.% N is needed. Adding this amount of nitrogen to that which can be dissolved in the unstrained ferritic matrix at 580 °C (about 0.3 at.%, [9]), an overall nitrogen concentration of 0.8 at.% is expected if all Mo has precipitated as Mo₂N. This nitrogen level is already exceeded after a nitriding time of 8 h. The MoN-type precipitates appear earlier in case of the cold rolled specimen than in the recrystallized specimen (cf. Figs. 2.12 and 2.18), which can be a direct consequence of the much faster precipitation of the Mo₂N-type precipitates in the cold rolled specimens (see above). Yet, as compared to the recrystallized specimens (cf. Fig. 2.15), the nitrogen-uptake curve for the cold rolled specimen (Fig. 2.20) suggests an only partial and in any case very slow Mo₂N → MoN transformation. Recognizing the much lesser degree of coherency (and thus the much smaller amounts of (misfit-) strain energy and nitrogen supersaturation) for the Mo₂N-type precipitates in the deformed specimen, it can be understood that the driving force for a discontinuous precipitation, as discussed in section 2.3.1.4 for the undeformed specimens, is much smaller for the deformed specimens. Thus, the fraction of the specimen volume subjected to the discontinuous transformation and thereby the total amount of nitrogen taken up by the deformed specimens at saturation can be distinctly smaller for the deformed specimens than for the undeformed specimens (cf. horizontal asymptotes in Figs. 2.15 and 2.20).

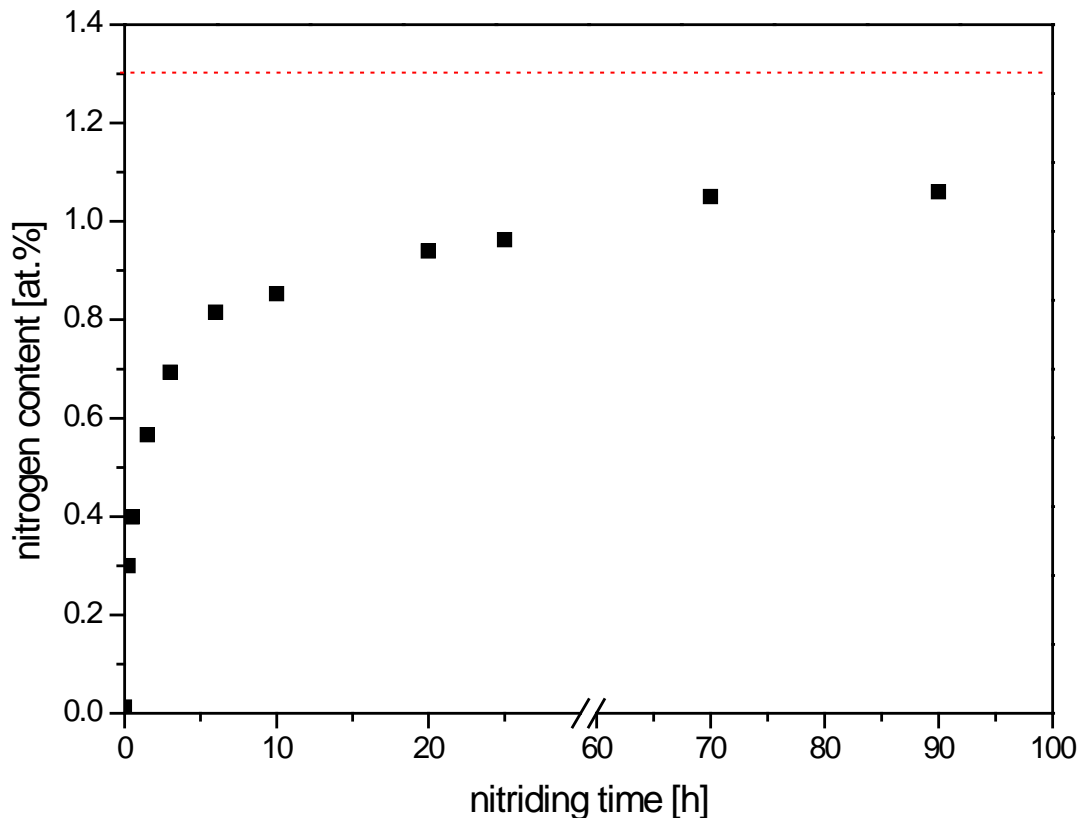


Fig. 2.20: Nitrogen uptake as function of nitriding time at 580 °C for the cold rolled specimen. The red dotted line represents the calculated nitrogen content under the assumption that all molybdenum in the specimen precipitates as MoN plus the amount of nitrogen that can be dissolved in the unstrained, ferritic matrix.

2.4 Conclusions

The nitride-precipitation process in recrystallized and cold rolled Fe-1at.%Mo alloy upon nitriding can be described as follows:

- First, the nitrogen content increases rapidly until nitrogen saturation of the ferrite matrix has been realized.
- Then, development of cubic Mo₂N-type precipitates as platelets of several hundreds of nm length and thickness of a few atomic layers occurs according to a Bain-type orientation relationship. In case of the recrystallized specimens the platelets are largely coherent (diffracting coherently with the matrix) giving rise to strongly asymmetric ferrite-matrix diffraction peaks. In case of the cold rolled

- specimens development of the Mo₂N-type precipitation occurs much earlier and the nitride platelets are at least partially incoherent (giving rise to separate nitride reflections in the diffraction patterns).
- Upon prolonged treatment a discontinuous precipitation reaction initiating at ferrite-matrix grain boundaries takes place replacing the submicroscopical Mo₂N-type platelets by a lamellar α -Fe/MoN (hexagonal) microstructure with a Burgers-type orientation relationship, involving parallelism of close packed planes in both phases. In case of the recrystallized specimens the discontinuous precipitation reaction eventually brings about a full transformation of Mo₂N-type precipitates to MoN-type precipitates. In case of the cold rolled specimens the Mo₂N \rightarrow MoN transformation occurs only partially: the driving force for the discontinuous precipitation reaction is much smaller in case of the cold rolled specimen (much less (misfit-) strain energy and nitrogen supersaturation).
 - The discontinuous transformation leads to a pronounced increase in the nitrogen concentration upon transformation due to the change in stoichiometry (Mo₂N \rightarrow MoN).
 - The composition analysis of the Mo₂N-type nitrides (submicroscopical) and of the MoN-type nitrides (lamellae) suggests no incorporation of significant amounts of Fe in the nitrides. Such earlier data all derive from FIM-atom probe analyses, which may have been affected by loss of spatial resolution.

CHAPTER 3

Defect-dependent nitride surface-layer development upon nitriding of Fe-1 at.% Mo alloys

H. Selg, E. Bischoff, I. Bernstein, T. Woehrle, S. Meka, R. Schacherl, T. Waldenmaier,
E.J. Mittemeijer

Abstract

Upon nitriding of binary Fe-1at.% Mo alloy in a NH_3/H_2 gas mixture under conditions (thermodynamically) allowing γ' - $\text{Fe}_4\text{N}_{1-x}$ compound-layer growth (nitriding potential: $0.7 \text{ atm}^{-1/2}$ at 753 K (480 °C) – 823 K (550 °C)) a strong dependency of the morphology of the formed compound layer on the defect density of the specimen was observed. Nitriding of *cold rolled* Fe-1at.% Mo specimens leads to the formation of a closed compound layer of approximately constant thickness, comparable to nitriding of pure iron. Within the compound layer, i.e. in the near-surface region, Mo nitrides are present. The growth of the compound layer could be described by a modified parabolic growth law leading to an activation energy comparable to literature data for the activation energy of growth of a γ' - $\text{Fe}_4\text{N}_{1-x}$ layer on pure iron. Upon low temperature nitriding (i.e. $\leq 793 \text{ K}$ (520 °C)) of *recrystallized* Fe-1at.%Mo specimens an irregular, “needle-like” morphology of γ' - $\text{Fe}_4\text{N}_{1-x}$ nucleated at the surface occurs. This γ' iron nitride has an orientation relationship (OR) with the matrix close to the Nishiyama-Wassermann OR. The different morphologies of the formed compound layer can be interpreted as consequences of the ease or difficulty of precipitation of Mo as nitride as function of the defect density.

3.1 Introduction

Thermochemical heat treatments are widely applied in industry in order to improve the surface properties of iron-based components. Gaseous nitriding is one of the most important of such treatments leading to pronouncedly improved mechanical (e.g. fatigue, wear) and chemical (e.g. corrosion) properties of ferritic steel components and work pieces in many practical applications [43, 60]. Upon nitriding, nitrogen atoms diffuse into the surface of the specimen. As a nitrogen donator, ammonia can be used, due to its dissociation at the surface of iron-based alloys, leading to the development of a nitrided zone at and beneath the surface. Gaseous nitriding, by employing a gas atmosphere composed of ammonia and hydrogen, allows an accurate control of the chemical potential of nitrogen in the nitriding atmosphere. The nitriding potential $r_N = \frac{P_{NH_3}}{P_{H_2}^{3/2}}$ is proportional to the chemical potential/activity of nitrogen in the atmosphere

[61]. If it is assumed that the chemical potential of nitrogen in the gas atmosphere is equal to the chemical potential of nitrogen absorbed at the surface (then so-called local equilibrium prevails), the nitrogen uptake can be adjusted very precisely by control of the composition of the gas atmosphere at constant temperature and pressure [9]. The nitrided layer itself, depending on the nitriding conditions [10, 23] can be subdivided into a compound layer adjacent to the surface, composed of iron nitrides and a diffusion zone beneath the compound layer. Within the diffusion zone, nitrogen is dissolved in the octahedral interstices of the ferrite lattice, or precipitated as internal nitrides MeN_x if nitride forming elements, such as $Me = Ti, Cr, Al, V$ are present [7, 16, 19, 45].

Recent work has shown that the presence of nitride forming alloying elements can have a significant influence on the nucleation and growth behaviour of compound layers consisting of γ' - Fe_4N_{1-x} ; an unusual needle-like morphology was obtained in the presence of Al as alloying element [62].

Usually, Mo is not added deliberately to nitriding steels to promote precipitation of molybdenum nitride but it is often present to improve the tempering brittleness, strength and weldability [46]. Against this background in this work the influence of Mo

on the nucleation and growth behaviour of a nitride surface layer on a Fe-Mo alloy substrate, and in particular its dependency on the defect density of the alloy substrate, was investigated.

3.2 Experimental

3.2.1 Specimen preparation

For the production of an alloy with the composition Fe-1at.% Mo appropriate amounts of pure iron (99.98 wt.%) and pure molybdenum (99.99 wt.%) were weighed, pre-alloyed in an arc furnace and melted in an Al₂O₃ crucible by means of an inductive furnace under a protective argon gas atmosphere (99.999 vol.%). The melt was cast in a copper mould to obtain a cylindrical rod (\varnothing : 10 mm, *l*: 100 mm). The chemical composition and the amounts of impurities were determined using chemical analysis (inductively coupled plasma - optical emission spectroscopy, combustion method and carrier gas hot extraction). The results are shown in Table 3.1.

Table 3.1: Amounts of Mo and light element impurities for the alloy used in this work (balance: Fe).

Element	Mo	O	N	C	S
content [wt.%]	1.800 ± 0.02	0.009 ± 0.002	0.003 ± 0.001	0.006 ± 0.001	<0.001
content [at.%]	1.057 ± 0.012	0.032 ± 0.007	0.012 ± 0.004	0.028 ± 0.005	<0.002

After casting the rod was cut into 3 pieces and their shells were removed by grinding. These pieces were cleaned with ethanol in an ultrasonic bath before cold rolling to sheets of a thickness of about 1 mm (degree of deformation: 90 %). Out of these sheets, rectangular specimens were cut (dimensions: about 15 x 10 mm²) and a hole was drilled (\varnothing : 1.5 mm) for fixing it later during heat treatment. The specimens were ground, cleaned in an ultrasonic bath using ethanol and then encapsulated in a quartz tube

which was filled with argon gas (purity: 99.999 vol.%). Subsequently, half of the specimens were recrystallized in a muffle furnace at 1073 K (800 °C) for 90 min.

3.2.2 Nitriding

Before nitriding, the specimen surfaces were polished mechanically (final step: 1 μm diamond suspension), cleaned with ethanol in an ultrasonic bath and dried in a nitrogen gas flow. The nitriding experiments were performed at three different temperatures (753 K (480 °C), 793 K (520 °C) and 823 K (550 °C) \pm 1 K) in a vertical, multizone quartz-tube furnace (\varnothing : 28 mm) with a NH_3/H_2 gas mixture using a flux of 500 ml/min (purity NH_3 : > 99.998 vol.%, purity H_2 : 99.999 vol.%). The gas fluxes were adjusted by mass flow controllers and corresponded to a nitriding potential of $r_N = 0.7 \text{ atm}^{-1/2}$ allowing development of γ' -iron nitride at the surface [9]. The nitriding process was terminated by breaking mechanically the quartz fibre at which the specimen was suspended in the furnace so that the specimen fell through an opened valve into a flask filled with water, flushed with N_2 , where the specimen was quenched to room temperature.

3.2.3 Specimen characterization

3.2.3.1 X-ray diffractometry

Phase analysis by means of X-ray diffraction was performed for the surfaces of all specimens before and after nitriding by using a PANalytical X'Pert Multi-Purpose Diffractometer (MPD) and Co-K_α radiation. This instrument uses Bragg-Brentano geometry and is equipped with a graphite monochromator in the diffracted beam. The diffraction-angle range ($30^\circ < 2\theta < 120^\circ$) was scanned in steps of $0.06^\circ 2\theta$ with a counting time of 320 s per step. For the identification of the phases, based on the positions of the diffraction peaks, data of the ICDD database were used [51].

Glancing angle X-ray diffraction measurements (for enhanced surface sensitivity) were performed by using a PANalytical X'Pert Materials Research Diffractometer (MRD), equipped with an Eulerian cradle and a graphite monochromator in the diffracted beam,

applying parallel beam geometry and Cu-K α radiation. The diffraction-angle range ($30^\circ < 2\theta < 90^\circ$) was scanned in steps of $0.06^\circ 2\theta$ with a counting time of 30 s per step.

3.2.3.2 Electron probe microanalysis

For the determination of the nitrogen concentration-depth profiles electron probe microanalysis (EPMA) was performed on polished cross sections of the specimens which were embedded in Struers PolyFast (final polishing step $1\ \mu\text{m}$ diamond suspension). For these measurements, a Cameca SX100 microprobe (acceleration voltage $U_a = 10\ \text{kV}$, current $I = 100\ \text{nA}$, spot size about $1\ \mu\text{m}$) equipped with five wavelength-dispersive spectrometers was used. The line scans performed on the cross sections started at the surface proceeding perpendicular to the surface towards the centre of the specimen. To obtain the element contents at each measurement point, the intensities of the characteristic X-ray emission peaks were measured and divided by the corresponding intensities obtained from standard samples of pure Fe, Mo and γ' -Fe $_4$ N (for N-K α). Elemental concentrations were calculated from the intensity ratios applying the $\Phi(\rho z)$ approach according to Pouchou and Pichoir [50].

3.2.3.3 Auger electron spectroscopy

Auger electron spectroscopy (AES) line scans were performed on polished cross sections (final polishing step $0.25\ \mu\text{m}$ diamond suspension) to determine the element concentrations across a sharp interface between the nitride surface layer and the substrate. For this purpose, an Auger microscope (JEOL JAMP-7830F operating at 10 kV and 15 nA to 70 nA) was used. AES analysis was carried out employing a focused electron beam with a diameter of about 30 nm. The element concentrations were measured after sputter cleaning of the cross-sectional surface using an Ar $^+$ ion beam (0.5 keV).

3.2.3.4 Light microscopy (LM) and microhardness measurement

For LM investigations a piece of each nitrided specimen was cut off (Struers Accutom 50, Al₂O₃ cut-off wheel), embedded in Struers PolyFast, ground and polished (final polishing step: 1 µm diamond suspension). In order to avoid spalling of the brittle compound-layer upon cross-section preparation (grinding and polishing), the specimen were nickel-plated prior to embedding. Each cross-section was etched with 2 % Nital (2 vol.% HNO₃ in ethanol) at room temperature for about 10 s. LM micrographs were taken using a Zeiss Axiophot microscope equipped with a digital camera (Olympus ColorView IIIu). The thickness of the nitrided layer was measured applying the software analySIS docu.

Microhardness measurements on cross sections of nitrided specimens were carried out with a Vickers microhardness tester (Leica VMHT Mot) applying a load of 490 mN and a dwell time of 10 s.

3.2.3.5 Electron backscatter diffraction

Electron Backscatter Diffraction (EBSD) was performed on polished cross-sections of the specimens (final polishing step: 0.05 µm OPS-suspension) with a Zeiss Leo 438 VP scanning electron microscope equipped with an EDAX TSL EBSD measurement system. The data were analysed using the software OIM version 5.

3.3 Cold rolled specimens; results and discussion

3.3.1 X-ray diffraction; phase analysis

Diffraction patterns recorded from specimens nitrided at 753 K (480 °C) for different times are shown in Fig. 3.1. A distinct, typical 100 rolling-texture is revealed as indicated by the intensity-dominance of the 200 reflection (Fig. 3.1). Evidently, nitriding of cold rolled Fe-1at.% Mo alloys at the temperature of 753 K (480 °C), using a nitriding potential of $0.7 \text{ atm}^{-1/2}$, leads to the formation of γ' -Fe₄N_{1-x} (primitive cubic; fcc Fe-sublattice).

The development of molybdenum nitrides in the ferrite matrix is revealed by the asymmetry of especially the α -Fe (ferrite) 200 reflection, as compared to the more symmetrical α -Fe 110 and 211 reflections: the occurrence of coherent Mo-nitride precipitates leads to an anisotropically, tetragonally distorted ferrite matrix due to the mismatch between ferrite matrix and nitride platelets. This results in the appearance of strongly broadened tetragonal (200/002) doublets in the diffraction patterns due to coherent diffraction from the platelets with the surrounding matrix [16, 45]). This asymmetric broadening decreases with increasing nitriding time as the nitrides become more and more semi- (or even in-) coherent and therefore inducing less tetragonal distortion. Eventually, the molybdenum nitrides diffract separately (i.e. incoherently with the matrix). Indeed, after the longest nitriding time of 64 h, the presence of Mo₂N is indicated by a small reflection at a diffraction angle of $2\theta = 50.9^\circ$.

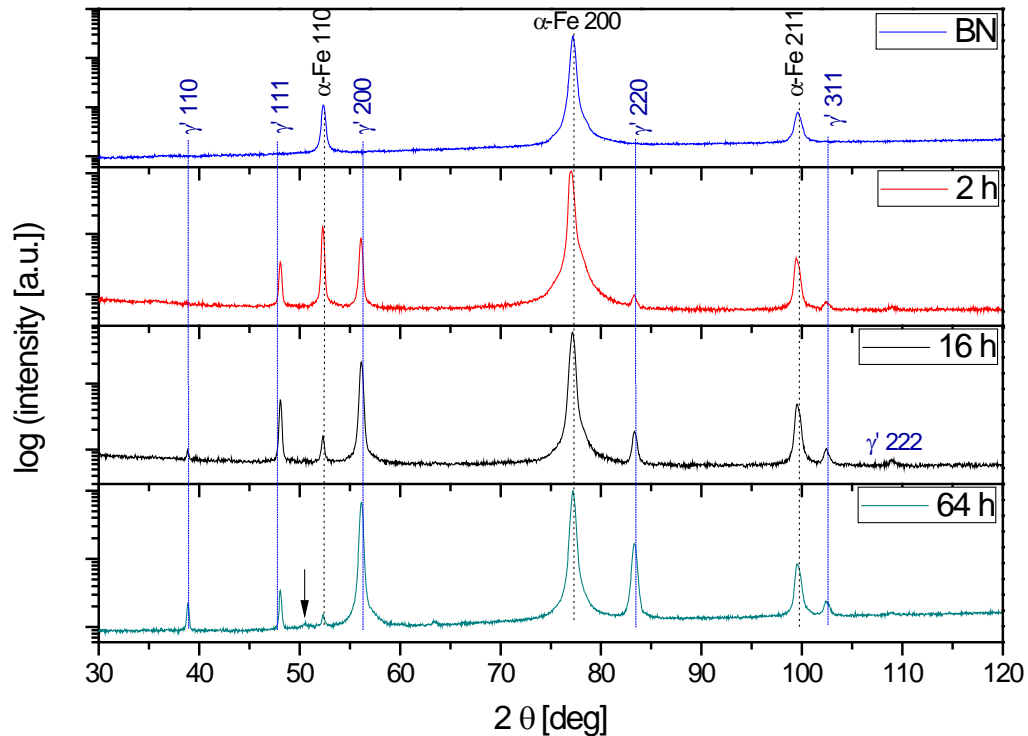


Fig. 3.1: X-ray diffraction patterns (Co- K_{α} radiation) of the cold rolled specimen before nitriding (BN) and after nitriding for different times at 753 K (480 °C) using a nitriding potential of 0.7 atm^{-1/2}. Dotted lines indicate reflection positions according to the ICDD database [51]. The black arrow marks the position of the Mo_2N 200 reflection.

The glancing angle diffraction pattern (angle of incidence: 3°, thus limiting the penetration depth to 1.5 microns (the Cu- K_{α} radiation used here is close to an absorption edge of iron, thus (further) limiting the penetration depth)) recorded after a nitriding time of 2 h (cf. Fig. 3.2), reveals that, upon nitriding of cold rolled Fe-1at.% Mo alloy, apart from γ' - $\text{Fe}_4\text{N}_{1-x}$ reflections, also reflections from ε - Fe_{2-3}N can be discerned in the early stage of nitriding, although the nitriding experiments were carried out in the γ' region of the Lehrer diagram. The ε reflections disappear upon continued nitriding. This could hint at a higher solubility of Mo in ε than in γ' , which could promote ε to form in the beginning of nitriding. Moreover, extra diffraction peaks appear in the diffractogram (cf. Fig. 3.2 after 2 h and 4 h of nitriding) that cannot be indexed according to any of the known (Fe, Mo)N phases. The reflections of this phase also disappear upon continued nitriding (cf. Fig. 3.2). This metastable phase could thus act as a “precursor” for the

formation of the later emerging binary Mo-nitrides (see Fig. 3.2 after 4 h and 16 h). Hence, the nucleation process of the compound layer may be described as follows: at the beginning of nitriding of cold rolled Fe-1at% Mo alloy, next to γ' ϵ and an unknown precursor phase are formed to incorporate the Mo that cannot dissolve in γ' . In the later stage of nitriding, Mo-nitride (Mo_2N) is formed, upon dissolution of the ϵ phase and the precursor phase which are thermodynamically unstable under the chosen nitriding conditions. For the later stage of growth of the γ' layer into the substrate, the Mo, originally dissolved in the ferrite matrix, has precipitated as Mo nitride already and these Mo nitride particles are then encompassed by the growing γ' layer (as shown in the next section 3.3.2).

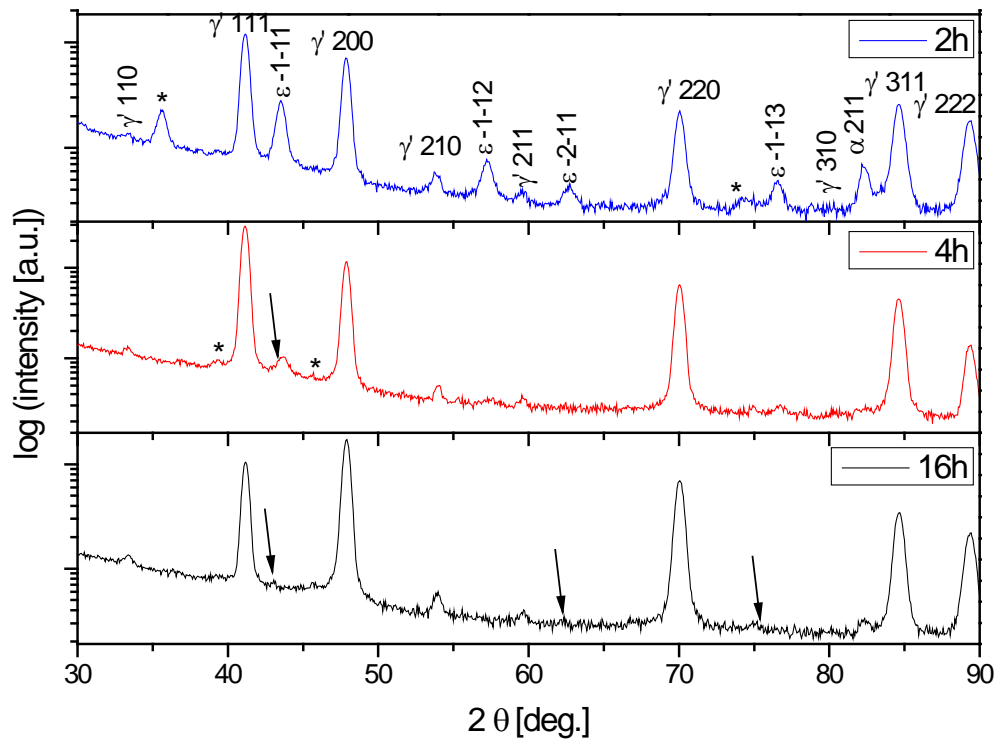


Fig. 3.2: Glancing angle X-ray diffraction patterns (Cu-K_α radiation) recorded from the surface of cold rolled specimens nitrided at 793 K (520 °C) for 2 h, 4 h and 16 h. Reflections arising from γ' - $\text{Fe}_4\text{N}_{1-x}$, ϵ - Fe_{2-3}N , Mo_2N (reflection positions indicated by a black arrow) and an unknown phase (reflection positions indicated by a star) can be discerned.

3.3.2 Microstructure; growth of the γ' -Fe₄N_{1-x} layer

Nitriding of cold rolled Fe-1at.% Mo alloy specimen using a nitriding potential of $0.7 \text{ atm}^{-1/2}$ leads to the formation of a closed compound layer, similar to that observed in the case of nitriding pure iron [63]. The thickness of the compound layer increases with increasing nitriding time and temperature (Figs. 3.3a-f). Some variation in the layer thickness could be due to the intrinsic inhomogeneity of the deformation by cold rolling (cf. section 3.2.1): locally enhanced dislocation density can be associated with enhanced nitride nucleation [64].

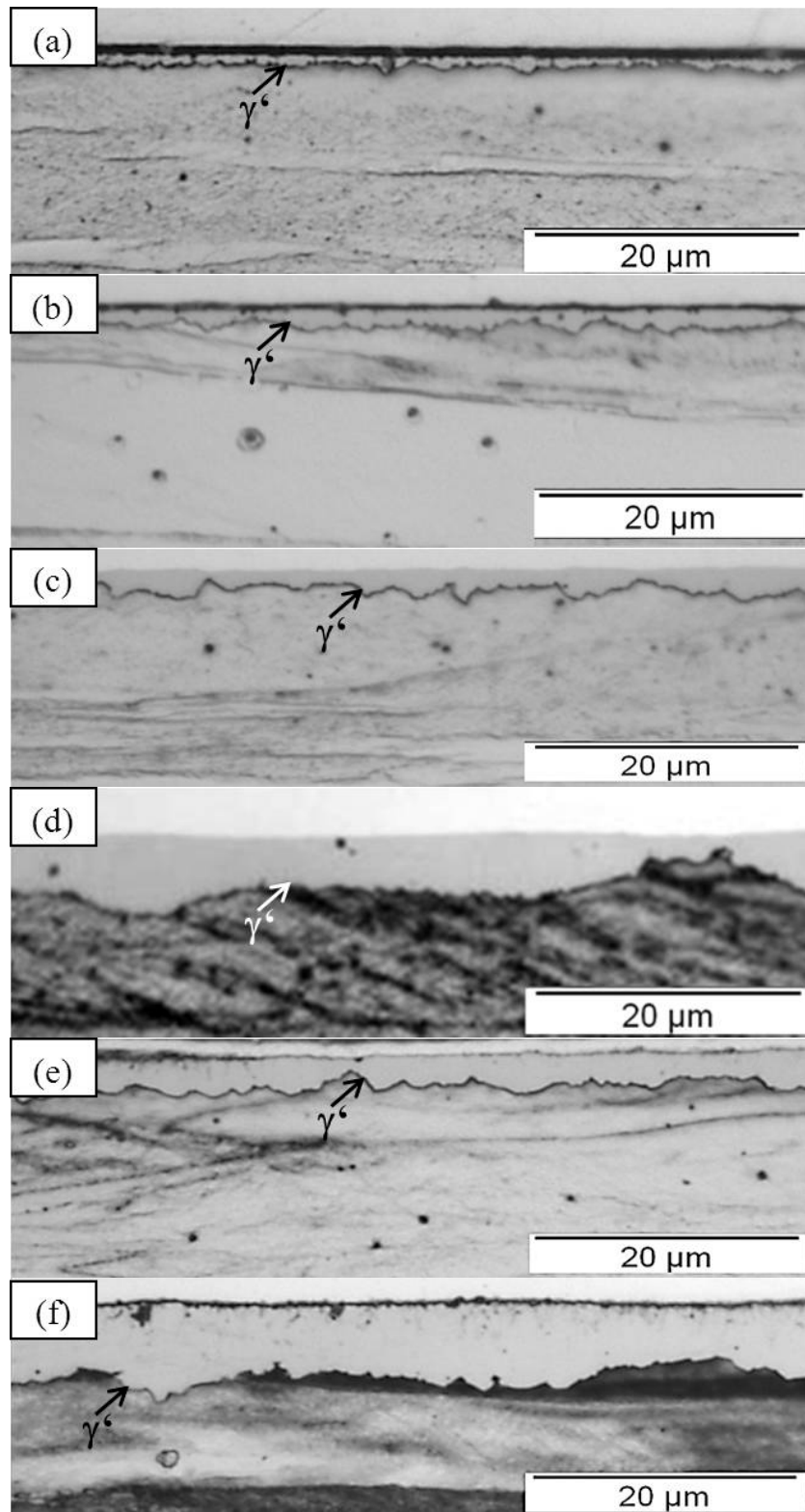


Fig. 3.3: LM micrographs of the cold rolled specimens (a) nitrided for 4 h at 753 K (480 °C), (b) nitrided for 16 h at 753 K (480 °C), (c) nitrided for 4 h at 793 K (520 °C), (d) nitrided for 16 h at 793 K (520 °C), (e) nitrided for 4 h at 823 K (550 °C) and (f) nitrided for 16 h at 823 K (550 °C).

EBSD analyses demonstrate that the grain size of the γ' -nitride grains in the compound layer decreases with increasing nitriding temperature (cf. Figs. 3.4a and b). Further, the EBSD analyses revealed that there is no preferred orientation relationship between the ferritic matrix and the γ' nitride.

As follows from Figs. 3.4a and b, γ' -nitride is not only formed at the surface, but also in the diffusion zone underneath. For discussion, see section 3.4.2.

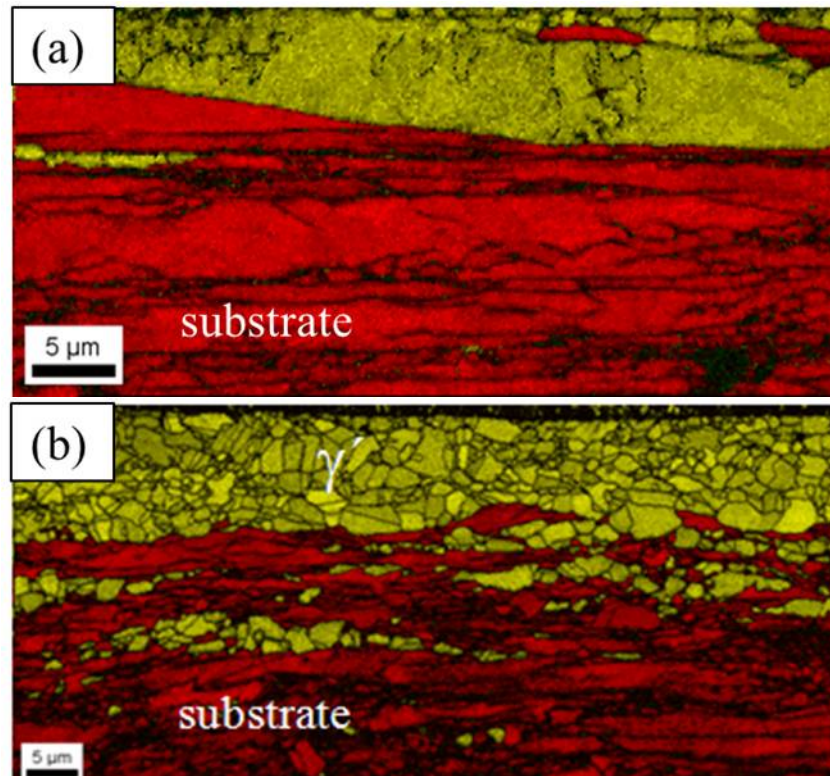


Fig. 3.4: EBSD images (phase maps) obtained after a nitriding time of 64 h (a) at 753 K (480 °C) and (b) at 823 K (550 °C). The Fe-substrate (bcc crystal structure) is indicated by red colour in the phase map, whereas the γ' iron nitride (fcc crystal structure) is colour-coded in yellow.

The nitrogen concentration-depth profile (determined by EPMA) of a specimen nitrided for 64 h at a temperature of 793 K (520 °C) (nitriding potential: $0.7 \text{ atm}^{-1/2}$) is shown in Fig. 3.5, on top of the image of the corresponding cross section recorded by light microscopy. The nitrogen concentration in the matrix (average value: 0.8 at.%) exceeds distinctly the solubility limit of nitrogen in pure ferrite for the concerned

temperature of 793 K (520 °C) (0.3 at.% [9]). This can be explained by Mo precipitated as nitride in the matrix at some depth from the surface prior to, or at the same time as, the begin of the formation of γ' -nitride at the surface (see discussion in section 3.3.1). This precipitation of Mo as nitride occurs usually at a relatively low rate due to the high volumetric misfit of the nitride with the matrix. The presence of a high density of defects, such as dislocations accelerates the precipitation of molybdenum nitride [65]. This result indicates that, after some time of nitriding, Mo has precipitated (pronouncedly) in the matrix as nitride before γ' growing from the surface arrives and “overruns” the Mo nitride in the substrate. The deviation between the Mo content in the ferrite matrix and the Mo content in the γ' phase is caused by the local increase of nitrogen at the location of the γ' phase as compared to the ferrite matrix: If 20 at.% N are added to an originally binary Fe-1at.% Mo alloy, the atomic concentration of Mo is reduced by 1/5, without that a redistribution (transport) of Mo has occurred, i.e. the atomic concentration in γ' then should be 0.8 at.%, as observed (see Fig. 3.5).

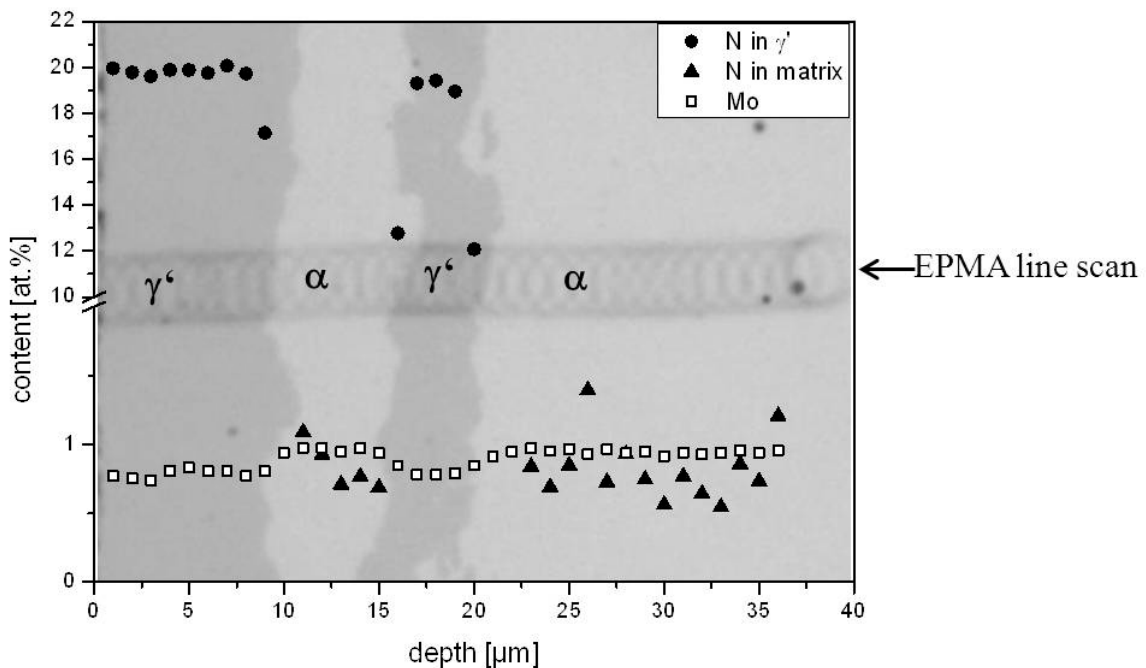


Fig. 3.5: Nitrogen concentration-depth profile (EPMA) of the specimen nitrided for 64 h at 793 K (520 °C) using a nitriding potential of $0.7 \text{ atm}^{-1/2}$, superimposed on the corresponding LM micrograph.

3.3.3 γ' -nitride layer-growth kinetics

On three micrographs of each cold rolled specimen nitrided at different temperatures, the thickness of the grown γ' -layer was measured using the software analySIS docu. From each micrograph 200 values for the thickness were obtained and the squared arithmetically averaged thickness was plotted vs. the treatment time for all temperatures. A parabolic relationship between layer thickness and treatment time is expected as the growth of the γ' -nitride layer is likely controlled by the inward diffusion of nitrogen [63]. Thus, a plot of the squared layer thickness versus the treatment time should result in a straight line. Such a relationship is indeed observed for treatment times larger than 2 h (see Fig. 3.6). At the beginning of the nitriding process ($t < 2$ h) the γ' -layer grows slower than indicated by the parabolic relation observed for longer times and indicated with the straight line passing through the origin of the plot¹. This can be discussed as follows: At the beginning of nitriding (a large part of) the inwardly diffusing nitrogen is consumed by Mo in the surface adjacent region to precipitate as molybdenum nitride thereby delaying the development of γ' at the surface. To account for this initial delay in the development of γ' a modified parabolic layer growth law is fitted to the experimental data:

$$S^2(t) = kt + S_0^2 \text{ (for } t \geq 2 \text{ h)}, \quad (3.1)$$

where S denotes the γ' -layer thickness at time t , k is the growth constant, t is the treatment time and S_0 represents the virtual layer thickness at $t=0$.

¹ This contrasts with what is observed for γ' -layer growth on pure iron, where growth of γ' in the first stage of nitriding, where no closed layer of γ' nitride occurs at the surface, is relatively fast, as the nitrogen follows a short-circuit path through the ferrite matrix, by-passing diffusion through the already formed γ' nuclei (diffusion of N through ferrite is much faster than through γ' nitride) [63].

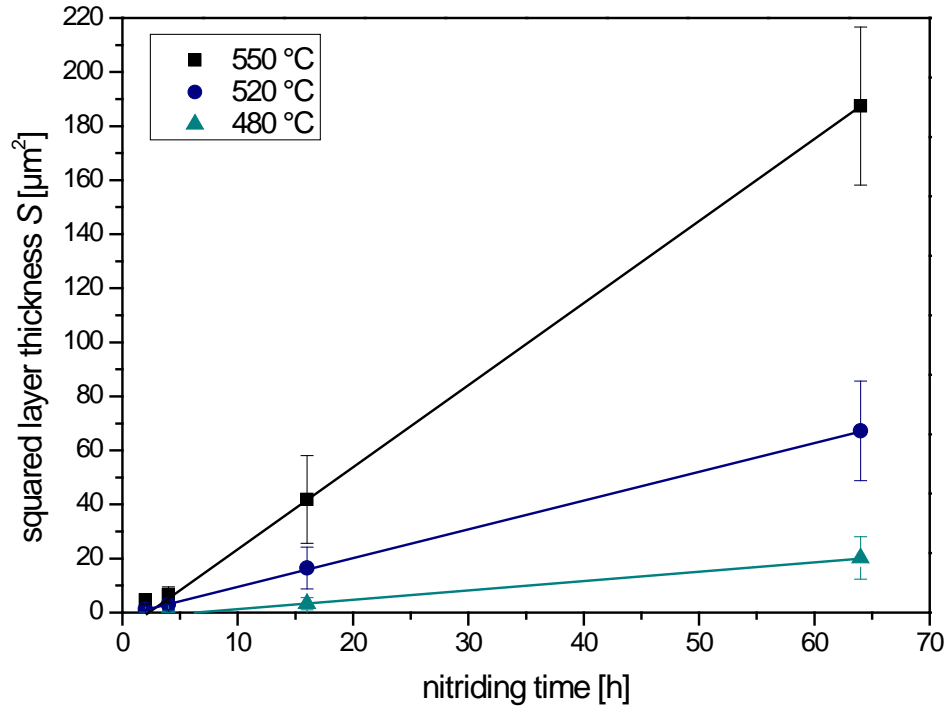


Fig. 3.6: Squared thickness of the γ' -nitride layer as function of nitriding time for three different temperatures (753 K (480 °C), 793 K (520 °C), 823 K (550 °C)) obeying a parabolic relationship (cf. Eq. (3.1)) indicated by the straight lines fitted to the data at each temperature for $t \geq 2$ h (see text).

From the slope and the intercept of the fitted straight lines to the data at each temperature in Fig. 3.6, values for the growth constant k and the virtual initial layer thickness S_0 were obtained (see Table 3.2). The growth constant for γ' -nitride growing on pure iron [66] is of the same order as that of the calculated values for the present alloy system.

Table 3.2: Growth constant k and hypothetical initial layer thickness S_0 , determined from the slopes of the straight lines in Fig. 3.6.

treatment temperature [K]	growth constant, k [$10^{-4} \mu\text{m}^2/\text{s}$]	hypothetical initial layer thickness, S_0 [μm]
753	0.9 ± 0.05	-0.97 ± 0.53
793	2.9 ± 0.02	-0.93 ± 0.24
823	8.3 ± 0.14	-3.98 ± 1.66

The growth constant k in the parabolic growth law can be interpreted using a growth model [63] subject to the following assumptions:

- i) the surface of the compound layer and the interface between compound layer and ferritic matrix are planar and parallel;
- ii) the nitrogen concentrations in γ' at the γ' /gas interface and at the γ'/α interface are constant and correspond with local thermodynamic equilibrium.

The flux of nitrogen, $J_N^{(\gamma')}$, in γ' (for one-dimensional diffusion) complies with Fick's first law [67] according to

$$J_N^{(\gamma')} = -c_N^{(\gamma')} M_N^{(\gamma')} \frac{d\mu_N^{(\gamma')}}{dx} = -c_N^{(\gamma')} M_N^{(\gamma')} RT \frac{d \ln a_N^{(\gamma')}}{dx} = -c_N^{(\gamma')} D_N^{(\gamma')*} \frac{d \ln a_N^{(\gamma')}}{dx} \quad (3.2)$$

where $M_N^{(\gamma')}$ is the mobility of nitrogen in γ' , $\mu_N^{(\gamma')}$ is the chemical potential of nitrogen in γ' , x the depth coordinate, R the gas constant, T the treatment temperature, $a_N^{(\gamma')}$ the activity and $c_N^{(\gamma')}$ the concentration of nitrogen in γ' and $D_N^{(\gamma')*}$ denotes the self-diffusion coefficient of N in γ' . Note that the diffusion of iron atoms can be neglected at the nitriding temperature, i.e. $D_{Fe}^{(\gamma')} \approx 0$.

Under the assumption of quasi-steady state diffusion of nitrogen in γ'^2 , equation (3.2) can be written as [68]

$$J_N^{(\gamma')} = -D_N^{(\gamma')*} \frac{c_N^{(\gamma')} \Delta \ln a_N^{(\gamma')}}{S} \quad (3.3)$$

where $D_N^{(\gamma')*}$ and $c_N^{(\gamma')}$ must be interpreted as effective values (constants over the layer thickness S). $\Delta \ln a_N^{(\gamma')}$ denotes the change in nitrogen activity across the γ' layer, i.e. from the gas phase/ γ' surface to the γ'/α interface.

² In quasi-steady-state diffusion, at a given time the diffusive flux through the growing γ' layer, $J_N^{(\gamma')}$, is constant throughout the γ' layer and its instantaneous value depends only on the actual layer thickness. This approximation is valid because of the very small composition range of γ' iron nitride and the large concentration difference between the γ' layer and the α -iron substrate, as confirmed by numerical calculations [68].

The growth of the γ' layer, given by the shift of the γ'/α interface, follows from a flux balance equation at the shifting γ'/α interface [63, 68, 69]:

$$v^{\gamma'/\alpha} \left(c_N^{\gamma'/\alpha} - c_N^{\alpha/\gamma'} \right) = J_N^{\gamma'/\text{gas}} - J_N^{\alpha/\gamma'} \quad (3.4)$$

where $c_N^{I/II}$ denotes the concentration of nitrogen in phase I at the interface between I and II ($I, II \in \{\gamma', \alpha\}$) expressed as quantity per unit volume and $v^{\gamma'/\alpha}$ is the growth rate of the γ'/α interface. The growth rate can be expressed as

$$v^{\gamma'/\alpha} = \frac{dS}{dt} \quad (3.5)$$

Assuming that the matrix has been saturated with nitrogen and all Mo has precipitated in the matrix as nitride, the flux of nitrogen in the matrix can be neglected, i.e. $J_N^{\alpha/\gamma'} = 0$. To account for this, only values for the parabolic growth constant pertaining to a nitriding time of $t \geq 16$ h were considered (it was verified that, within experimental accuracy, no change in hardness, measured over the entire cross section of the specimen, occurred between 16 h and 64 h, i.e. the matrix was nitrogen saturated after 16 h of nitriding).

Then, combining Eqs. (3.1), (3.3), (3.4) and (3.5), an expression for the growth constant k is obtained:

$$k = \frac{2D_N^{(\gamma')*} c_N^{(\gamma')}}{\left(c_N^{\gamma'/\alpha} - c_N^{\alpha/\gamma'} \right)} \Delta \ln a_N^{\gamma'} \quad (3.6)$$

The molar concentration of N in γ' and in α -Fe can be expressed as

$$C_N^i = \frac{u_N^i}{N_{Av} \cdot V} \quad (3.7)$$

with the atomic ratio u_N^i of N in phase i ($i \in \{\gamma', \alpha\}$), denoting the number of nitrogen atoms divided by the number of iron atoms in a unit cell of phase i and where N_{Av} denotes Avogadro's constant and V is the volume of the unit cell of phase i per Fe atom.

As $c_N^{(\gamma')} \approx c_N^{\gamma'/\alpha} \gg c_N^{\alpha/\gamma'}$ ($c_N^{\gamma'/\alpha} = 30292$ mole/m³; $c_N^{\alpha/\gamma'} = 1120$ mole/m³), it follows from Eq. (3.6):

$$k \approx 2(\Delta \ln a_N^{\gamma'}) D_N^{(\gamma')*} \quad (3.8).$$

The activity $a_N^{\gamma'}$ of nitrogen in a γ' phase, in equilibrium with a nitriding (NH_3/H_2) atmosphere of nitriding potential r_N , is given by [9]

$$a_N^{(\gamma')} = (p_{\text{N}_2}^0)^{-1/2} K \cdot r_N \quad (3.9)$$

with $p_{\text{N}_2}^0$ denoting nitrogen gas at atmospheric pressure and at the temperature concerned as the reference state, K as the equilibrium constant for the (thermal) decomposition of ammonia, and thus

$$k \approx 2(\Delta \ln r_N) D_N^{(\gamma')*} \quad (3.10)$$

where $\Delta \ln r_N$ denotes the difference in nitriding potential (activity; cf. Eq. (3.8)) of nitrogen in the γ' layer at the (gas phase/ γ') surface and of nitrogen at the γ'/α interface.

Hence, the (effective; see above) self-diffusion coefficient of nitrogen in γ' , $D_N^{(\gamma')*}$, can be calculated from the experimentally determined layer-growth constant, k , the nitriding potential of the applied gas atmosphere, $r_N^{\text{gas}/\gamma'}$, and the nitriding potential at the interface between γ' and α (temperature dependent), $r_N^{\gamma'/\alpha}$, calculated using literature data [70]. Adopting an Arrhenius-type temperature dependency for the self-diffusion coefficient, it holds

$$D_N^{(\gamma')*} = D_0 \exp\left(-\frac{Q_D}{RT}\right) \quad (3.11)$$

with Q_D as the activation energy for the (tracer) diffusion of nitrogen in γ' , D_0 as a pre-exponential factor, R as the gas constant and T as the treatment temperature.

Therefore, a plot of the logarithm of the growth constant k divided by $2(\Delta \ln r_N)$ versus the reciprocal of the treatment temperature should result in a straight line. This is observed indeed (see Fig. 3.7). The value obtained from the slope of this straight line for the activation energy of $D_N^{(\gamma')*}$ is 117 kJ/mol. This value for Q_D is in the upper part of the range of values for Q_D found in the literature, ranging from 88 kJ/mol [71], 91 kJ/mol [63], (116 ± 30) kJ/mol [72] to 127 kJ/mol [66], as derived from the observed

kinetics for γ' -Fe₄N_{1-x}-layer growth on pure ferrite. It is concluded that the growth rate of the γ' -layer developing at the surface of cold rolled Fe-Mo alloy is controlled by nitrogen self-diffusion in the γ' -layer.

Table 3.3: Self-diffusion coefficients of N in γ' , $D_N^{(\gamma')*}$, pre-exponential factor D_0 and activation energy of diffusion of N in γ' , Q_D , as determined in the present work and as compared with literature data.

	$D_N^{(\gamma')*}$ [$10^{-16} \cdot \text{m}^2 \cdot \text{s}^{-1}$]			D_0 [$10^{-9} \cdot \text{m}^2 \cdot \text{s}^{-1}$]	Q_D [kJ/mol]
	753 K	793 K	823 K		
present work	0.67	1.42	3.17	7.9	117
Ref. [63]	2.14	4.48	7.42	0.47	91
Ref. [71]	2.02	4.12	6.72	0.27	88
Ref. [66]	3.2 ⁽¹⁾	-	7.9 ⁽²⁾	96	127
Ref. [72] ⁽³⁾	0.11	0.29	0.54	1.25	116

⁽¹⁾ determined at a temperature of 777 K

⁽²⁾ determined at a temperature of 827 K

⁽³⁾ extrapolated to the nitriding temperatures used in the present work

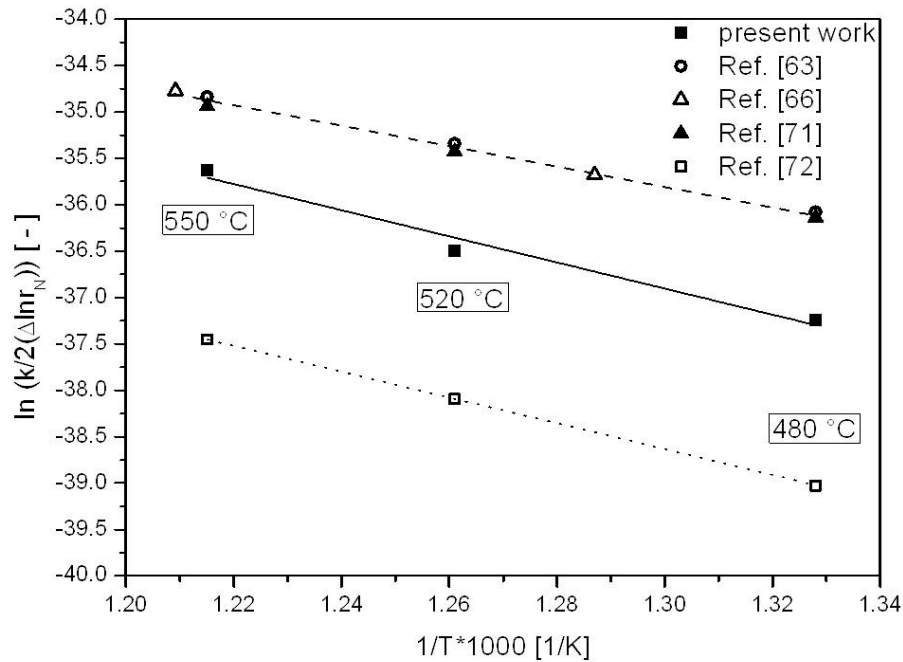


Fig. 3.7: Arrhenius plot of the natural logarithm of $k/2(\Delta \ln r_N)$ versus the reciprocal of the nitriding temperature. The activation energy for the self-diffusion of nitrogen in γ' -Fe₄N_{1-x} can be calculated from the slope of the straight line fitted to the experimental data in this plot (see text). Literature values, taken from Refs. [63] (unfilled circles), [66] (unfilled squares), [71] (solid triangles), and [72] (unfilled triangles) have been plotted as well.

3.4 Recrystallized specimens; results and discussion

3.4.1 X-ray diffraction – phase analysis

Diffractograms recorded from specimens nitrided at 753 K (480 °C) for different times are shown in Fig. 3.8.

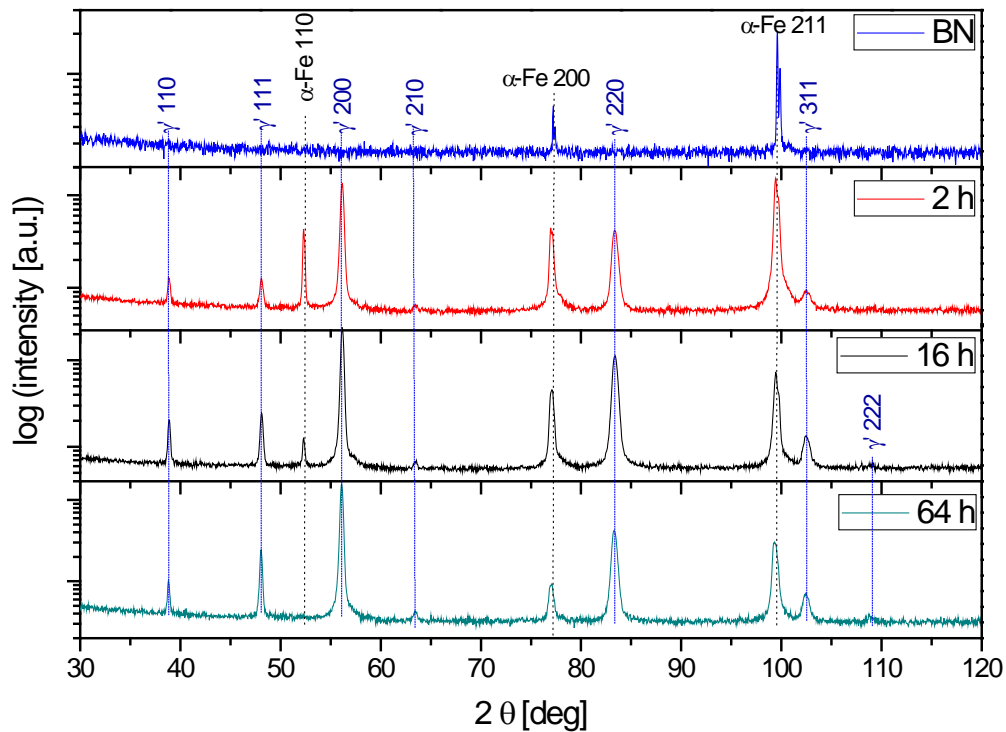
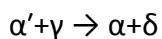


Fig. 3.8: X-ray diffraction patterns (Co- K_{α} radiation) of the recrystallized specimen before nitriding (BN) and after nitriding for different times at 753 K (480 °C) using a nitriding potential of $0.7 \text{ atm}^{-1/2}$. Dotted lines indicate reflection positions according to the ICDD database [51].

Even for the longest nitriding time investigated (64 h) at 753 K (480 °C), and apart of reflections of the ferrite substrate, only reflections from γ' nitride are detected. Thus, in contrast with the deformed specimens nitrided under similar conditions (cf. Figs. 3.1, 3.2 and their discussion), no substantial precipitation of Mo as nitride has occurred in the ferritic matrix of the recrystallized specimens at this stage of nitriding. Indeed, in contrast with what is observed for the deformed specimens, no asymmetric

broadening of the 200 ferrite reflection due to a possible precipitation of coherent molybdenum nitride (cf. discussion in section 3.3.1) occurs for the recrystallized specimens (compare Figs. 3.1 and 3.8).

At the elevated nitriding temperature of 793 K (520 °C), an additional reflection is observed that may be ascribed to cubic Mo₂N (see Figs. 3.9a and b after a nitriding time of 64 h) and upon prolonged nitriding a reflection arises that can be ascribed to hexagonal MoN (see Figs. 3.9a and b after a nitriding time of 64 h). At the still higher nitriding temperature of 823 K (550 °C), and also only after prolonged nitriding, an additional reflection is observed that can be ascribed to hexagonal MoN (see Fig. 3.10). Previous investigations [65] on bright nitriding (i.e. under conditions such that no iron nitrides can be formed at the surface) of Fe-1at.% Mo alloy showed that, upon nitriding such specimens at a temperature of 853 K (580 °C) for longer nitriding times, the nitride precipitation starts with the formation of submicroscopical Mo₂N-type precipitates followed by a discontinuous precipitation of the type [57, 58]:



where α' denotes the supersaturated ferrite matrix, γ represents the submicroscopical, likely largely coherent cubic Mo₂N-type precipitates and α and δ represent the ferrite and hexagonal MoN-type lamellae in the colonies produced by the discontinuous transformation starting from (mobile) grain boundaries in the ferrite matrix.

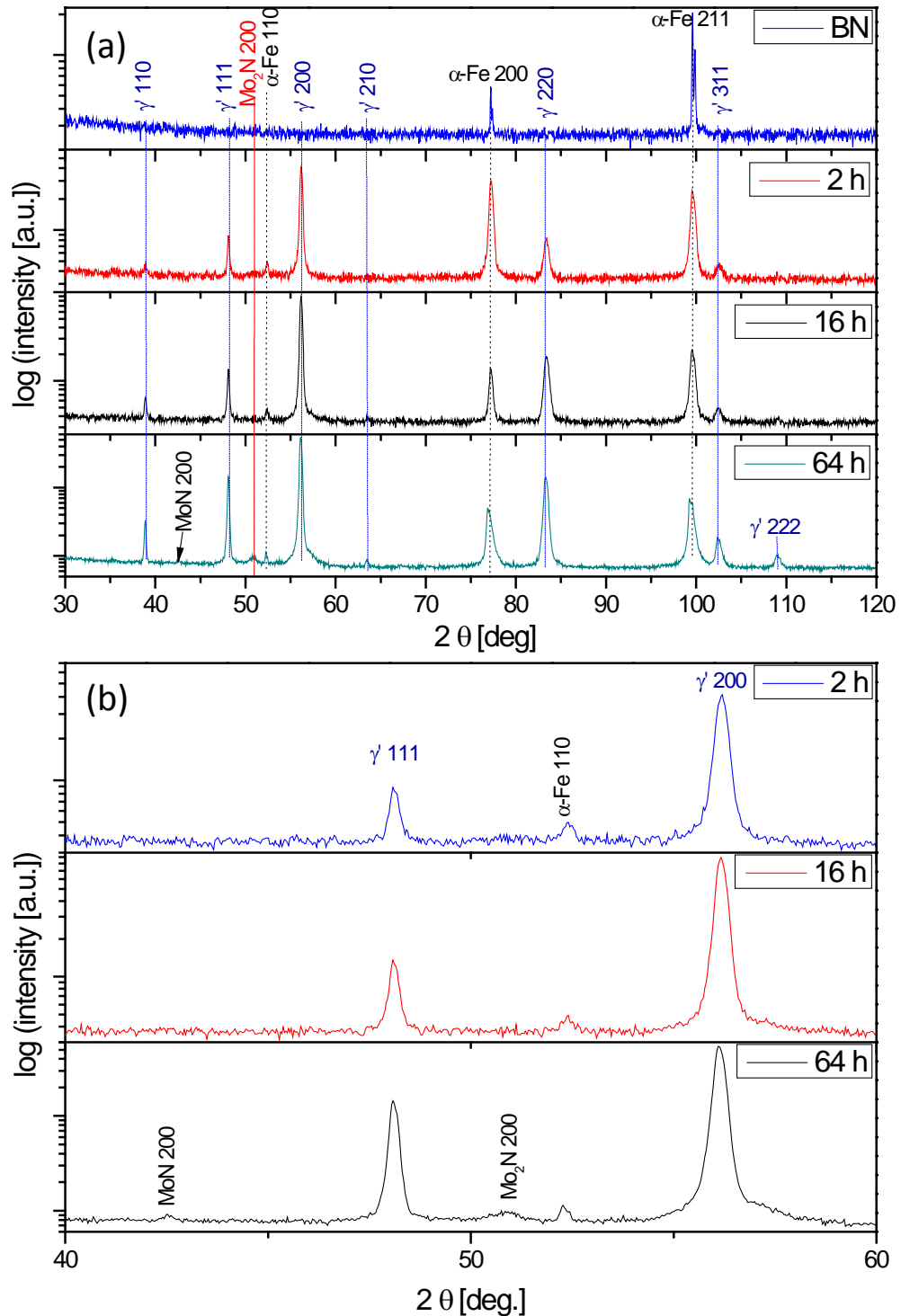


Fig. 3.9: X-ray diffraction patterns (Co- K_α radiation) of the recrystallized specimens (a) before nitriding (BN) and after nitriding for different times at 793 K (520 °C) using a nitriding potential of $0.7 \text{ atm}^{-1/2}$. Dotted lines indicate reflection positions according to the ICDD database [51]. The 2θ range $40^\circ \leq 2\theta \leq 60^\circ$ is shown magnified in (b) for 2 h, 16 h and 64 h of nitriding.

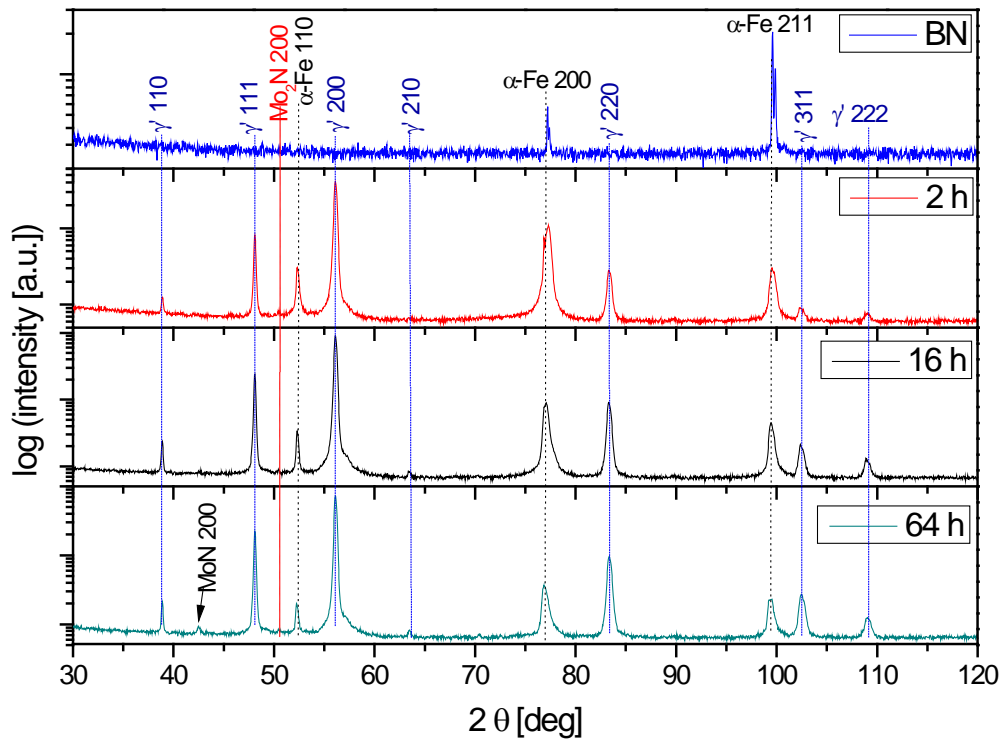


Fig. 3.10: X-ray diffraction patterns (Co- K_α radiation) of the recrystallized specimen before nitriding (BN) and after nitriding for different times at 823 K (550 °C) using a nitriding potential of 0.7 atm^{-1/2}. Dotted lines indicate reflection positions according to the ICDD database [51].

The glancing angle X-ray diffraction patterns of the recrystallized specimens nitrided at 793 K (520 °C) for 4 h and 6 h are shown in Fig. 3.11. Apart from reflections of γ' - $\text{Fe}_4\text{N}_{1-x}$, reflections indicating the presence of ε - Fe_{2-3}N and of the same unknown (precursor) nitride phase as observed for the cold rolled specimens (cf. Fig. 3.2) can be detected. The occurrence of these phases in the compound layer is explained in the same way as for the cold rolled specimens (cf. section 3.3.1): Mo cannot dissolve in the developing γ' and, as an intermediate stage, next to γ' ε and the precursory nitride develop, which incorporate the Mo originally dissolved in the ferrite matrix. For more pronounced stages of nitriding (see the glancing angle X-ray diffraction patterns shown in Fig. 3.12 pertaining to 4 h and 16 h of nitriding at the elevated temperature of 823 K (550 °C)), precipitation of Mo as an equilibrium, hexagonal MoN phase takes place and

the intermediate ε phase and unknown (precursory) nitride phase dissolve (cf. Figs. 3.12a and b).

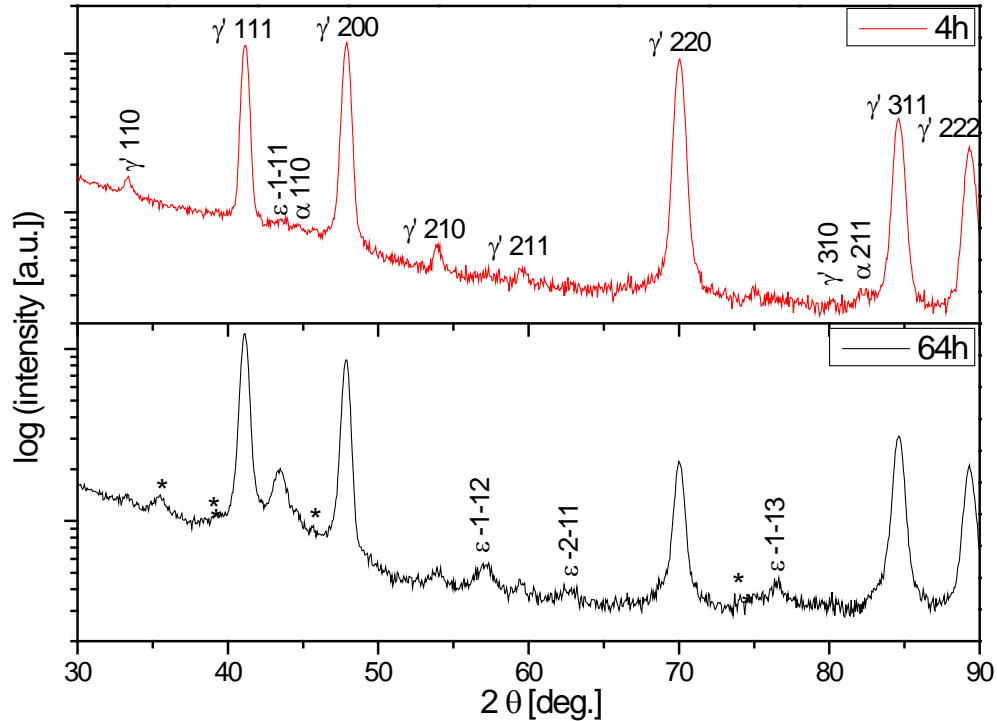


Fig. 3.11: Glancing angle X-ray diffraction patterns (Cu- K_{α} radiation) recorded from the surface of recrystallized specimens nitrided at 793 K (520 °C) for 4 h and 64 h. Apart from reflections originating from γ' - $\text{Fe}_4\text{N}_{1-x}$, reflections arising from ε - Fe_{2-3}N can be discerned. The star marks the positions of reflections of an unknown (precursory) nitride phase (cf. discussion in section 3.4.1).

Hence, at the higher temperature at a more advanced stage of nitriding ε nitride is promoted to form with Mo dissolved in it. Mo cannot stay dissolved in the ε phase due to enhanced kinetics for precipitation of molybdenum nitride at the elevated temperature. The glancing angle X-ray diffraction pattern recorded after a nitriding time of 16 h (Fig. 3.12) further suggests that, upon continued nitriding at this temperature, ε dissolves as it is thermodynamically not stable under the chosen nitriding conditions. This could be explained with the proceeding precipitation of Mo as nitride which makes ε less stable.

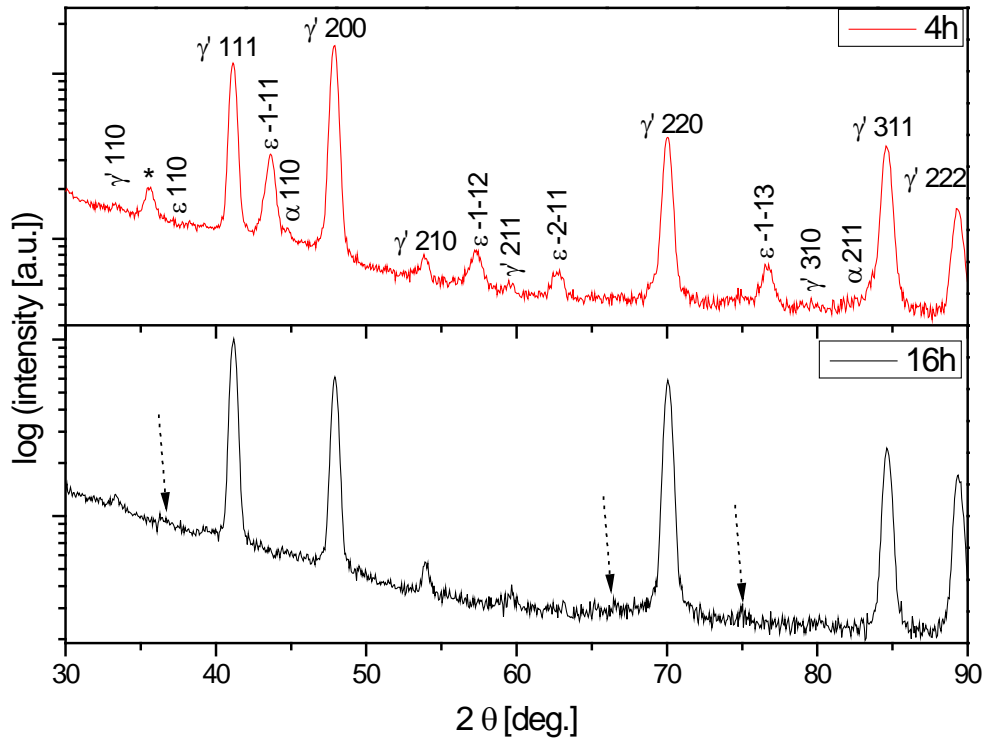


Fig. 3.12: Glancing angle X-ray diffraction pattern (Cu-K α radiation) from recrystallized specimens nitrided at 823 K (550 °C) for 4 h and 16 h. Apart from reflections originating from γ' -Fe₄N_{1-x}, reflections arising from MoN (black dotted arrows) and from ϵ -Fe₂₋₃N can be observed. The star marks the position of a reflection of the unknown (precursory) nitride phase; further, see discussion in section 3.4.1.

3.4.2 Occurrence of plate-like morphology of the γ' phase; the role of dissolved Mo

The influence of molybdenum (initially) dissolved in the ferrite matrix on the morphology of the γ' nitride layer at the initial stage of nitriding of recrystallized specimens is dramatic, as can be seen by comparing the microstructure adjacent to the surface of similarly nitrated recrystallized Fe-1at.% Mo alloy (Fig. 3.13a) with pure, recrystallized iron (Fig. 3.14; note the large difference in penetration by γ' of the ferrite matrix). In the case of nitriding of pure iron many nuclei of γ' nitride have developed at the surface, which, at the stage of nitriding considered, practically cover the whole surface, whereas in the case of Fe-1at.% Mo alloy, only a few γ' nuclei have formed, which have deeply penetrated the substrate as “plates”.

Upon nitriding at 793 K (520 °C) the density of γ' plates nucleated at the surface of the specimen is larger than at 753 K (480 °C) (see Fig. 3.13b). At longer nitriding times, a compact layer develops at the surface as a consequence of coalescence by lateral extension of the γ' plates at the surface, with γ' plates emanating from the compact part of the γ' phase and penetrating deeply the substrate (Fig. 3.13c).

The X-ray diffraction results presented in section 3.4.1 and the morphological observations reported above lead to the following interpretation. In case of nitriding Fe-1at.% Mo specimen under conditions allowing the formation of γ' , a competition between the (very slow [65]) formation of molybdenum nitride and of γ' occurs: The equilibrium solubility of Mo in γ' is likely (very) low, recognizing that the atomic radius of Mo is much larger than that of Fe [56]. Precipitation of γ' thus requires either a Mo partitioning in the ferrite matrix as by a preceding precipitation of Mo as molybdenum nitride to make possible formation of Mo free γ' , or γ' is forced to nucleate and grow with Mo dissolved in it. The precipitation of Mo_2N in the recrystallized, ferrite matrix is a very slow process, due to the large misfit of Mo_2N with the ferrite matrix [65]. These obstacles for the precipitation of both, γ' and Mo-nitride, lead to a large nitrogen supersaturation of the ferrite matrix over an extended depth range in the specimen. This nitrogen supersaturation can become that large that it eventually forces γ' to

Nitride surface-layer development upon nitriding of Fe-1 at.% Mo alloy

nucleate and grow, with Mo dissolved in it, across the extended depth range of high nitrogen supersaturation. This leads to the plate-like morphology of γ' deeply penetrating the substrate.

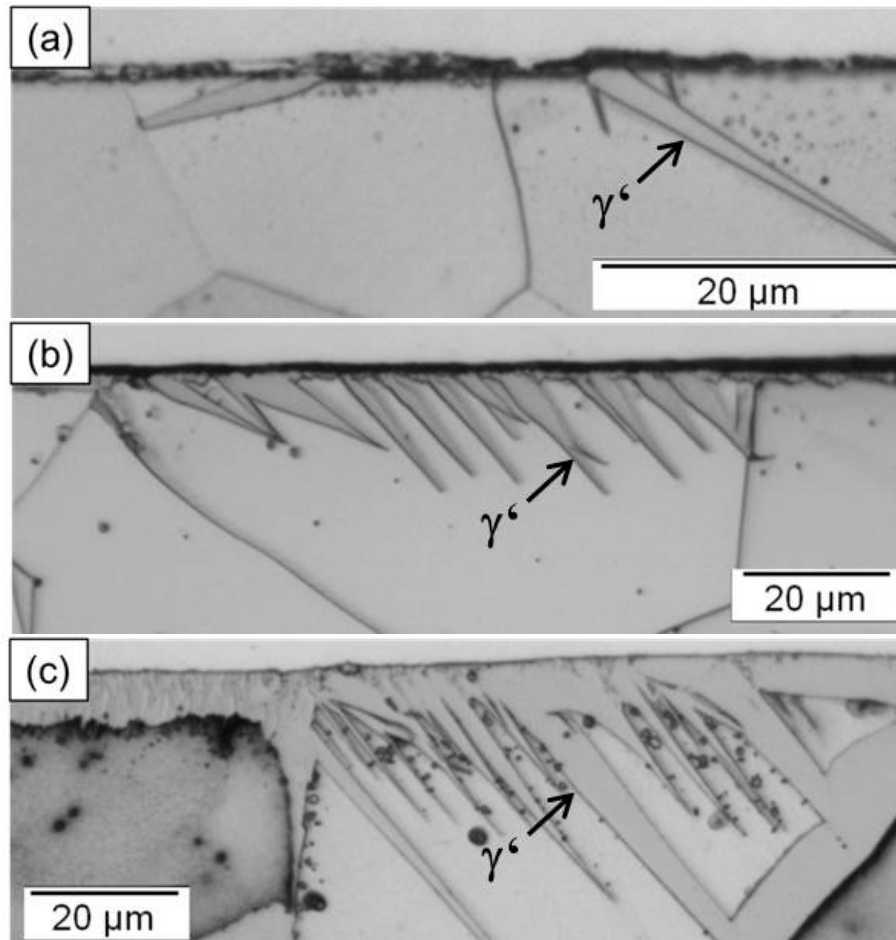


Fig. 3.13: LM-micrograph of the recrystallized Fe-1at.%Mo specimens nitrided for (a) 15 min at 753 K (480 °C), (b) 2 h at 793 K (520 °C) and (c) 64 h at 793 K (520 °C).

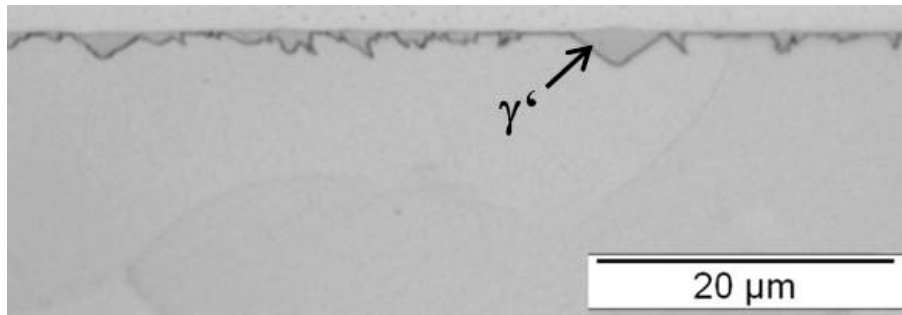


Fig. 3.14: LM-micrograph of a recrystallized pure Fe specimen nitrided for 15 min at 753 K (480 °C).

The delayed precipitation of Mo_2N or even the inability for Mo to precipitate as Mo_2N and the uptake of Mo as dissolved element in the delayedly precipitating γ' phase (as plates penetrating the ferrite substrate) can be demonstrated by the following EPMA and AES results.

The nitrogen concentration in γ' plates and in the adjacent ferrite matrix was determined by EPMA line scans for a specimen nitrided for 64 h at 753 K (480 °C) (see Fig. 3.15). Evidently, in-between the γ' plates the nitrogen concentration is below 0.3 at.% which corresponds with the solubility of nitrogen in pure ferrite at this temperature [73]. Hence, Mo has not precipitated as nitride within the recrystallized matrix in the nitrided zone (note the strikingly different result for the cold rolled specimens, where the nitrogen content of the matrix adjacent to the γ' phase is much larger and indicative of the presence of Mo-nitride precipitates; see Fig. 3.5 and its discussion in section 3.3.2).

The AES line scan crossing the γ' plate/ α -matrix interface for a specimen nitrided at 753 K (480 °C) for 16 h demonstrates that the Mo/Fe atomic ratio is the same in the matrix and γ' plate. Also no separate molybdenum-nitride phase occurs in the γ' phase at the surface (as demonstrated by the glancing angle X-ray diffraction analysis; see Fig. 3.11). Hence, it can be concluded that γ' -plate development occurs under incorporation of Mo in the γ' phase, in agreement with the glancing angle X-ray diffractogram shown in Fig. 3.11 and the above discussion.

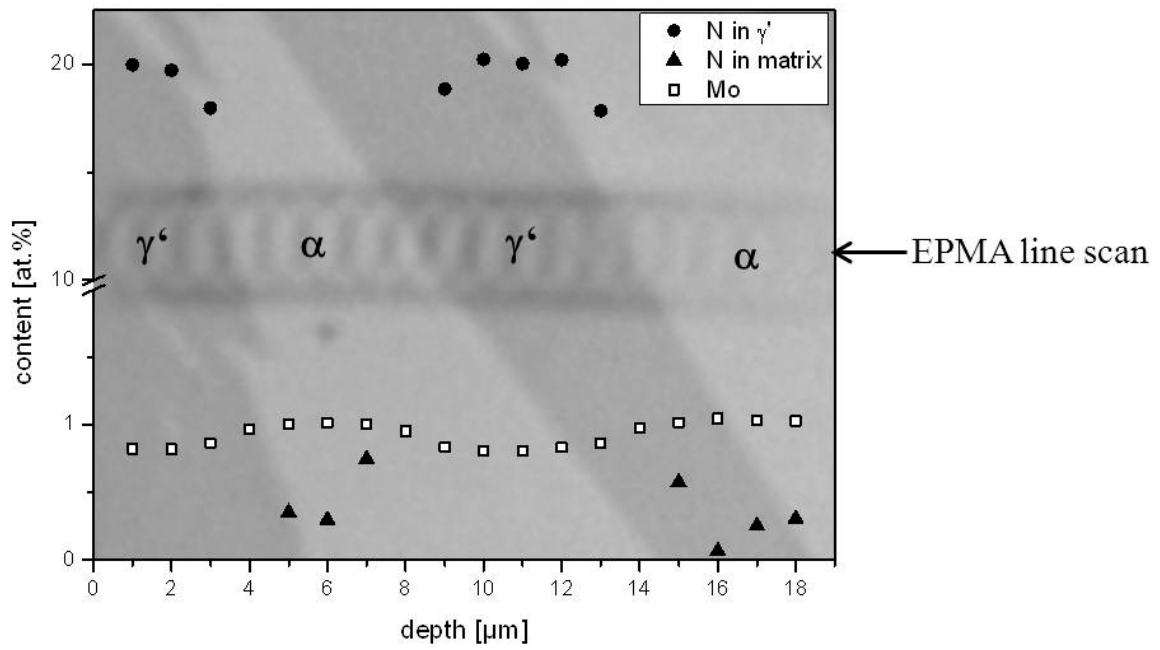


Fig. 3.15: Nitrogen concentration-depth profile (EPMA line scan) of the specimen nitrided at 723 K (480 °C) for 64 h superimposed on the corresponding light optical micrograph. The position of the line scan is indicated by the contamination spots.

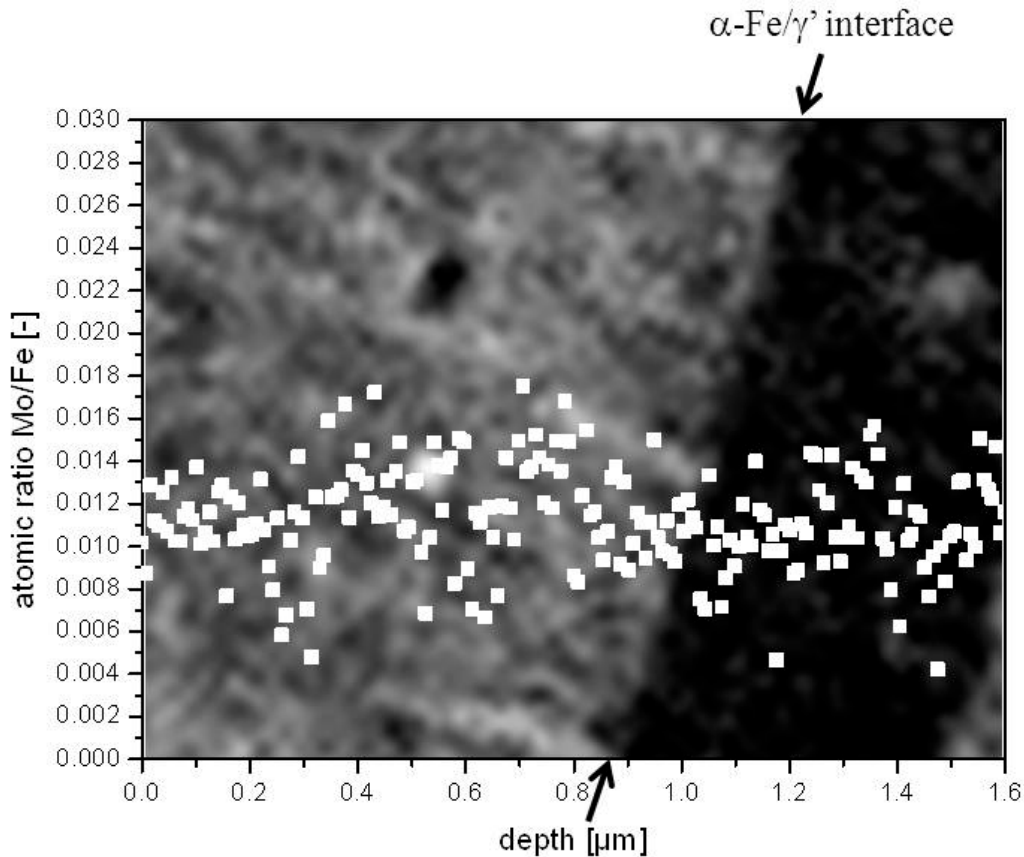


Fig. 3.16: The Mo/Fe atomic ratio across a ferrite-matrix/ γ' -plate interface as measured by an AES line scan on a cross section of the specimen nitrified at 753 K (480 °C) for 16 h. The elemental atomic ratio is plotted starting from the ferrite-matrix into the γ' plate onto the corresponding secondary electron image (light grey: ferritic matrix; dark grey: γ'). The atomic ratio of Mo/Fe is constant within experimental accuracy.

In order to confirm the above described effect of dissolved molybdenum on the morphology of the developing γ' phase, a specimen of Fe-1at.% Mo alloy was first nitrified at a nitrifying potential and temperature such that no γ' could form and all Mo could precipitate as nitride (734 h at a temperature of 853 K (580 °C) using a nitrifying potential of $0.104 \text{ atm}^{-1/2}$ [65]). Complete precipitation of MoN in this thin foil specimen was proven experimentally by weight gain measurements (no further nitrogen uptake could be observed). Next, this specimen was nitrified at 753 K (480 °C) for 72 h using a nitrifying potential of $0.7 \text{ atm}^{-1/2}$, implying that γ' phase can develop. The corresponding

light optical micrograph shown in Fig. 3.17 reveals that a compact γ' -Fe₄N layer had developed at the surface, i.e. the peculiar plate-like morphology did not occur (within the grains, the discontinuously transformed microstructure, consisting of hexagonal MoN and ferrite lamellae, as described in section 3.4.1, can be seen). Hence, only in the presence of Mo dissolved in the ferrite matrix does the platelet-like morphology of γ' occur.

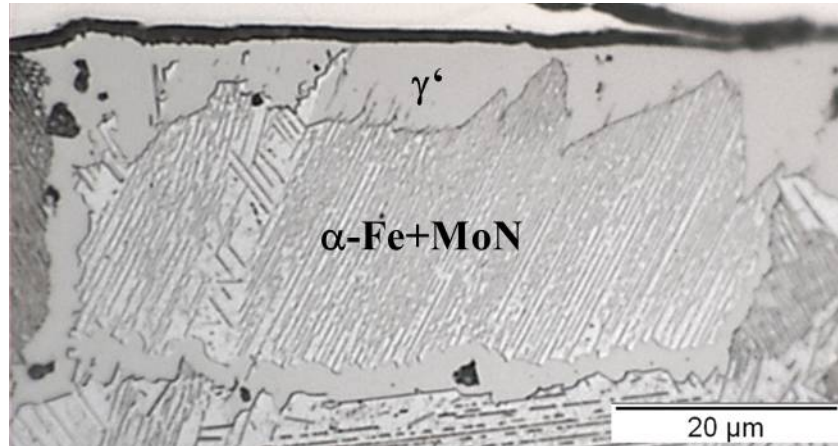


Fig. 3.17: LM-micrograph of the recrystallized specimen nitrided for 72 h at 753 K (480 °C) with a nitriding potential of 0.7 atm^{-1/2} after pre-saturation at 853 K (580 °C) for 734 h with a nitriding potential of 0.1 atm^{-1/2}.

The high growth rate of these plates, once nucleated, as compared to the growth rate of the compact γ' layer (cf. Figs. 3.13a and 3.14) is presumably not only a result of the high nitrogen supersaturation over an extended depth range, but can also be ascribed to “short circuit” nitrogen diffusion into the specimen through uncovered (i.e. bare, γ' -free) ferrite parts of the surface: nitrogen diffusion through ferrite (activation energy 78 kJ/mol [74]) is much faster than through γ' (see section 3.3.3).

The unusual plate-like morphology of γ' nitride does not occur for nitrided Fe-Cr [75], Fe-V [76] and Fe-Ti [77, 78] alloys. In these systems the much faster precipitation of the alloying element nitrides, CrN, VN and TiN, allows precipitation of γ' only after all alloying element has precipitated as alloying element nitride, i.e. in these cases no such high nitrogen supersaturation over an extended depth range of the ferrite matrix

occurs. Consequently and reversely, such unusual morphology of γ' precipitation has also been observed upon nitriding of Fe-Al [62] and Fe-Si alloys [79].

At a relatively high nitriding temperature (i.e. 823 K (550 °C)), the morphology of the developing γ' nitride, in case of recrystallized Fe-Mo specimens, is similar to that observed upon nitriding cold rolled Fe-Mo specimens and nitrided recrystallized pure iron specimens: γ' forms as a compact layer at the surface (see Figs 3.18a and b). This can be interpreted as that at this relatively high nitriding temperature, the Mo-nitride precipitation rate is that high that γ' growth occurs into a ferrite matrix which, more or less, no longer contains dissolved Mo and where no high nitrogen supersaturation prevails.

Additionally, γ' -growth along grain boundaries can be observed (Fig. 3.18b). This can be understood as a consequence of the favoured nucleation of Mo-nitride precipitates at the grain boundaries [80]. Thereby the ferrite matrix adjacent to the grain boundaries is depleted of dissolved Mo and thus the obstacle for γ' growth into this ferrite is removed.

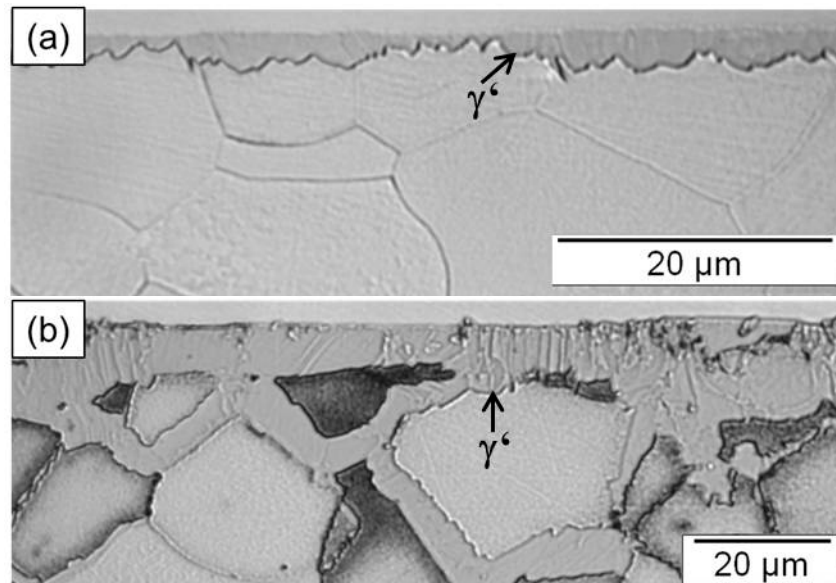


Fig. 3.18: LM-micrographs of the recrystallized specimens nitrided for (a) 2 h at 823 K (550 °C) and (b) 64 h at 823 K (550 °C).

The microhardness-depth profiles in the nitrided zone of the ferrite matrix indicate (also) that Mo-nitrides are virtually absent at a comparatively low nitriding temperature such as 753 K (480 °C): for the extended time range investigated the hardness increase remains on a level representative of dissolution (only) of nitrogen in the ferritic matrix (see Fig. 3.19a) [81]. At a higher nitriding temperature such as 823 K (550 °C) Mo nitride develops in the ferrite matrix leading to a distinct increase of hardness (see Fig. 3.19b and compare with Fig. 3.19a). The more or less homogeneous increase in hardness level as function of time across the depth range investigated suggests that Mo effectively acts as a weak nitride former, i.e. precipitation takes effectively place at each depth at the same time with the same rate.

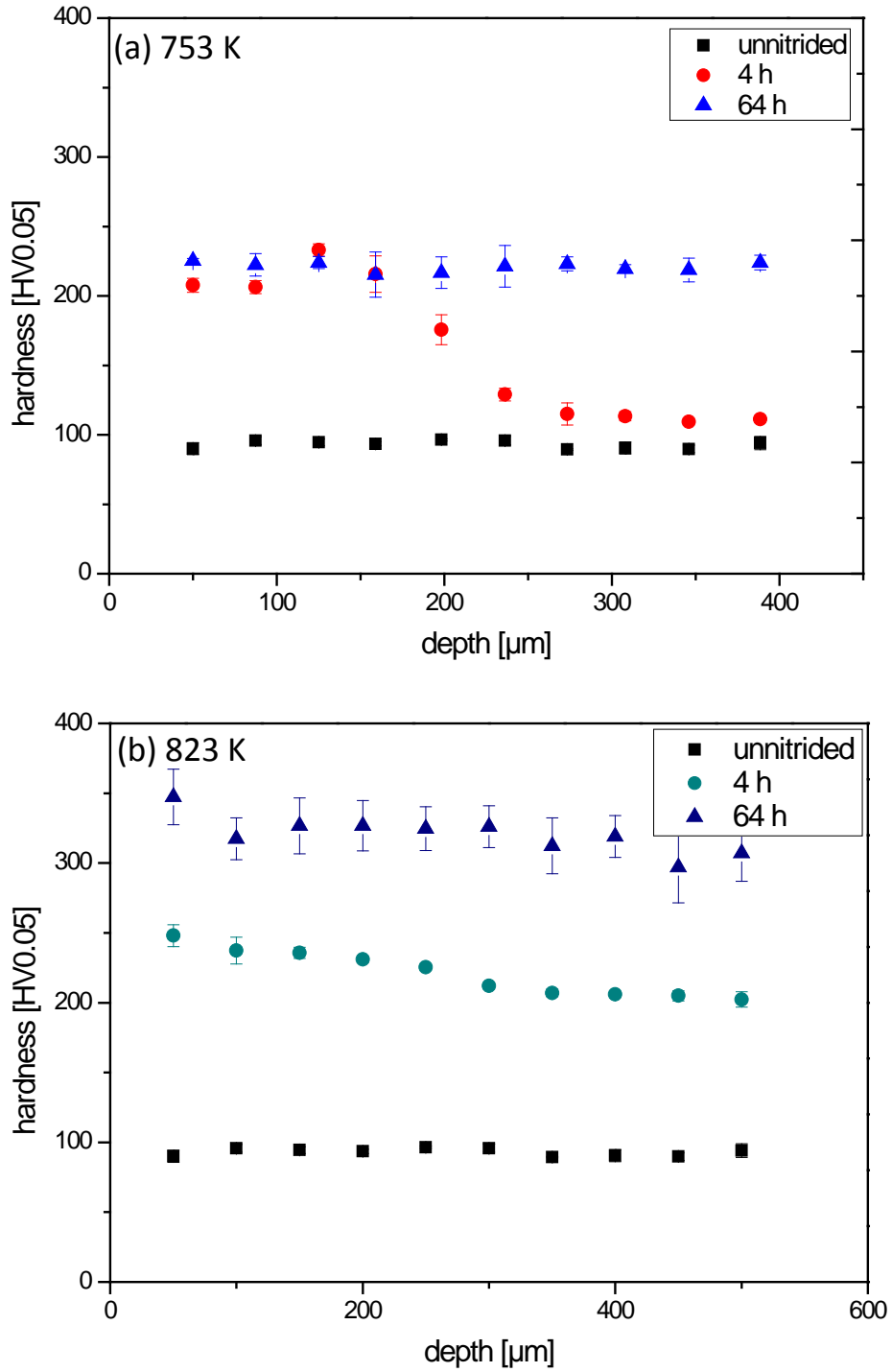
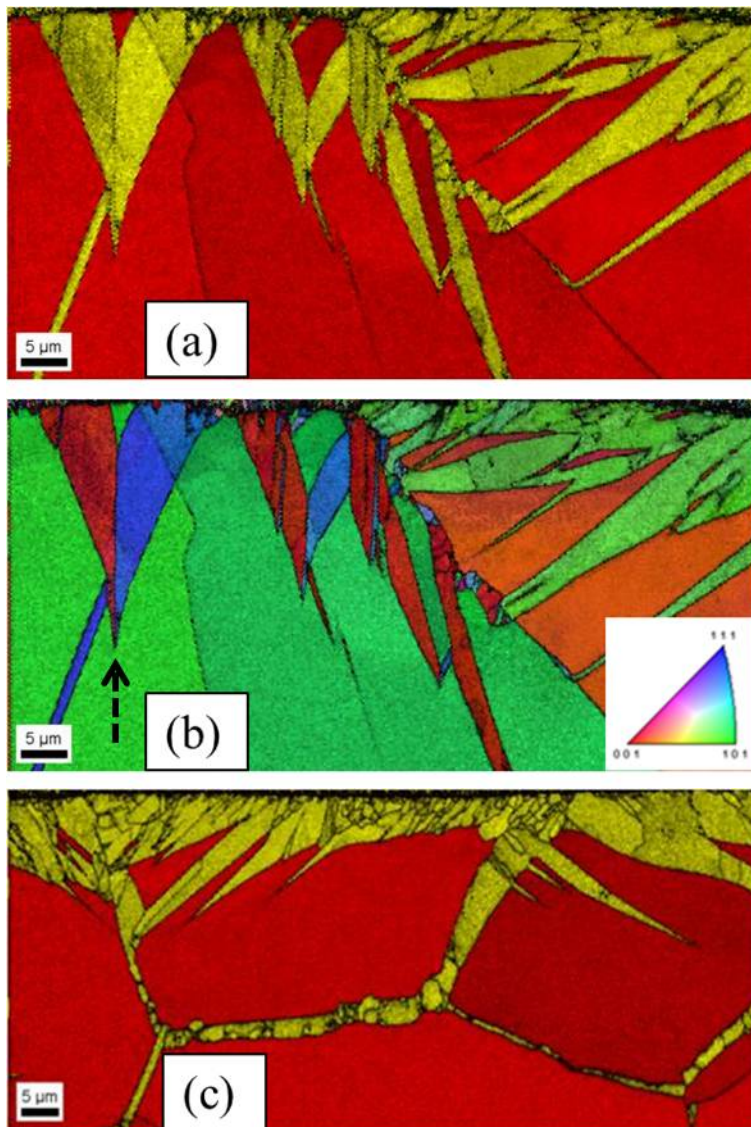


Fig. 3.19: Hardness-depth profiles of recrystallized specimens before nitriding and after nitriding for 4 h and 64 h (a) at 753 K (480 °C) and (b) at 823 K (550 °C).

3.4.3 Orientation relationship γ' nitride/ferrite

The orientation relationship of the γ' plates and the ferritic matrix was determined by EBSD analysis of the recrystallized specimens nitrided for 64 h at different temperatures (753 K (480 °C), 793 K (520 °C) and 823 K (550 °C)) (see Figs. 3.20a-f for phase and orientation maps). The γ' plates growing from the surface towards the centre of the specimen upon nitriding at 753 K (480 °C) consist of γ' nitride (see the phase map in Fig. 3.20a) and are, upon growing together in a single ferrite-matrix grain, separated by $\Sigma 3$ twin boundaries (see indication in the orientation map, Fig. 3.20b).



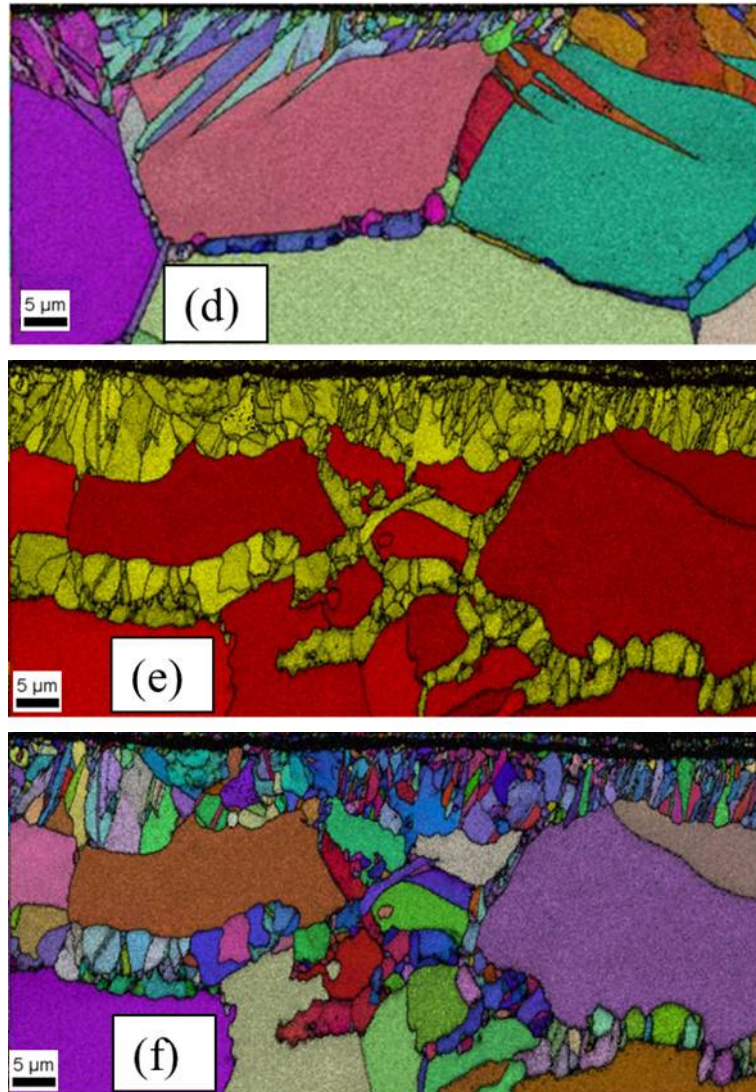


Fig. 3.20: EBSD images obtained after a nitriding time of 64 h (a) phase map obtained at 753 K (480 °C), (b) orientation map obtained at 753 K (480 °C), $\Sigma 3$ twin boundary is indicated by a dashed arrow, (c) phase map obtained at 793 K (520 °C), (d) orientation map obtained at 793 K (520 °C), (e) phase map obtained at 823 K (550 °C) and (f) orientation map obtained at 823 K (550 °C). The Fe-substrate (bcc crystal structure) is indicated by red colour in the phase map, whereas the γ' iron nitride (fcc crystal structure) is colour-coded in yellow. In the orientation map the normal direction of the crystals (for the cross section shown) is colour-coded according to the inverse pole figure shown in the inset in (b).

To calculate the orientation relationship of the γ' precipitates and the ferritic matrix three Euler angles for each grain of each phase were extracted from the EBSD data for γ' grains which had grown from the surface into the ferrite matrix. With these angles (and the transformation matrix M given in [82]), all 9 combinations of $\langle 100 \rangle$ directions of γ' and $\langle 100 \rangle$ directions of α -Fe were calculated (see Figs. 3.21a-c). As follows from Fig. 3.20a these calculated angles for the sample nitrided at 753 K (480 °C) for 64 h accumulate around $9^\circ \pm 3^\circ$, $45^\circ \pm 4^\circ$, $90^\circ \pm 10^\circ$ and $135^\circ \pm 5^\circ$. Similarly for the results obtained upon nitriding at 793 K (520 °C) for 64 h (see Fig. 3.20b). Hence, the γ' precipitates develop according to a Nishiyama [83]–Wassermann [84] (NW) orientation relationship with the ferrite matrix: $(110)_{\alpha\text{-Fe}} // (1\bar{1}1)_{\gamma'}$ and $[001]_{\alpha\text{-Fe}} // [10\bar{1}]_{\gamma'}$. Such an OR has also been reported in Ref. [85] for a furnace cooled hypoeutectoid Fe-N alloy. In Ref. [86], however, a Pitsch OR (inverse NW OR) was observed possibly due to the precipitation carried out at much lower treatment temperatures ($T < 350^\circ\text{C}$) than in the present work.

As shown in Fig. 3.20c, nitriding at higher temperatures (823 K (550 °C)) results in a compact γ' nitride layer which exhibits no preferred OR with the ferrite substrate. This parallels the observations on nitriding cold deformed specimens (see section 3.3.2). Apparently, the relatively large driving force for γ' nucleation, at the surface, in those cases allows development of γ' grains with less favourable interfaces with the ferrite matrix.

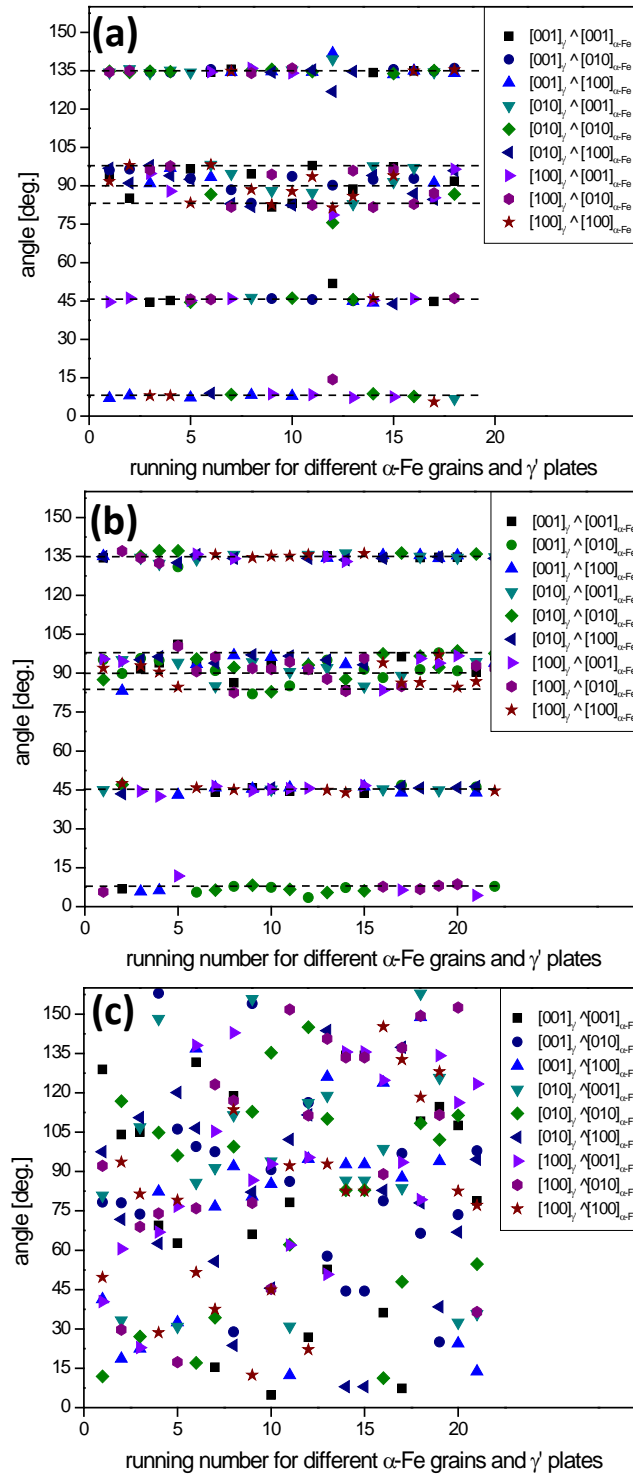


Fig. 3.21: Calculated angles between the different $\langle 100 \rangle$ type directions in ferrite and those in γ' nitride for the recrystallized specimens nitrided for 64 h (a) 753 K (480 °C), (b) at 793 K (520 °C) and (c) at 823 K (550 °C).

3.5 Conclusions

The defect density of iron-based Fe-Me alloy, with Me as an (effectively) weak nitride former (e.g. Me = Mo), has a dramatic effect on the constitution and morphology of the iron-nitride based compound layer developing upon nitriding:

- Upon nitriding *cold rolled* Fe-1at.% Mo alloy *immediate* precipitation of Mo_2N (dislocation facilitated nucleation) occurs, leading to a low nitrogen supersaturation of the ferrite matrix. γ' nucleates (only) at the surface resulting in the development of a compact layer of γ' , incorporating (by overrunning the formed) Mo_2N particles. The γ' layer growth can be described by a modified parabolic growth law, accounting for the initial delay in the nucleation of γ' . Growth of the nitride layer is rate controlled by diffusion of nitrogen through the layer.
- Upon nitriding *recrystallized* Fe-1at.% Mo alloy (strongly) *delayed* precipitation of Mo_2N occurs (if at all): no Mo_2N can be found in the matrix even after 64 h of nitriding at 753 K (480 °C). This is a consequence of the high volumetric misfit between the ferrite matrix and the Mo_2N nitride. Because the solubility of Mo in γ' is low, γ' nitride cannot precipitate easily. These obstacles for Mo-nitride and γ' -nitride precipitation lead to a high nitrogen supersaturation of the ferrite matrix over an extended depth range. Eventually, the chosen route for elimination of this high nitrogen supersaturation is precipitation of γ' at the cost of dissolution of Mo in γ' (para-equilibrium conditions). Plates of γ' nitride, once nucleated, grow rapidly across the extended depth range of high nitrogen supersaturation. The relatively high growth rate of these plates is at least partly due to short-circuit diffusion of nitrogen through ferrite grains adjacent to the surface (no compact γ' layer occurs). The γ' plates exhibit a Nishiyama-Wassermann orientation relationship with the ferrite matrix.
- The equilibrium solubility of Mo in γ' nitride is low. This leads to the emergence of ϵ phase and a hitherto unknown (precursory) Mo-nitride phase, next to γ'

phase in the compound layer, upon nitriding the recrystallized Fe-Mo specimens, and also the cold rolled specimens in a beginning stage of nitriding. Upon continued nitriding the ϵ phase and the unknown (precursory) Mo-nitride phase in the surface adjacent part of the compound layer dissolve and equilibrium Mo-nitride phases emerge.

CHAPTER 4

Microstructural and surface residual stress development during low-temperature gaseous nitriding of Fe-3.07at.%Mo alloy

H. Selg, E. Bischoff, R. Schacherl, J. Schwarzer, E.J. Mittemeijer

Abstract

Fe-3.07at.% Mo alloy specimens were nitrided at 480 °C in a NH₃/H₂ gas mixture applying a nitriding potential of 0.25 atm^{-1/2}. Selected area electron diffraction patterns (SADPs) of the nitrided zone showed continuous streaking in <100>_α directions, which indicates the presence of fine, nano-sized precipitate platelets, with a coherent interface parallel to the {100} planes of the ferrite (α) matrix. The X-ray diffractograms, recorded from the specimen surface, showed an asymmetric broadening of the ferrite-matrix reflections which was especially pronounced for the (200) reflections, which hints at a tetragonal distortion of the (microstressed) ferrite matrix surrounding the precipitates. These misfitting, nano-sized precipitates cause a relatively high hardness as well as a compressive residual macrostress parallel to the surface in the nitrided zone adjacent to the surface: 900 HV0.05 and 1100 MPa, respectively.

4.1 Introduction

Nitriding is a thermochemical surface treatment which is of great industrial importance to improve the surface mechanical and chemical properties of ferritic steel components. As nitriding medium, a gas atmosphere composed of ammonia and hydrogen gas is often used. Gaseous nitriding allows an accurate control of the chemical potential of nitrogen in the nitriding atmosphere. The nitriding potential $r_N = \frac{P_{NH_3}}{P_{H_2}^{3/2}}$ is proportional to

the activity of nitrogen in the atmosphere [8]. If it is assumed that the chemical potential of nitrogen in the gas atmosphere is equal to the chemical potential of nitrogen absorbed at the surface (so-called local equilibrium), the nitrogen uptake can be adjusted very precisely by control of the composition of the gas atmosphere at constant temperature and pressure [9]. Depending on the value of the nitriding potential, only a diffusion zone or a diffusion zone and a compound layer at the sample surface can be formed. In the case of the presence of nitride forming elements inner nitrides will be formed in the diffusion zone.

Mo as substitutionally dissolved element could precipitate as molybdenum nitride in the nitrified surface region, because of its affinity for nitrogen. Mo is mostly not added deliberately to promote such precipitation (in contrast with nitride forming elements such as Cr and Al), but it is often present in nitriding steels in order to improve the tempering brittleness, the strength and the weldability [46]. Although a distinct driving force for the precipitation of molybdenum nitride exists, relatively little is known about this precipitation process.

Upon nitriding of Fe-1.7at.% Mo and Fe-3at.% Mo alloys in the temperature range of 400 °C to 600 °C a homogenous nucleation of coherent metastable substitutional-interstitial “zones on {100} matrix ferrite planes” were observed [21]. It was also reported that the size, composition and structure of the developed “zones” depend on the amount of Mo, the nitriding temperature as well as the nitriding potential. Coarsening of these zones led to Mo₂N-precipitates of fcc-type structure having a Bain-orientation relationship [87] with the ferrite matrix [88].

The purpose of the present project is to investigate the nature of the nitride-precipitation process and the corresponding mechanical properties (such as hardness, residual stress) of nitrided layers developing during gaseous nitriding of Fe-3.07at.% Mo alloy.

4.2 Experimental

4.2.1 Specimen preparation

Pure iron (99.98 wt.%) and pure molybdenum (99.99 wt.%) were weighed and pre-alloyed in an arc furnace. The pre-alloyed lumps were melted in an Al₂O₃ crucible by means of an inductive furnace under a protective argon gas atmosphere (99.999 vol.%). The melt was cast in a copper mould to obtain a cylindrical rod (diameter: 10 mm, length: 100 mm). The chemical composition and the amounts of impurities were determined using chemical analysis (inductively coupled plasma - optical emission spectroscopy, combustion method and carrier gas hot extraction). The results are shown in Table 4.1.

Table 4.1: Amounts of alloying elements and impurities of the used alloy (balance: Fe)

Element	Mo	O	N	C	S
content [wt.%]	5.16±0.05	0.015±0.001	0.0013±0.0003	0.0033±0.0008	0.003±0.001
content [at.%]	3.07±0.03	0.054±0.004	0.0053±0.001	0.0157±0.004	0.054±0.002

After casting the rod was cut into 3 pieces before cold rolling to sheets of a thickness of 1 mm. Out of these sheets, rectangular specimens were cut (dimensions: about 15 x 10 x 1 mm³). Subsequently, the specimens were ground, cleaned in an ultrasonic bath using ethanol and then encapsulated in a quartz tube which was filled with argon gas (purity: 99.999 vol.%), followed by recrystallization in a muffle furnace at 800 °C for 90 min.

4.2.2 Nitriding

Before nitriding, the recrystallized specimen surfaces were polished mechanically (final step: 1 μm diamond suspension) and cleaned with ethanol in an ultrasonic bath. The nitriding experiments were performed at a temperature of (480 ± 1) °C in a vertical, multizone quartz-tube furnace (diameter: 28 mm) with a NH_3/H_2 gas mixture flux of 500 ml/min (purity NH_3 : > 99.998 vol.%, purity H_2 : 99.999 vol.%). The gas fluxes were adjusted by mass flow controllers and corresponded to a nitriding potential of $r_N = 0.25 \text{ atm}^{-1/2}$. The nitriding potential was chosen such that no iron nitrides develop at the surface [9]. The nitriding process was terminated by quenching the specimens in water at room temperature.

4.2.3 Specimen characterization

4.2.3.1 X-ray diffractometry

Phase analysis by means of X-ray diffraction (XRD) was performed of all specimens before and after nitriding by using a PANalytical X'Pert Multi-Purpose Diffractometer (MPD) with $\text{Co-K}\alpha$ radiation. This instrument uses Bragg-Brentano geometry and is equipped with a graphite monochromator in the diffracted beam. To improve the crystallite statistics, the specimens were rotated around their surface normal during the measurements. The diffraction-angle range ($30^\circ < 2\theta < 120^\circ$) was scanned in steps of 0.06° with a counting time of 30 s per step. For the identification of the phases based on the positions of the diffraction peaks, data of the ICDD database were used[51].

To determine the residual stress, XRD stress measurements were performed using the crystallite group method, as described by [89], recognizing the (100)-fibre texture present after recrystallization, instead of applying the conventional $\sin^2\psi$ -method. Stress values were obtained for the case of a macroscopically elastically isotropic specimen with a plane, rotationally symmetric biaxial state of stress (see also [90]).

The measurements were performed using a PANalytical X'Pert Materials-Research Diffractometer (MRD), equipped with an Eulerian cradle and a graphite monochromator in the diffracted beam, applying a quasi-parallel beam geometry and Co-K α -radiation. The different diffraction-angle ranges for the different reflections (α -Fe (110) reflection: $45^\circ < 2\theta < 60^\circ$; α -Fe (200) reflection: $65^\circ < 2\theta < 90^\circ$; α -Fe (211) reflection: $90^\circ < 2\theta < 110^\circ$; α -Fe (220) reflection: $118^\circ < 2\theta < 132^\circ$) were scanned in steps of 0.08° using a counting time of 10 s per step.

4.2.3.2 Electron probe microanalysis (EPMA)

For the determination of nitrogen concentration-depth profiles EPMA was performed on polished cross sections of the specimens using a Cameca SX100 microprobe (acceleration voltage = 10 kV, current = 100 nA, spot size of about 1 μm). For details, see Ref. [3].

4.2.3.3 Light microscopy (LM)

Cross sections of the nitrided specimen, embedded in Struers PolyFast, were ground, polished (final polishing step: 1 μm diamond paste) and finally etched with 2 % Nital (2 vol.% HNO₃ in ethanol) at room temperature for about 30 s. LM micrographs were taken from these cross sections using a Zeiss Axiophot microscope equipped with a digital camera (Olympus ColorView IIIu).

4.2.3.4 Microhardness measurement

Microhardness measurements were made on cross sections of the nitrided specimens (see section 4.2.3.3) using a Vickers microhardness tester (Leica VMHT Mot) applying a load of 490 mN and a dwell time of 10 s.

4.2.3.5 Transmission electron microscopy (TEM)

A TEM specimen was prepared from the Fe-3.07at.% Mo alloy specimen nitrided for 20 h. Details of the preparation technique have been given in Ref. [5]. TEM analysis was performed using a Philips CM 200 transmission electron microscope operating at 200 kV. Bright field (BF) images, dark field (DF) images and selected area electron diffraction patterns (SADPs) were recorded by a CCD camera attached to the TEM apparatus.

4.3 Results and discussion

4.3.1 Microstructure

X-ray diffractograms recorded from the specimen surfaces before and after nitriding for different times are shown in Fig. 4.1. In the unnitrided condition, apart from reflections originating from the ferrite matrix, additional reflections can be expected because the maximum solubility of Mo in Fe is somewhere between 1 and 1.5 at.% at a temperature of 527 °C [91]: nitriding was performed in a two-phase region of the Fe-Mo system. Additional reflections are observed indeed, which can be indexed as reflections originating from a $\text{Fe}_3\text{Mo}_3\text{N}$ Laves phase. This phase is stabilized by interstitial elements such as O, C, and N. The reflections of the Laves-phase $\text{Fe}_3\text{Mo}_3\text{N}$ decrease and finally disappear (see diffractogram taken from the 100 h nitrided sample in Fig. 4.1) completely, since all molybdenum in the specimen is used for the formation of molybdenum-nitride precipitates. However, no reflections originating from molybdenum nitrides can be observed (see what follows).

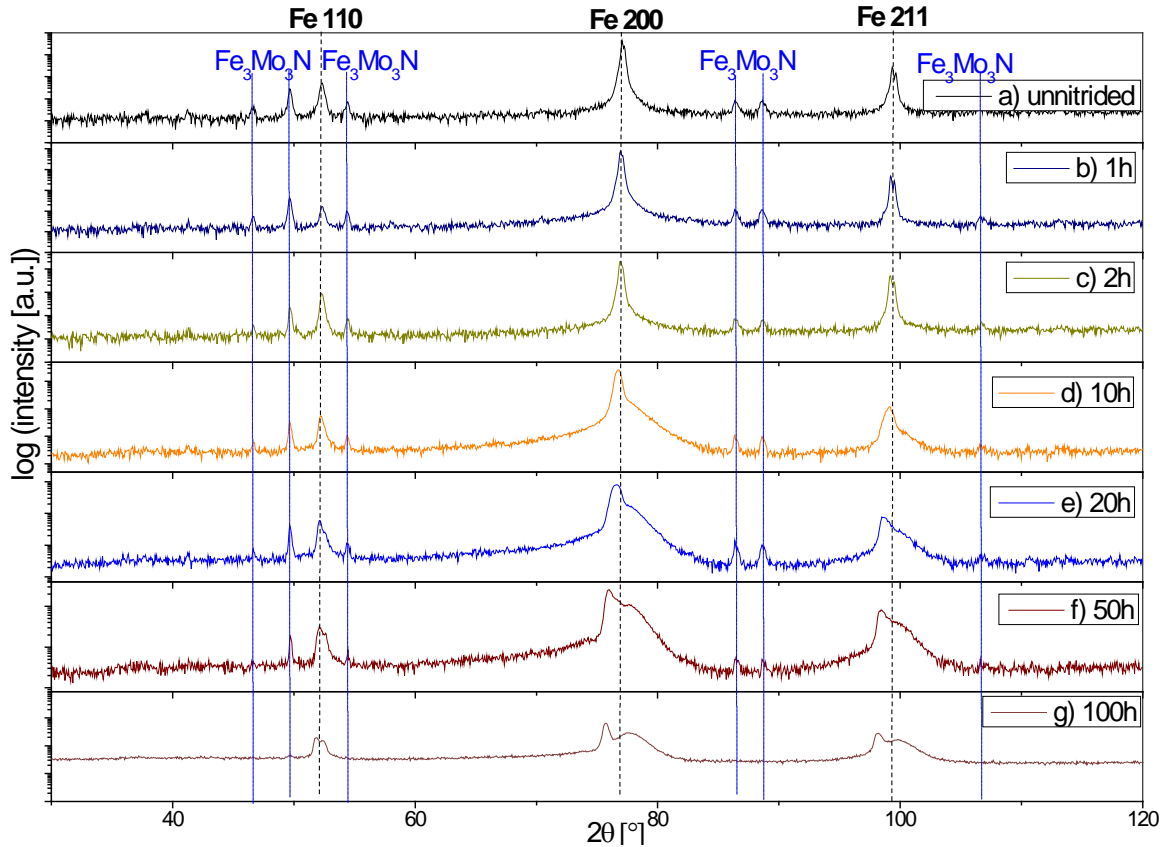


Fig. 4.1: X-ray diffractograms taken from the specimen surface before nitriding (a), and after nitriding for 1 h (b), 2 h (c), 10 h (d), 20 h (e), 50 h (f) and 100 h (g).

With increasing nitriding time an asymmetric peak broadening of the ferrite-matrix reflections occurs, in particular after 2 h of nitriding, i.e. after significant precipitation has begun (cf. discussion in section 4.3.2). This can be ascribed to the development of microstrain due to the formation of largely coherent nitride precipitates in the matrix, which also diffract coherently with the matrix. This causes the intensity “hump” at the high-angle side of the matrix reflections, eventually leading to even peak-splitting after a nitriding time of 100 h. This intensity hump represents the tetragonal 200/002 doublet reflection due to the tetragonally distorted ferrite matrix surrounding the precipitates, as discussed for VN precipitates in a ferrite matrix [45].

The SADP and the corresponding bright field image of a TEM specimen from a region near the surface are shown in Fig. 4.2. The platelet-like, very small precipitates,

having a length of 10-15 nm and a thickness of < 1 nm, are oriented with their faces along $\{100\}_{\alpha\text{-Fe}}$ planes. Due to the very fine platelet-like nature of the coherent precipitates, diffraction streaks along $\langle 100 \rangle_{\alpha\text{-Fe}}$ directions are present in the SADP. The precipitate platelets could be conceived as fcc-type Mo_2N nitride exhibiting a Bain-type orientation relationship with the matrix, as observed by [88] only after coarsening. Then, this nitride would experience a misfit parallel to the habit plane of only a few percent, whereas the misfit perpendicular to the habit plane would be very large. An alternative crystal structure is to conceive the platelets as fcc-type MoN which could exist according to a theoretical calculation [92]. Also in this case a Bain-type orientation relationship is anticipated, albeit with a larger misfit parallel to the habit plane than for Mo_2N . Due to the occurrence of only streaking, the determination of the crystal structure of the formed precipitates is not possible at this stage.

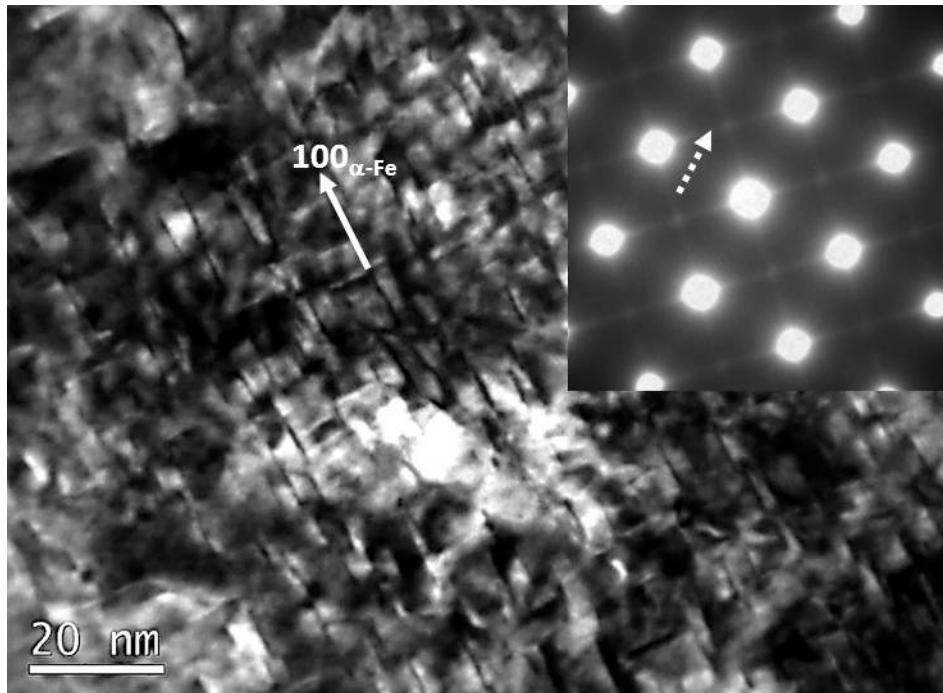


Fig. 4.2: Bright field image and corresponding diffraction pattern of the sample Fe-3.07at.% Mo, nitrided at a temperature of 480 °C for 20 h using a nitriding potential of $r_N = 0.25 \text{ atm}^{-1/2}$. [001] zone axis of ferrite. The streaking has been indicated in the SADP with a white dashed arrow.

The light-optical micrographs of a specimen nitrided for 100 h at a temperature of 480 °C are shown in Fig. 4.3. The nitrided zone can be distinguished from the unnitrided core on the basis of etching-contrast difference since the diffusion zone is less resistant to the etching medium. It follows from Fig. 4.3a that the region adjacent to the grain boundary in the nitrided layer exhibits different etching behaviour than the bulk of the grains. As deduced from the results discussed in section 4.3.2, this is due to preferred precipitation at the grain boundaries.

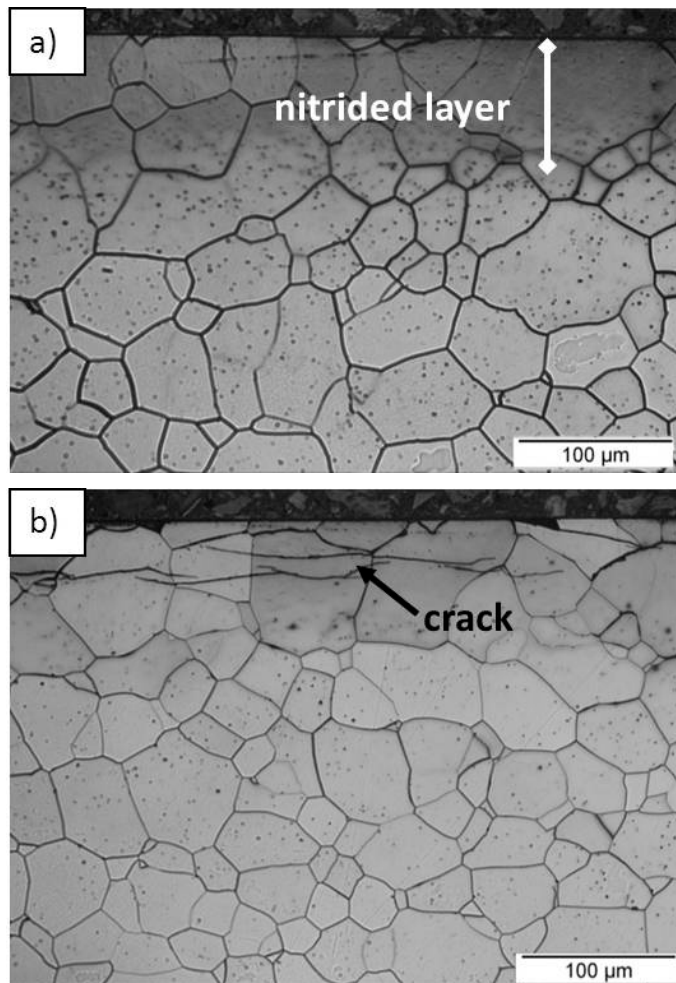


Fig. 4.3: LM-micrographs of the specimen nitrided at 480 °C for 100 h $r_N = 0.25 \text{ atm}^{-1/2}$. The specimen shown in Fig. 4.3a was more severely etched than the specimen shown in Fig. 4.3b in order to obtain a stronger etching contrast.

Trans-granular cracks develop already after a nitriding time of 20 h, suggesting that the nitrided zone is brittle (see Fig. 4.3b) and that tensile residual stresses act perpendicularly to the surface. These cracks grow, upon prolonged nitriding, more or less parallel to the surface of the specimen.

4.3.2 Concentration-depth and microhardness-depth profiles

EPMA concentration-depth profiles of a specimen nitrided for 100 h at 480 °C are shown in Fig. 4.4, as plotted on the corresponding image recorded by scanning electron microscopy (backscatter mode).

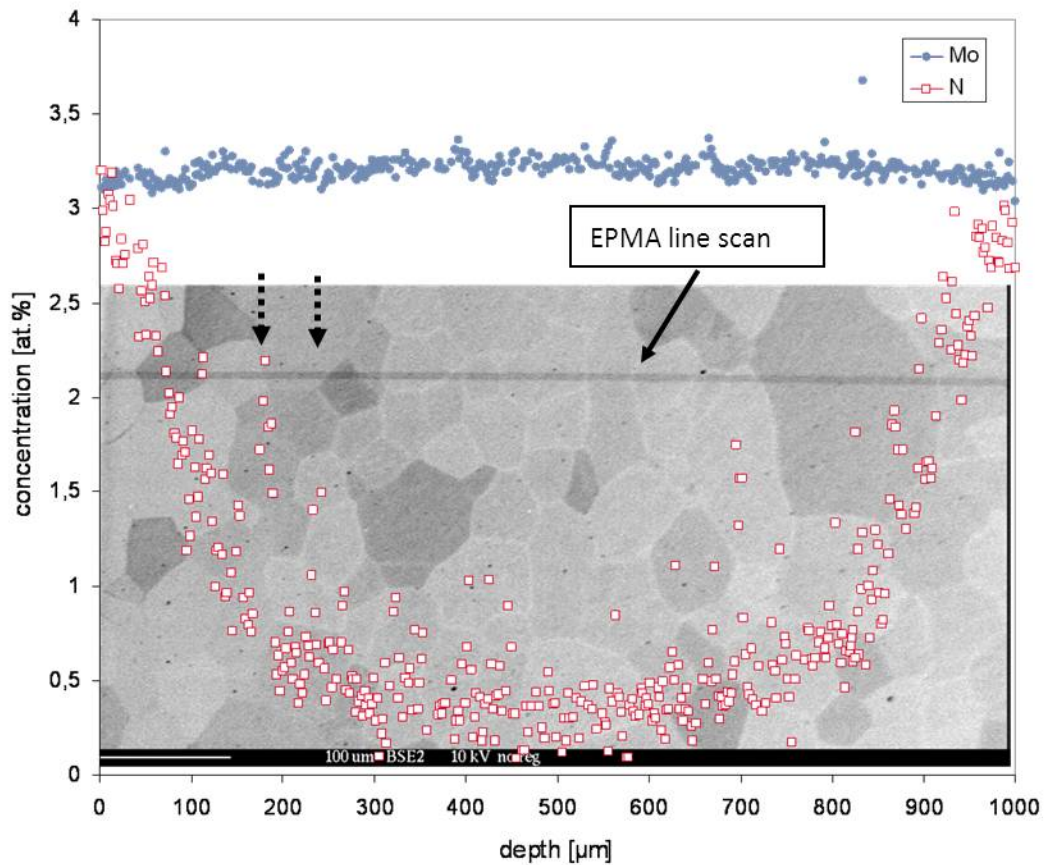


Fig. 4.4: EPMA concentration-depth profile of a specimen nitrided for 100 h at a temperature of 480 °C using a nitriding potential of $r_N = 0.25 \text{ atm}^{-1/2}$. The line scan (marked in the figure by an arrow) was performed along the entire cross section of the specimen.

The nitrogen-penetration depth is small, which can be attributed to the low nitriding temperature (100 h at 480 °C). The molybdenum is distributed more or less evenly over the whole cross section, whereas the nitrogen content shows a pronounced scatter in the nitrided zone. It follows from Fig. 4.4 that the nitrogen content at the grain boundaries exceeds the one in the bulk of the grains by a factor of two (see dashed arrows in Fig. 4.4). This suggests that nucleation of nitride precipitates is favoured at grain boundaries in the nitrided zone (see discussion of etching contrast at grain boundaries in section 4.3.1).

Assuming that the nitride precipitates can be conceived as molybdenum nitrides, the observed value for the nitrogen content in the surface-adjacent region (about 3.2 at.%) can be discussed as follows:

(i) According to [88] (but as observed after coarsening) the fcc-type nitride precipitates have the composition Mo_2N . Thus, an amount of about 1.5 at.% N would be necessary in order to achieve full precipitation of the Mo as Mo_2N in the present, 3-at.% Mo containing specimen. The equilibrium solubility of N in the unstrained ferrite matrix for the given nitriding conditions is about 0.16 at.%. Then, the difference between the observed nitrogen content (3.2 at.%) and the expected nitrogen content (1.5 at.% required for precipitation of Mo_2N and 0.16 at.% which can be dissolved in the unstrained ferrite) is described as excess nitrogen (about 1.54 at.%), located, as dissolved, in the strained matrix surrounding the precipitates and at the precipitate-matrix interfaces (see [31]).

(ii) If the Mo-precipitates would have the composition MoN , a similar calculation as above indicates the presence of a much smaller amount of excess nitrogen (below 0.04 at.%). This observation is rather unlikely since the amount of excess nitrogen is expected to be much higher due to the large number of nano-sized, coherent precipitates. Further, in view of the crystal structure of MoN (the equilibrium, hexagonal modification; cf. section 4.3.1) the precipitation of coherent nitrides is assumed to be very difficult.

The microhardness-depth profiles of the specimens nitrided at 480 °C for 1 h, 2 h, 10 h, 20 h, 50 h and 100 h are shown in Fig. 4.5. A gradual increase of the hardness in the region adjacent to the surface is observed. The increase of the hardness during the early stages of nitriding (up to 2 h at 480 °C) can be attributed to the dissolution of nitrogen in the ferrite matrix, since the nitrogen content, as demonstrated by EMPA, was below the saturation limit of dissolved N in the α -Fe matrix.

The recognition that a distinct built-up of hardness during nitriding occurs only after more than 2 h of nitriding at 480 °C suggests a slow nucleation of the nitride precipitates. As Mo is a nitride former of only intermediate strength (chemical driving force for the precipitation of Mo_2N is about -81 kJ/mol (for VN : -251 kJ/mol) [93]) and because it has a large *volume* misfit with the α -Fe-matrix [21], a non-instantaneous, gradual nitride formation from the supersaturated matrix can be understood.

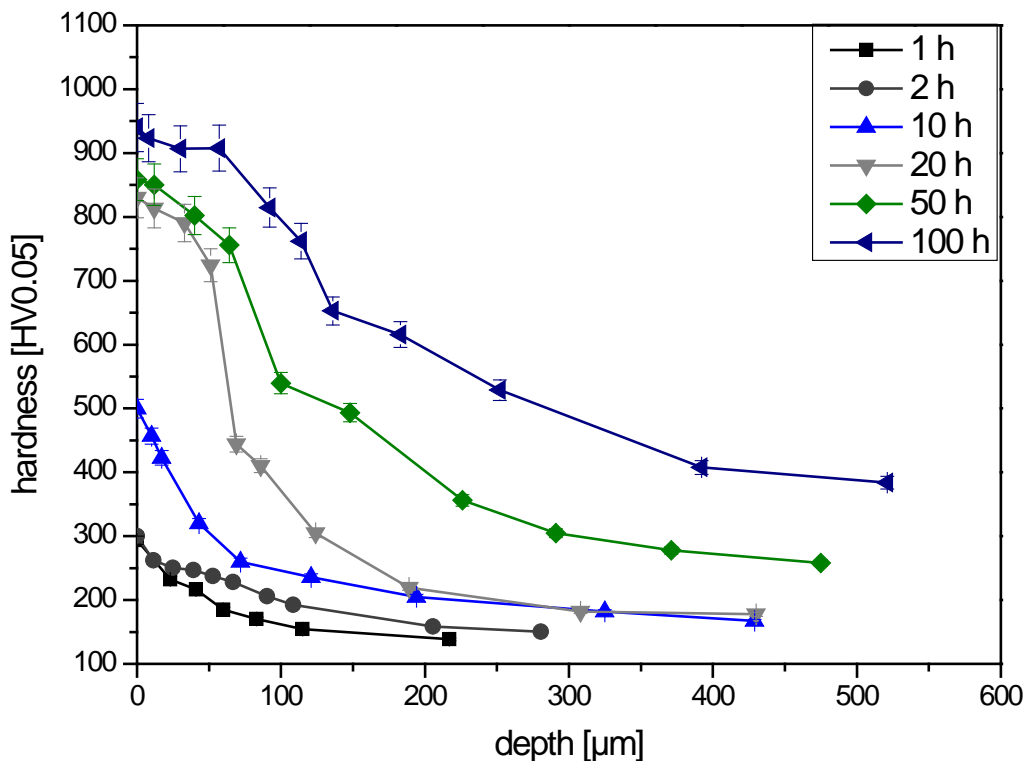


Fig. 4.5: Microhardness-depth profiles of specimens nitrided for various times at a temperature of 480 °C using a nitriding potential of $r_N = 0.25 \text{ atm}^{-1/2}$.

4.3.3 Residual macrostress

The development of the compressive residual stress, parallel to the surface in the near-surface region, is shown in Fig. 4.6a as function of the nitriding time, whereas the development of the surface hardness as function of the nitriding time is shown in Fig. 4.6b. The first increase in compressive residual stress up to a nitriding time of 2 h is caused by nitrogen dissolved in the ferrite matrix, (cf. discussion in section 4.3.2). Beyond a nitriding time of 2 h the formation of (largely coherent; cf. section 4.3.1) nitride precipitates starts. This leads to a strong hardness increase, and a strong increase of compressive residual stress. After passing through a maximum of about 1150 MPa at a nitriding time of 67 h, the compressive residual stress tends to decrease. This could be caused by the progressing nitrogen homogenization of the specimen (see Fig. 4.5): a homogeneously nitrided specimen will not exhibit a macrostress(-depth profile).

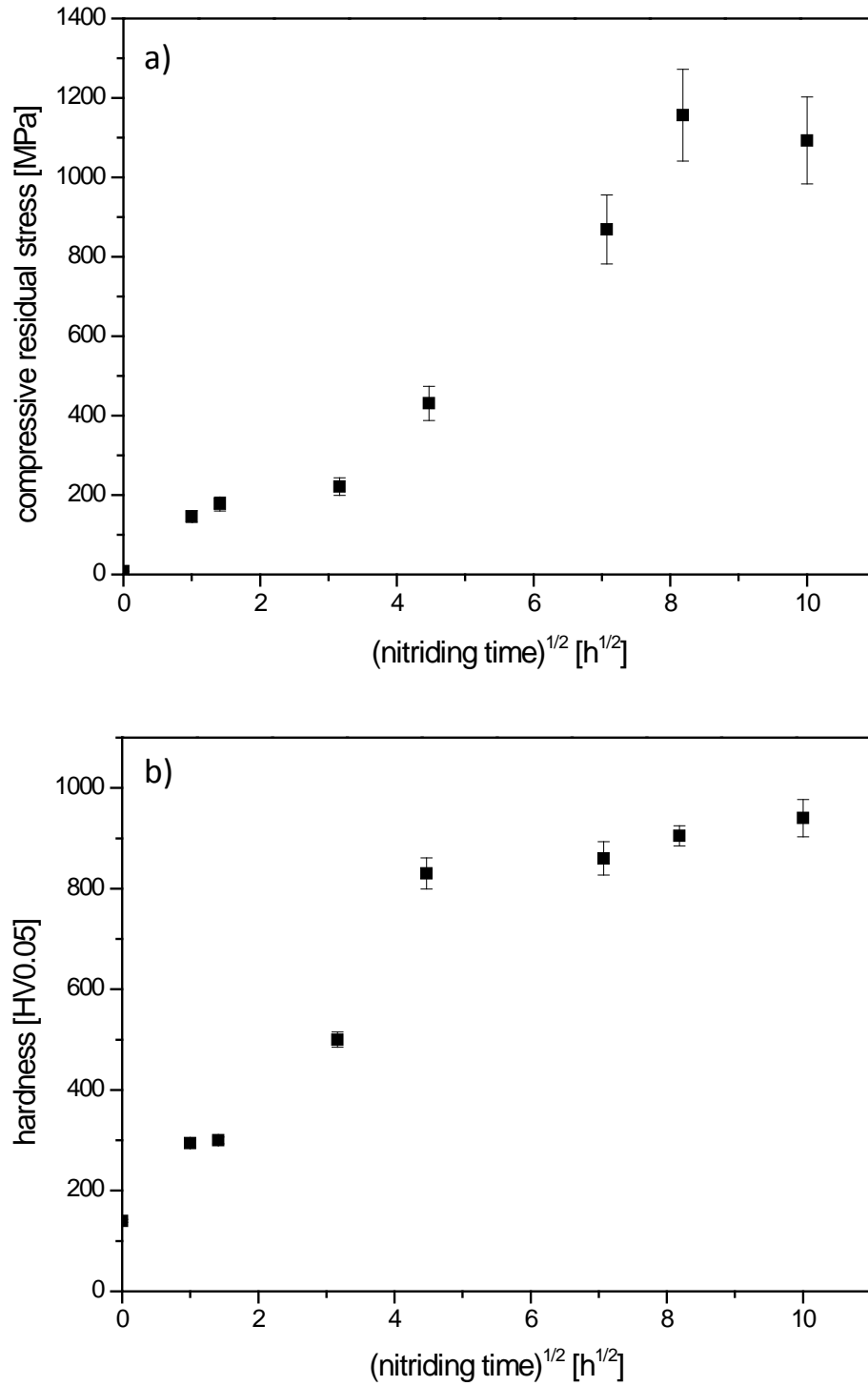


Fig. 4.6: Surface compressive residual stress parallel to the surface (a) and surface hardness (b) as function of the square root of the nitriding time.

4.4 Conclusions

- Upon low-temperature nitriding of Fe-3.07at.% Mo alloy, precipitation of nano-sized platelets along {100} planes of the ferrite matrix occurs. Strongly asymmetric X-ray diffraction ferrite-peak broadening and streaks along $\langle 100 \rangle$ ferrite directions in the selected area electron diffraction pattern suggest that the nitride precipitates are largely coherent with the surrounding ferrite matrix, which is distorted tetragonally due to the precipitate/matrix misfit.
- The precipitation process is not instantaneous upon nitrogen saturation of the ferrite matrix: a gradual development of high hardness and high compressive residual stress occurs.
- Adopting the composition Mo_2N for the largely coherent nitride platelets, it follows that a distinct amount of “excess nitrogen” is taken up.

Acknowledgement

We are grateful to Dipl.-Ing. P. Kress and Mr. J. Köhler for assistance with the nitriding experiments, Mrs. S. Haug for assistance with the EPMA experiments, Mr. W.-D. Lang for TEM sample preparation and Dr. U. Welzel for discussion of the XRD data.

CHAPTER 5

Nitriding behaviour of maraging steel: experiments and modelling

H. Selg, S. Meka, M. Kachel, R. Schacherl, T. Waldenmaier, E.J. Mittemeijer

Abstract

The microstructure and the kinetics of growth of the nitrided zone of a Mo-containing maraging steel was investigated by performing gaseous nitriding at temperatures between 440 °C and 520 °C and at nitriding potentials up to $0.5 \text{ atm}^{-1/2}$ for both solution annealed and precipitation hardened specimens. The microstructure of the nitrided zone was investigated by means of X-ray diffraction (phase constitution; crystal imperfection). Fine, initially largely coherent Mo_2N -type precipitates developed in the nitrided zone. The elemental concentration-depth profiles were determined employing Glow Discharge Optical Emission Spectroscopy (GDOES). The nitrogen content within the nitrided zone exceeds the nitrogen content expected on the basis of the molybdenum content and the equilibrium solubility of nitrogen in a (stress-free) ferritic matrix: excess nitrogen occurs. A numerical model was applied to predict the nitrogen concentration-depth profile within the nitrided layer. The model describes the dependence on time and temperature of the nitrogen concentration-depth profiles with, as fit parameters, the surface nitrogen concentration, the diffusion coefficient of nitrogen in the matrix, a composition parameter of the formed nitride and the solubility product of the nitride forming element and dissolved nitrogen in the matrix. Initial values for the surface nitrogen concentration and the composition parameter were determined experimentally with an absorption isotherm and fitted to the measured nitrogen concentration-depth profiles. The results obtained revealed the striking effects of the amount of excess nitrogen and the extent of precipitation hardening on the developing nitrogen concentration-depth profile.

5.1 Introduction

Maraging steels are a group of nickel-alloyed steels having a practically carbon-free martensitic structure and which are age hardened by the precipitation of one or more intermetallic compounds [35, 36]. Since their development in the early 1960s by the International Nickel Company (INCO), this class of steels has attracted much interest and is used in many technical applications ([37, 38]) due to their high strength, high fracture toughness, high strength to weight ratio and good weldability. The martensitic transformation is induced by air cooling³ from the solution annealing temperature in the austenite-phase region. Due to the very low content of interstitials (C, N) the martensite phase is usually of cubic crystal structure and relatively soft. Upon subsequent age hardening, extremely fine, coherent intermetallic compounds such as Ni₃X (X = Ti, Mo, V, W) develop [35, 36].

As other alloyed steels, maraging steels are often subjected to an additional, specific thermochemical heat treatment in order to improve the fatigue properties [52]. Gaseous nitriding is one of the most widely applied of such surface engineering treatments. In the past, only a few, moreover largely phenomenological studies were devoted to the nitriding behaviour of maraging steels, mainly to measure the improvement of the mechanical properties [94, 95]. Little is known about the microstructure and the growth kinetics of the nitrided zone. In the present study the microstructural development of the diffusion (nitrided) zone and its growth kinetics were investigated by performing nitriding experiments at controlled chemical potential of nitrogen in the nitriding (gaseous) atmosphere. Both the nitriding response of purely martensitic (solution annealed and quenched) specimens and of subsequently age hardened specimens were studied. As a result, a numerical model quantitatively describing the growth kinetics of the diffusion zone was developed (see sec. 5.2). The modelling required distinction of the different types of nitrogen uptake [19], as

³ In case of maraging steels, air cooling from the solution annealing temperature to room temperature is sufficient to obtain the completely martensitic microstructure.

discussed for iron-based alloys in Ref. [31]. For quantitative assessment so-called nitrogen-absorption isotherms were determined.

5.2 Modelling the kinetics of growth of the nitrified zone

Nitriding of iron-based alloys containing nitride forming alloying elements Me (Me = Al, Cr, Mo, V,...) leads to the development of nano-sized alloying element nitride precipitates in the ferrite matrix (i.e. diffusion zone) [1, 3, 15, 20, 27]. The shape of the resulting nitrogen concentration-depth profile strongly depends on the “strength of the interaction” [31] between nitride forming element and nitrogen. A number of models for describing the nitriding kinetics have been proposed in the literature. In the following, after having indicated very briefly the classical model for “strong” Me-N interaction, a synopsis of the most general, recent treatment of weak to strong interaction and incorporating the different effects of the different types of absorbed nitrogen is presented, which is necessary for understanding this paper. The present maraging steel has been modeled as a binary Fe-Mo alloy, as Mo is the only nitride forming element in it.

The simplest model for the case of strong interaction between Me and N (the presence of only one nitride forming element is supposed) provides an analytical expression for the nitriding kinetics at constant temperature, which was originally derived for internal oxidation [15, 96]:

$$z^2 = \frac{2C_s^N D_N}{nC_{Me}} t \quad (5.1),$$

where z denotes the extent of the diffusion zone (depth under the surface) across which all of the nitride forming alloying element has precipitated as nitride, C_s^N is the dissolved nitrogen concentration at the specimen surface, D_N is the diffusivity of nitrogen in the matrix, n denotes the stoichiometry of the MeN_n precipitates, C_{Me} is the concentration of the initially dissolved Me in the matrix and t denotes the nitriding time. Hence, a parabolic relationship should occur between the nitriding time and the

thickness of the diffusion layer at constant temperature. Equation (5.1) presupposes that a sharp “interface” occurs between the nitrated case and the unnitrated core. In case of intermediate interaction between Me and N, a shallow transition between the nitrated case and the unnitrated core occurs. If (ideally) weak interaction prevails, the transition between nitrated case and unnitrated core vanishes resulting in a constant nitrogen content independent of the depth in the specimen, i.e. precipitation of Me-N takes place at the same time at each depth (“bucket that fills up”). The shape of the transition between the nitrated case and the unnitrated core is governed by the solubility product of Me and N in the matrix, K_{MeN_n} , with respect to the nitride MeN_n , (see below). Moreover, it has been found that a distinction has to be made between the different types of absorbed nitrogen (immobile and mobile excess nitrogen; see below) in order to model the nitrogen diffusion-depth profile successfully [19]. The nitrogen taken up upon nitriding of an iron-based alloy (Fe-Al [97], Fe-Cr- [15, 18], Fe-Ti [27, 29], Fe-V [30] and Fe-Mo [98]) generally exceeds the so-called normal nitrogen content. The expected normal nitrogen content is the sum of the equilibrium content of nitrogen dissolved in the unstrained matrix and the nitrogen needed to precipitate the entire amount of alloying element as nitride, MeN_n . The nitrogen in excess of the normal nitrogen is called “excess nitrogen”.

Two types of excess nitrogen have been distinguished [30, 31]:

- i) nitrogen adsorbed at the precipitate/matrix interface,
- ii) nitrogen dissolved additionally (with respect to the equilibrium amount of dissolved nitrogen (i.e. in the absence of misfit stresses)) in the strained matrix, due to volume misfit between nitride precipitate and ferrite matrix.

The first type of the above listed excess nitrogen (i) is denoted as *immobile* excess nitrogen as this nitrogen is not able to diffuse. The second type of excess nitrogen (ii) is referred to as *mobile* excess nitrogen, as it participates in the diffusion flux. The effect of the different kinds of excess nitrogen on nitriding kinetics is different: the mobile excess nitrogen increases the extent of the diffusion zone, whereas the immobile excess

nitrogen tends to decrease the extent of the diffusion zone. These considerations have led to the following set-up of a numerical model for the nitriding kinetics:

The inward diffusion of nitrogen can be expressed by Fick's second law, as follows:

$$\frac{\partial c_{N_\alpha}(z,t)}{\partial t} = D_N(T) \frac{\partial^2 c_{N_\alpha}(z,t)}{\partial z^2} \quad (5.2),$$

with c_{N_α} being the concentration of nitrogen dissolved in the ferrite matrix at depth z at given temperature T , and given time t . $D_N(T)$ is the temperature dependent (concentration independent, recognizing the very low nitrogen solubility in the matrix [9]) diffusion coefficient of nitrogen in the matrix.

The formation of the alloying element nitride, MeN_n , from alloying element Me and nitrogen N , both being dissolved in the matrix, can be written as:



The equilibrium constant K_e of the above reaction is given by:

$$K_e = \frac{1}{[Me] \cdot [N]^n} = \frac{1}{K_{MeN_n}} \quad (5.4),$$

with K_{MeN_n} as the solubility product. Precipitation of MeN_n will take place at any depth within the diffusion zone once the solubility product is surpassed and the precipitation of nitride occurs until the solubility equilibrium has been established:

$$[Me] \cdot [N]^n > K_{MeN_n} \quad (5.5).$$

The presence of (immobile) excess nitrogen is incorporated by replacing the stoichiometric parameter n from equation (5.3) with a parameter b according to:

$$b = n + y \quad (5.6),$$

with y representing the contribution of the immobile excess nitrogen.

On the above basis, the calculation of the nitrogen concentration-depth profiles runs as follows: first, the concentration of nitrogen at every time step for every depth is calculated by solving Fick's second law (Eq. 5.2) numerically with a finite-difference (explicit) solution method as described in Refs. [19, 99, 100]. Then, the amount of

dissolved alloying element content is calculated at every time step for every depth and the value of the solubility product of MeN_n is calculated. If the solubility product surpasses its equilibrium value, precipitation of MeN_n will take place at this location until $[\text{Me}] \cdot [\text{N}]^n = K_{\text{MeN}_n}$.

Thus, the nitrogen concentration-depth profile can be numerically calculated iteratively adopting starting values for following fit parameters:

- the surface concentration of dissolved nitrogen, $c_N^s = [N]_{\alpha\text{-Fe}}^0 + [N]_{\alpha\text{-Fe}}^{\text{strain}}$ with $[N]_{\alpha\text{-Fe}}^0$ as the solubility of nitrogen in the unstrained, ferrite matrix and $[N]_{\alpha\text{-Fe}}^{\text{strain}}$ as the solubility of nitrogen in the strained matrix in excess to $[N]_{\alpha\text{-Fe}}^0$,
- the composition parameter $b = n + y$,
- the solubility product K_{MeN_n} ; can be estimated according to Ref. [101] on the basis of standard Gibbs energy of formation of MeN_n ,
- the diffusion coefficient of nitrogen in the matrix, D_N ; can, in case of a ferrite matrix, be assessed using literature data [9].

Values of $[N]_{\alpha\text{-Fe}}^{\text{strain}}$ and b have been obtained in this study experimentally from nitrogen-absorption isotherm determinations. These values were used as starting values in the fitting procedure. The influence of the fitting parameters is explained as follows:

- (i) *Effect of C_N^s* : If the surface concentration of dissolved nitrogen increases, the *total* nitrogen content increases and also the nitriding depth increases with increasing C_N^s due to a larger concentration gradient of the mobile nitrogen.
- (ii) *Effect of b* : If b increases, the *total* nitrogen concentration increases because the amount of adsorbed nitrogen increases. This leads, in contrast to an increasing surface concentration of dissolved nitrogen, to a decrease of the extent of the nitrided zone.

- (iii) *Effect of K_{MeN_n}* : The solubility-product value changes the “slope” of the “interface” between the nitrided case and the unnitrided core. If K_{MeN_n} decreases, as for strong nitride forming elements such as Ti or V, this “interface” becomes less diffuse.
- (iv) *Effect of D_N* : A larger value of the diffusion coefficient obviously increases the depth of the nitrided zone and makes the “case/core interphase” more diffuse.

5.3 Experimental

5.3.1 Specimen preparation

For the investigations a commercially available maraging steel (Imphy alloys, Arcelor Group, France) was used. The chemical composition, including the amounts of impurities, was determined using chemical analysis (inductively coupled plasma - optical emission spectroscopy, combustion method and carrier gas hot extraction). The results are shown in Table 5.1.

Table 5.1: Amounts of main alloying elements and impurities for the maraging steel used in this work

(balance: Fe).

maraging steel	composition [wt.%]	composition [at.%]
Ni	17.9 ± 0.2	17.7
Co	16.6 ± 0.2	16.4
Mo	5.48 ± 0.06	3.3
Cr	0.072 ± 0.001	0.08
Cu	0.062 ± 0.001	0.06
Ti	≤ 0.002	< 0.0025
O	0.024 ± 0.006	0.05
N	0.0034 ± 0.0005	0.014
C	0.0095 ± 0.0009	0.045

The as-supplied sheets (thickness approximately 400 μm) were cut into rectangular specimens (lateral dimensions: about 15 x 10 mm^2) and a hole was drilled (\varnothing : 1.5 mm) in them for fixing them later during the age hardening and nitriding treatments. The specimens were ground, cleaned in an ultrasonic bath using ethanol and then encapsulated in a quartz tube which was filled with argon gas (purity: 99.999 vol.%). Subsequently, the specimens were solution annealed in a muffle furnace at 880 $^{\circ}\text{C}$ for 30 min. Before nitriding, the specimen surfaces were polished mechanically (final step: 1 μm diamond suspension), cleaned with ethanol in an ultrasonic bath and dried in a nitrogen gas flow.

5.3.2 Nitriding

The nitriding experiments were performed at different calibrated temperatures (440 $^{\circ}\text{C}$, 460 $^{\circ}\text{C}$, 480 $^{\circ}\text{C}$ and 520 $^{\circ}\text{C}$; temperature accuracy: ± 1 $^{\circ}\text{C}$) in a vertical, multizone quartz-tube furnace (\varnothing : 28 mm) with a NH_3/H_2 gas mixture using a total gas flux of 500 ml/min (purity NH_3 : > 99.998 vol.%, purity H_2 : 99.999 vol.%). The gas fluxes were adjusted by calibrated mass flow controllers and corresponded to a nitriding potential, $r_{\text{N}} = \frac{P_{\text{NH}_3}}{P_{\text{H}_2}^{3/2}}$

[8], of 0.5 $\text{atm}^{-1/2}$. The nitriding potential was chosen such that no γ' -iron nitrides develop at the surface. Hence, the nitrided layer only consists of a diffusion zone. The nitriding process was terminated by breaking mechanically the quartz fibre at which the specimen was suspended in the furnace and for which the hole was drilled so that the specimen fell into a flask filled with water. In order to minimize the risk of specimen oxidation, the water in the quenching flask was rinsed with N_2 (for about 15 min) before specimen quenching.

Some of the specimens were subjected to an age hardening treatment (until peak hardness was reached) at 480 $^{\circ}\text{C}$ for 2 h in a H_2 atmosphere prior to the nitriding treatment. All other specimens were nitrided in the soft condition, i.e., directly after solution annealing. In the following, the specimens nitrided (at temperatures in the range of 460 $^{\circ}\text{C}$ to 520 $^{\circ}\text{C}$) in the soft condition are denoted with "A", whereas the

specimens subjected to age hardening before nitriding (at 440°C) are denoted with “B”. Note that in the specimens of type “A” nitriding and age-hardening processes could occur simultaneously.

The nitriding (and pre-treatment) parameters used in the present work have been listed in Table 5.2.

Table 5.2: Nitriding parameters employed in the present work. The specimens “A” were nitrided in the solution annealed state, whereas specimens “B” were age-hardened prior to nitriding.

specimen type	pre-(aging) treatment	nitriding temperature [°C]	nitriding time [h]	nitriding potential [atm ^{-1/2}]
A	-	460, 480, 520	0.5 - 6	0.5
B	2 h at 480 °C in pure H ₂	440	1 - 21	0.5

5.3.3 Determination of nitrogen-absorption isotherms

For the determination of the absorption isotherm, i.e. the dependence of nitrogen uptake on the nitriding potential at constant temperature, a thin foil of approximately 60 µm thickness was prepared by cold-rolling and mechanical grinding followed by a solution annealing treatment as described in sec. 5.3.1. Subsequently, one such specimen was age hardened at 480 °C under H₂ atmosphere for 2 h (thus peak hardness was reached). Next, both the solution annealed specimen and the solution annealed and age hardened specimen were pre-nitrided to saturation level of nitrogen uptake in order to obtain a homogeneous precipitation morphology throughout the cross section of the specimen. This pre-nitriding was performed at 480 °C for 110 h with a nitriding potential of 0.25 atm^{-1/2} (i.e. until no further nitrogen uptake occurred). A subsequent denitriding was performed in pure H₂ atmosphere at 450 °C for 70 h (i.e. until no further decrease of mass of the specimen occurred) under pure H₂ atmosphere to remove less strongly

bonded interstitially dissolved nitrogen. The nitrogen-absorption isotherms of both specimens were determined at a temperature below the pre-nitriding temperature, (i.e. at 440 °C) in order to avoid any change in nitride-precipitate morphology during the course of absorption-isotherm measurements. For the nitrogen-absorption isotherm determinations, the pre-nitrided foils were subjected to nitriding at different nitriding potentials (listed in Table 5.3) until the saturation level of nitrogen uptake was reached (which was achieved after nitriding for 20 h).

Nitrogen uptake (or loss) was determined by weighing the specimen before and after the experiment using a Mettler microbalance (accuracy: 1 µg). The average of at least 5 weight measurements was taken for the determination of the nitrogen uptake (as compared to the unnitrided specimen). The error bars indicated in Fig. 5.2a and b represent the standard deviation for that average value.

Table 5.3: Nitriding potential, r_N , and corresponding flow-rates of NH_3 and H_2 used for the determination of the absorption isotherms.

r_N [atm ^{-1/2}]	NH_3 [ml/min]	H_2 [ml/min]
0.02	10	490
0.05	23	477
0.08	36	464
0.09	40	460
0.12	50	450
0.14	58	442
0.2	78	422
0.3	105	395
0.4	128	372
0.5	148	352

5.3.4 Specimen characterization

5.3.4.1 Light microscopy (LM)

For LM investigations a piece of each nitrided specimen was cut off (Struers Accutom 50, Al₂O₃ cut-off wheel), embedded in Struers PolyFast, ground and polished (final polishing step: 1 µm diamond suspension). Each cross section was etched with 2 % Nital (2 vol.% HNO₃ in ethanol) at room temperature for about 10 s. LM micrographs were taken using a Zeiss Axiophot microscope equipped with a digital camera (Olympus ColorView IIIu).

5.3.4.2 Microhardness measurement

Microhardness measurements on cross sections (for determination of hardness-depth profiles) and on the surfaces of nitrided specimens were carried out with a Vickers microhardness tester (Leica VMHT Mot) applying a load of 490 mN and a dwell time of 10 s.

5.3.4.3 X-ray diffractometry

Phase analysis by means of X-ray diffraction was performed for all specimens before and after nitriding using a PANalytical X'Pert Multi-Purpose Diffractometer (MPD) with Co-K_α radiation. This instrument uses Bragg-Brentano geometry and is equipped with a graphite monochromator in the diffracted beam. The diffraction-angle range (30 ° < 2θ < 120 °) was scanned in steps of 0.06 ° with a counting time of 600 s per step. For the identification of the phases, based on the positions of the diffraction peaks, data of the ICDD database were used [51].

Residual stress measurements were carried out applying the sin²ψ-method [102]. Stress values were obtained for the case of a macroscopically elastically isotropic specimen with a plane, rotationally symmetric biaxial state of stress ($\sigma_{11} = \sigma_{22} = \sigma_{\parallel}$; experimentally proven to be applicable). The measurements were performed using a PANalytical X'Pert Materials-Research Diffractometer (MRD), equipped with an Eulerian

cradle and a graphite monochromator in the diffracted beam, applying a quasi-parallel beam geometry and Co- K_{α} radiation. The Fe 211 reflection was scanned in the range of $95^{\circ} < 2\theta < 105^{\circ}$ in steps of 0.08° using a counting time of 25 s per step, at various values of the specimen-tilt angle ψ . Lattice strains were calculated from the peak position of the Fe 211 reflection in dependence on ψ . The measured diffractograms of the Fe 211 reflection were evaluated by fitting Pseudo-Voigt functions using a custom peak fit program which, besides other fit parameters, refines the position of the peak maximum. For calculation of the stress parallel to the surface, σ_{\parallel} , from the slope, macroscopic elastic constants ($S_1 = -\frac{\nu}{E}$ and $\frac{1}{2}S_2 = \frac{1+\nu}{E}$ with ν as the Poisson ratio and E as the Young's modulus) were calculated from data for ν and E from [103] for a maraging steel of grade 350.

5.3.4.4 Glow Discharge Optical Emission Spectroscopy

The elemental concentration-depth profiles were determined with a glow discharge optical emission spectroscope (GDOES) (electron probe micro-analysis (EPMA) could not be used due to overlap of the N- K_{α} line with especially the Co- L_{α} line; cf. Table 5.1). This instrument (GDA 650 (Spektruma GmbH)), operated at 30 KV and 15 mA, was equipped with high-resolution CCD optics. The focal spot was 2.5 mm. Prior to the measurement, the specimens were electrolytically nickel plated in order to determine an accurate surface nitrogen-concentration (i.e. to minimize the effect of surface contaminations). The nickel plating was carried out in a Watts bath at 70°C and at a voltage of 3.5 V [104].

5.4 Results and discussion

5.4.1 Nitrogen-absorption isotherms

For quantitative determination of the (types of) excess N taken up by nitrided maraging steel, nitrogen-absorption isotherms were determined for both the solution annealed condition and the age hardened condition. In order to avoid change in size and morphology of the nitride (Mo_2N ; see sections 5.4.2.1 and 5.4.3.1) precipitates during the course of the absorption-isotherm measurements, the specimens had been pre-nitrided, to obtain homogeneously through nitrided specimens, at a distinctly higher temperature (480 °C) than the temperature (440 °C) at which the absorption isotherms were determined (cf. section 5.3.3). After pre-nitriding (480 °C, 110 h, r_N 0.25 atm^{-1/2}) a saturation level of nitrogen uptake of 2.35 at.% N for the age hardened specimen and 2.32 at.% for the solution annealed specimen was determined. The expected normal nitrogen uptake ($[\text{N}]_{\text{normal}} = [\text{N}]_{\text{Mo}_2\text{N}} + [\text{N}]_{\alpha\text{-Fe}}^0$) after pre-nitriding is 1.78 at.% ($[\text{N}]_{\text{Mo}_2\text{N}} = 1.64$ at.% and $[\text{N}]_{\alpha\text{-Fe}}^0 = 0.14$ at.% [9]). Thus, it follows for the total amount of excess nitrogen: $[\text{N}]_{\text{excess}} = [\text{N}]_{\text{total}} - [\text{N}]_{\text{normal}} = 2.35$ at.% - 1.78 at.% = 0.57 at% for the age hardened specimen and $[\text{N}]_{\text{excess}} = 0.54$ at. % for the solution annealed specimen.

The X-ray diffraction patterns, taken after the nitrogen-absorption isotherm determinations, (i.e. after pre-nitriding at 480 °C, followed by denitriding at 450 °C and again nitriding at 440 °C during isotherm determination) show, for both types of specimen, apart from matrix reflections, reflections from a fcc-type Ni-rich phase ($\text{Fe}_{0.64}\text{Ni}_{0.36}$ (identified according to ICDD card No. 00-047-1405) and also reflections originating from the Mo_2N phase can be discerned (see Fig. 5.1). The formation of the fcc $\text{Fe}_{0.64}\text{Ni}_{0.36}$ phase is the consequence of the dissolution of N as austenite (fcc) stabilizing element and the removal of the ferrite stabilizing element Mo from the matrix. This Ni-rich, austenitic phase occurs only after prolonged, excessive heat treatment (e.g. after nitriding at 500 °C for 72 h and after the cumulative nitriding experiments performed for a single specimen during nitrogen-absorption isotherm

determination) but does not occur for shorter times, which pertains to the experiments described in the following sections.

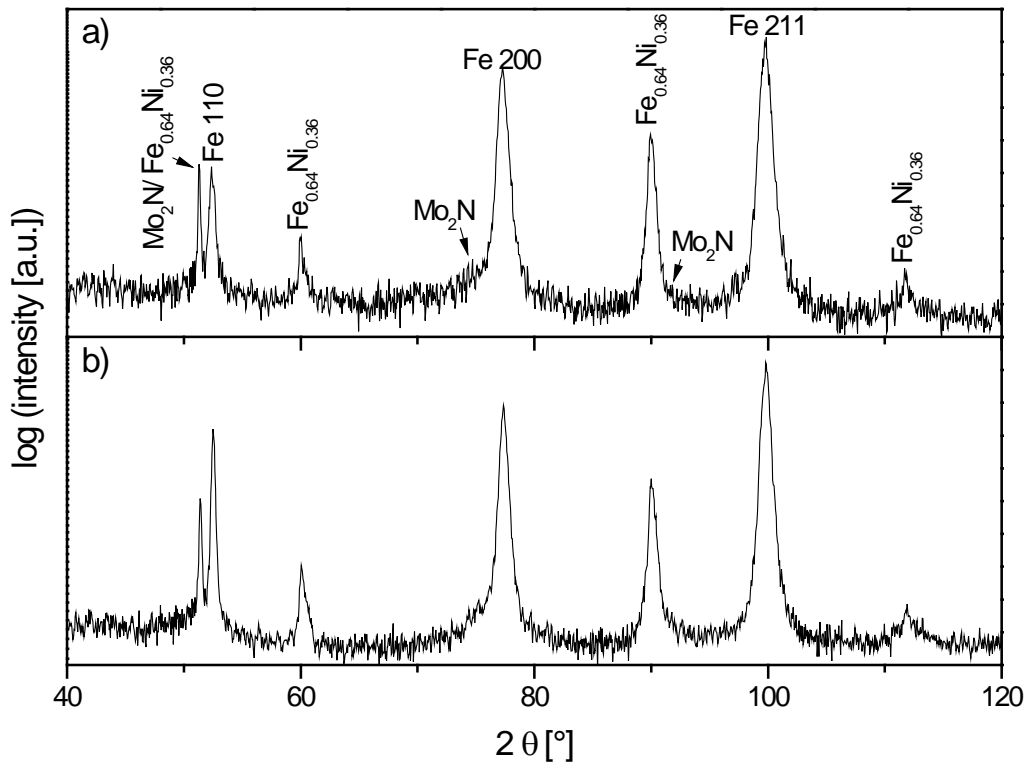


Fig. 5.1: X-ray diffraction patterns taken from the solution annealed specimen (a) and from the solution annealed and age hardened specimen (b) used for the nitrogen-absorption isotherm determinations, after the last nitriding step performed in the nitrogen-absorption isotherm determinations, at the temperature of 440 °C for 20 h employing a nitriding potential of $0.5 \text{ atm}^{-1/2}$ and subsequent quenching to room temperature.

The results of the nitrogen-absorption isotherm measurements have been gathered in Fig. 5.2 for the solution annealed specimen (a) and for the solution annealed and age hardened specimen (b). The level of nitrogen in the specimen after denitriding has been indicated by the black solid lines in Figs. 5.2a and b; level I. The expected amount of nitrogen required to form Mo₂N-type precipitates has been indicated by the light solid grey line; level II. The difference of levels I and II can be ascribed to the amount of immobile excess nitrogen (adsorbed at the nitride platelets; cf. section 5.2). The amount of interstitially dissolved nitrogen increases linearly with the nitriding

potential at constant temperature [8]. Therefore, the unfilled, black circles above the level of denitriding (level I) represent the amount of nitrogen dissolved in the (strained by the largely coherent Mo₂N-type precipitates) matrix. Fitting of a straight line to these data points leads to the black dashed lines in Figs. 5.2a and b, which intersect the ordinate at $r_N = 0$ at the nitrogen level as after denitriding. The difference between the dashed line and the grey dotted line, representing the nitrogen solubility in an unstrained, ferritic matrix, can be attributed to the amount of mobile (dissolved) excess nitrogen. Thus, the amount of nitrogen that can be dissolved in the strained matrix at a nitriding potential of $0.52 \text{ atm}^{-1/2}$ equals 0.50 at.% in case of the solution annealed specimen and 0.40 at.% in case of the age hardened specimen, whereas in a pure, unstrained ferrite matrix the solubility is 0.14 at.% [9]: hence, at this nitriding potential the amount of mobile excess nitrogen is 0.38 at.% for the solution annealed specimen and 0.26 at.% for the solution annealed and age hardened specimen. This difference in the amounts of mobile excess nitrogen is ascribed to smaller nitride precipitates developing upon nitriding of solution annealed specimens (see results and discussion in sections 5.4.2.1 and 5.4.3.1).

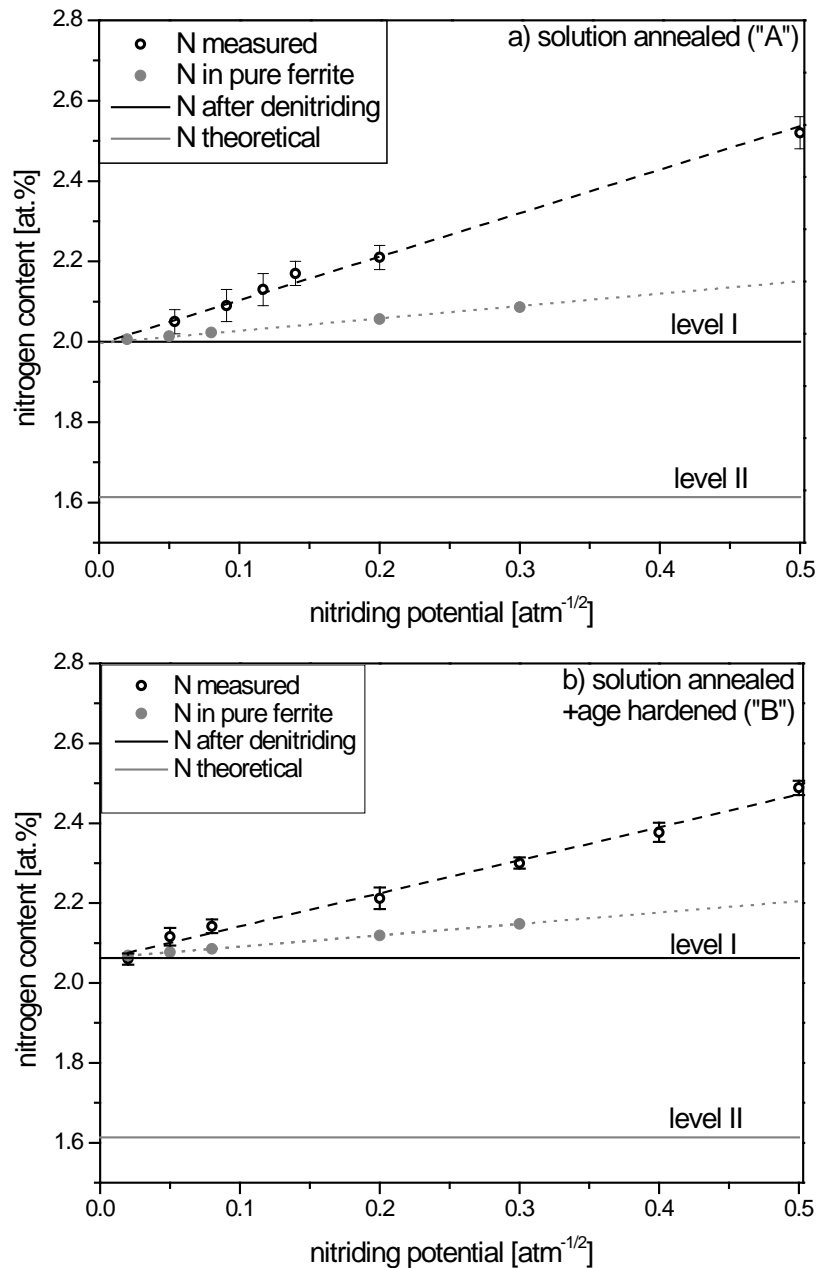


Fig. 5.2: Nitrogen-absorption isotherms determined at the temperature of 440 °C for the solution annealed specimen ("A") (a) and the solution annealed and age hardened specimen ("B") (b) after prenitriding (homogeneously through nitriding) at the temperature of 480 °C for 90 h followed by denitriding thereby removing all N dissolved in the matrix. The remaining nitrogen content in the specimen after denitriding is indicated by the horizontal straight black line (level I). The theoretical required nitrogen content to cause complete precipitation of Mo as Mo₂N is given by the grey horizontal line (level II). The black unfilled circles represent the nitrogen contents determined by weighing for each particular nitriding potential. The grey round points correspond to the equilibrium solubility of nitrogen in pure, unstrained ferrite calculated from data given in Ref. [9].

5.4.2 Nitriding of solution annealed maraging steel (specimens “A”)

5.4.2.1 Microstructure

Cross sections of maraging steel specimens nitrided for 4 h with a nitriding potential of $0.5 \text{ atm}^{-1/2}$ at 480 °C and 520 °C are shown in Figs. 5.3a and b. The typical plate-like microstructure of maraging steels [35, 95] can be seen in the unnitrided core. The diffusion zone adjacent to the surface (the extent of the diffusion zone has been indicated with a black dashed line in the figures) shows an etching contrast different from the unnitrided core. No hints of austenite can be seen in the micrographs, which is compatible with the XRD phase analysis discussed below (see Fig. 5.7).

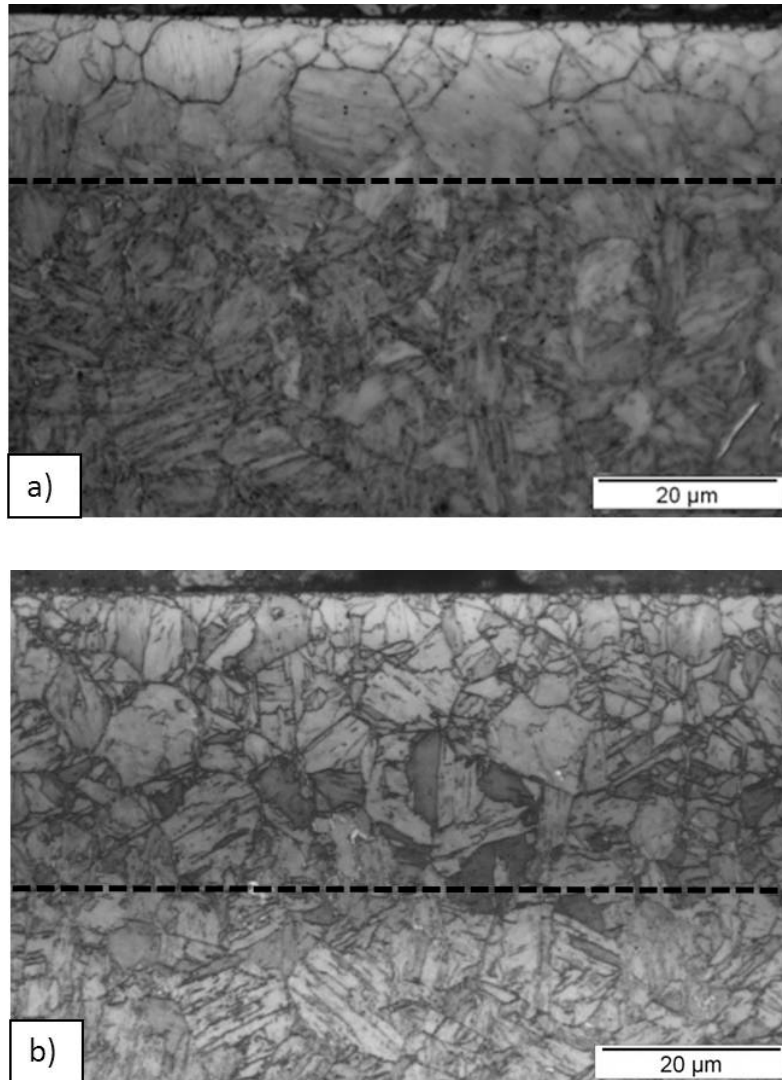


Fig. 5.3: LM micrograph of specimens (type “A”) nitrided at (a) the temperature of 480 °C for 4 h and (b) at the temperature of 520 °C for 4 h, each with a nitriding potential of $0.5 \text{ atm}^{-1/2}$. The extent of the nitrided zone has been marked with a dashed line.

The surface micro-hardness (measured on the surface) increases initially strongly with increasing nitriding time until a maximum value of about 1050-1100 $\text{HV}_{0.05}$ is obtained (Fig. 5.4). The first, very strong hardness increase after a nitriding time of 0.5 h, from 300 $\text{HV}_{0.05}$ (corresponding to the micro-hardness value of the solution annealed state) to about 900 $\text{HV}_{0.05}$ (at a nitriding temperature of 460 °C) or to about 1000 $\text{HV}_{0.05}$ (at nitriding temperatures of 480 °C and 520 °C), is ascribed to the precipitation of

nitrides *and* of intermetallic compounds (compare Figs. 5.4 and 5.5). Upon prolonged nitriding, the micro-hardness decreases due to (over-)aging of the initially largely coherent precipitates.

The (XRD) surface compressive residual stress ($\sigma_{\parallel} = \sigma_{11} = \sigma_{22}$) evolution as function of nitriding time for different nitriding temperatures is shown in Fig. 5.6 (at $t = 0$, $\sigma_{\parallel} = 0$). At all nitriding temperatures, the surface compressive residual stress increases with increase in nitriding time to a maximum value and then decreases upon continued nitriding. At 520 °C, a maximum (measured) compressive residual stress of -460 MPa was reached already after 0.5 h of nitriding, followed by a strong decrease with increasing nitriding time. This decrease upon continued nitriding is the natural consequence of the proceeding homogenization of the specimen, supported by overaging of the formed nitrides and the intermetallic compound particles (cf. Fig. 5.4). X-ray diffraction phase analysis indicates that after a nitriding time of 0.5 h at 520 °C, only reflections originating from the matrix can be detected (Fig. 5.7a). In this case, significant peak broadening, especially of the Fe 200 reflection (Fig. 5.8), occurs indicating that upon the development of largely coherent nitride precipitates coherent diffraction of the nitrides with the ferrite matrix can occur [45, 52, 54]: The cubic ferrite matrix surrounding the nitride precipitate gets tetragonally distorted due to the occurrence of highly coherent nitride/matrix interface and the large volume misfit between nitride and matrix. This results in the asymmetric peak broadening (in particular of 200 peak) as the peaks from cubic and tetragonal ferrite overlap [45]. Upon increased nitriding time (2 h and 6 h at 520 °C), additional reflections corresponding to Mo₂N emerge (Fig. 5.7b), suggesting that the initially, very fine and coherent Mo₂N-type precipitates, upon continued nitriding, get incoherent, leading to the appearance of separate precipitate reflections (cf. Figs. 5.7b and a) and associated by decreased microhardness (Fig. 5.4) and matrix diffraction-line broadening (Fig. 5.8).

It has been shown for binary Fe-Mo alloys that, upon nitriding, the cubic Mo₂N-type nitride precipitates in the early stages of nitriding, which Mo₂N precipitates are subsequently replaced by hexagonal MoN by a discontinuous precipitation reaction [65].

This $\text{Mo}_2\text{N} \rightarrow \text{MoN}$ transition appears to be hindered in the maraging steel (upon nitriding at comparatively low temperature), likely as a consequence of grain-boundary pinning by the presence of small (intermetallic) precipitates.

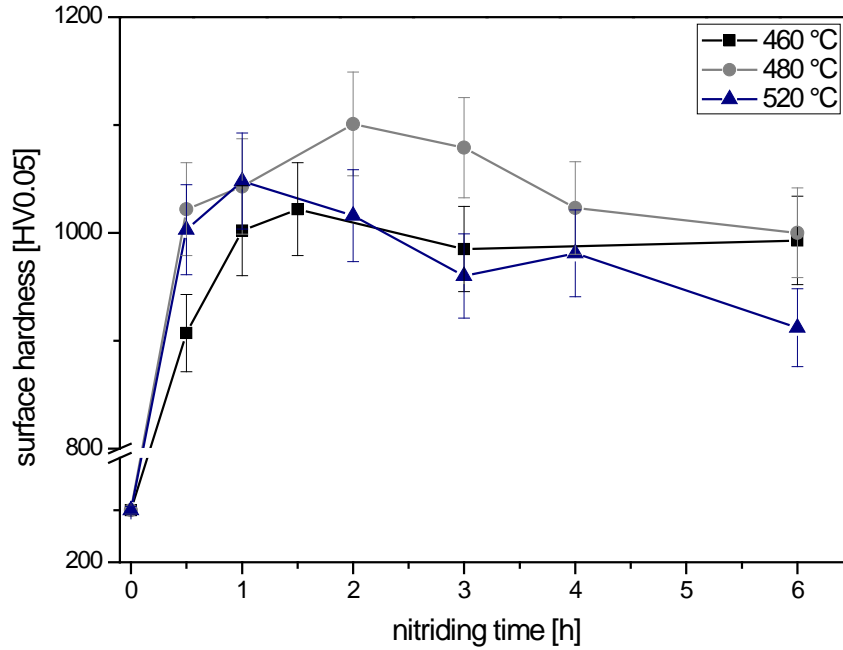


Fig. 5.4: Surface hardness as function of nitriding time for the specimens (type “A”) nitrided at different temperatures (460 °C, 480 °C and 520 °C) employing a nitriding potential of $0.5 \text{ atm}^{-1/2}$. Hardness values indicated at 0 h of nitriding correspond to the hardness of the unnitrided specimen.

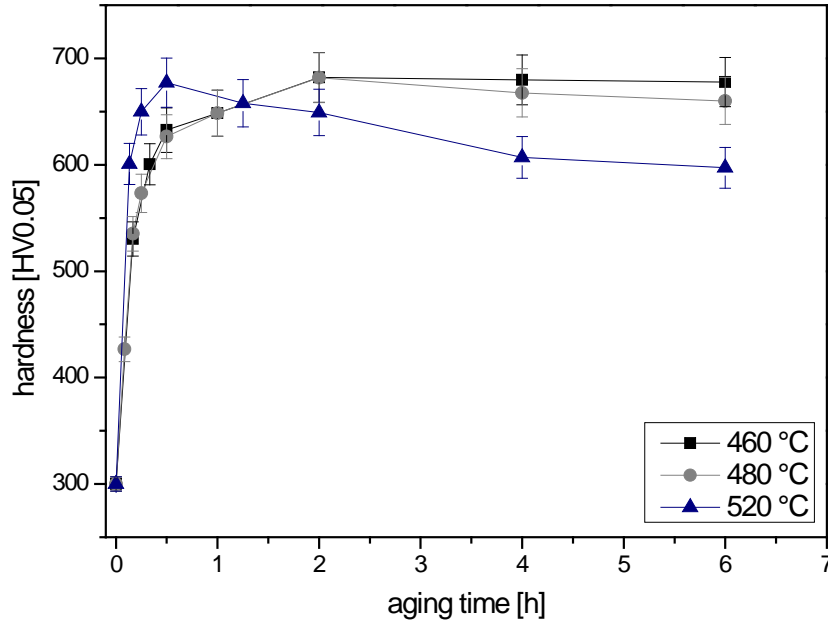


Fig. 5.5: Hardness as function of aging time at aging temperatures of 460 °C, 480 °C and 520 °C. Hardness values indicated at 0 h correspond to the hardness in the soft condition (i.e. after solution annealing).

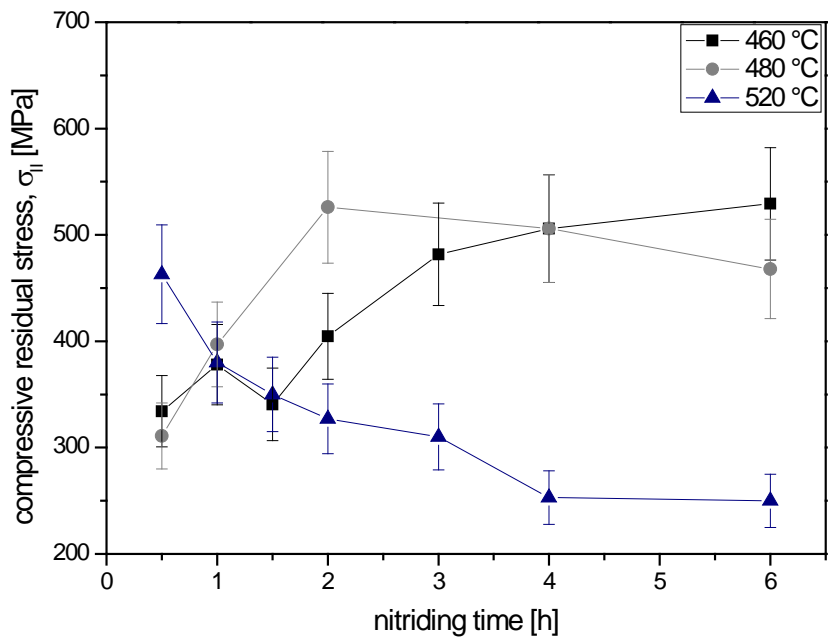


Fig. 5.6: Compressive residual stress at and parallel to the surface, $\sigma_{||}$, as function of nitriding time for specimens (type “A”) nitrided at different temperatures (460 °C, 480 °C, 520 °C) employing a nitriding potential of $0.5 \text{ atm}^{-1/2}$.

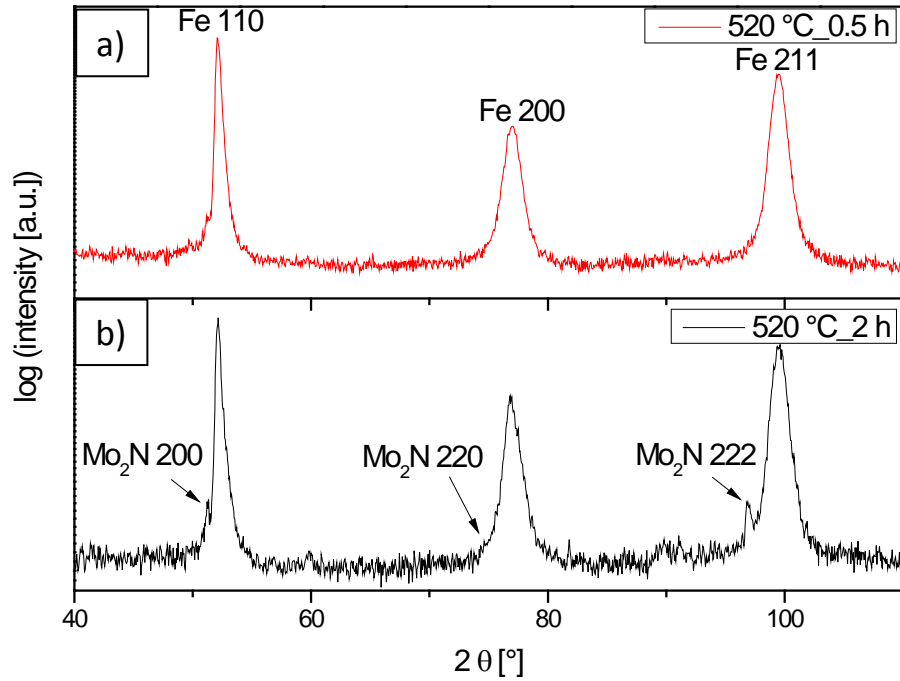


Fig. 5.7: X-ray diffraction patterns recorded from the surface of specimens (type “A”) nitrided at the temperature of 520 °C with a nitriding potential of $0.5 \text{ atm}^{-1/2}$. (a). After 0.5 h of nitriding; only broadened matrix reflections occur; (b) after 2 h of nitriding; additional reflections originating from Mo₂N emerge.

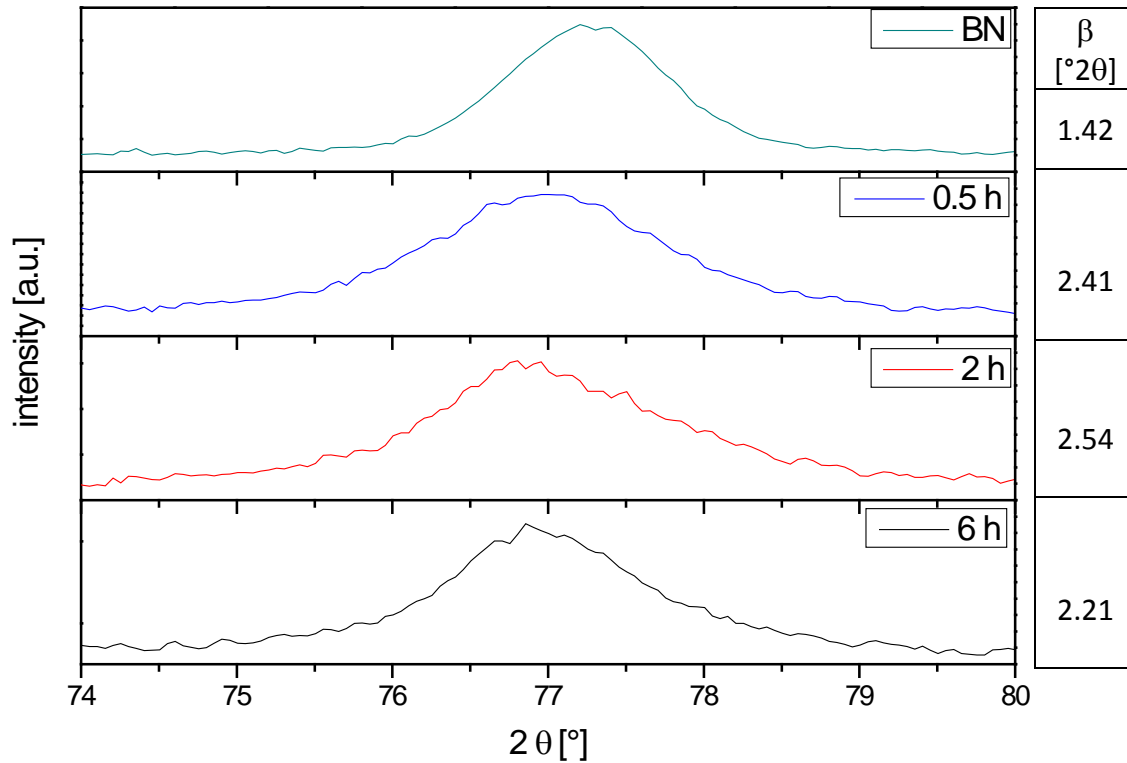


Fig. 5.8: The 200 α -Fe reflection of specimens (type “A”) before nitriding (BN) and after nitriding for 0.5 h, 2 h and 6 h, respectively, at the temperature of 520 °C with a nitriding potential of 0.5 atm^{-1/2}. Extensive (asymmetric) broadening is indicated by the integral breadth, β , indicated at the right side of the figure, strongly increasing until 2 h of nitriding at the temperature of 520 °C, followed by a decrease upon further increase in nitriding time.

5.4.2.2 Nitriding kinetics

The time and temperature dependent development of the nitrogen concentration-depth profile has been determined by GDOES (cf. section 5.3.4.4). Numerical fitting of the model described in section 5.2 to these data led to results as shown in Fig. 5.9 and Table 5.4. The fitting parameters are: (i) the diffusion coefficient D_N , (ii) the solubility product K_{MeN_n} , (iii) the composition parameter b and (iv) the surface concentration of dissolved nitrogen C_N^S . Starting values for the fitting parameters were obtained as described in section 5.2. The starting values for the fitting parameters b and C_N^S , as

obtained from the absorption isotherm, were $b = 0.6$ and $C_N^S = 0.52$ at.% (see sec. 5.4.1). Comparing these values with the final values obtained by fitting, it strikes that the fitted value for b is significantly larger than that determined from the absorption isotherm (0.6 vs. 0.8). This could be explained with smaller nitride precipitates developing in the beginning of nitriding of the specimens pertaining to Fig. 5.9, whereas the specimen used for the determination of the nitrogen-absorption isotherm was prenitrided for a long time (110 h at 480 °C) which can bring about some coarsening; the larger the interfacial area the higher the amount of immobile, adsorbed (at the interfaces between nitride particle and matrix) nitrogen and thus the larger the value of b .

The model was fitted to simultaneously two to three nitrogen concentration-depth profiles, i.e. for two to three different nitriding times for each temperature, with, for each temperature, as fit parameters: constant b , constant D_N^{matrix} and constant K_{MeN_n} and variable C_N^S . Results are shown in Fig. 5.9.

Within experimental accuracy, the model calculated nitrogen concentration-depth profiles fit very well to the experimentally determined ones. The resulting, refined values for (the fit parameters and) the excess N quantities as derived from the refined fit parameters ((i) the difference between c_N^S and $[N]_{\alpha-Fe}^0$, i.e. the mobile excess N, $[N]_{\text{matrix}}^{\text{strain}}$, and (ii) the difference between b and n , i.e. the immobile excess N) have been gathered in Table 5.4. Here, it is assumed that local equilibrium prevails at the surface and that in the surface region all Mo has precipitated as nitride. Indeed, the total surface nitrogen content does not increase after 2 h of nitriding at 460 °C.

The amount of mobile, dissolved excess N, $[N]_{\text{matrix}}^{\text{strain}}$, decreases significantly with increasing nitriding temperature. This can be attributed to the partial loss of coherency (relaxation of misfit strain) of the nitride precipitates by coarsening upon increasing temperature. Evidently, coarsening involves decrease of the amount of nitride/matrix interfacial area and thus also the immobile (adsorbed at the nitride/matrix interface) excess N content is expected to decrease with increasing temperature, as observed (see Table 5.4).

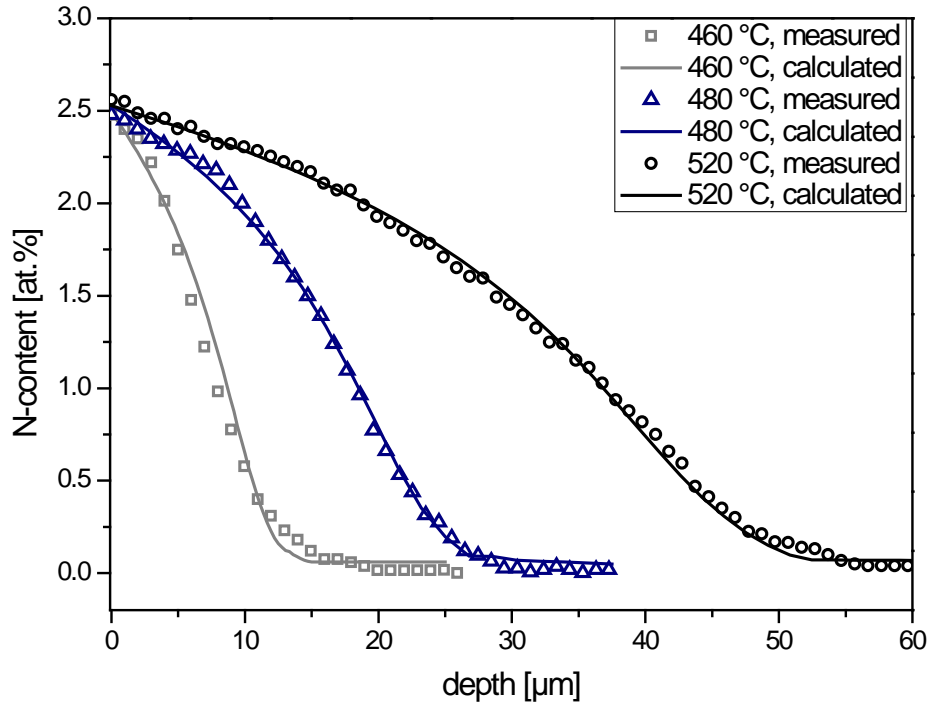


Fig. 5.9: Measured (data points) and model fitted (solid lines) nitrogen concentration-depth profiles for specimens (type “A”) nitrided at the temperature of 460 °C for 4 h (square data points), at the temperature of 480 °C for 6 h (triangular data points) and at the temperature of 520 °C for 6 h (round data points), each with a nitriding potential of $0.5 \text{ atm}^{-1/2}$. The corresponding, refined values of the fit parameters have been given in Table 5.4.

Table 5.4: The refined values of the fit parameters of the model fitted to the measured nitrogen concentration-depth profiles and the excess N quantities derived from these fit parameters, for the specimens (type “A”) nitrided at different temperatures.

tempera- ture [°C]	fitting parameters				$[N]_{\alpha-Fe}^o$ [at.%] ¹	excess nitrogen at the surface		
	C_N^S [at.%]	b	K_{MeN_n} [(atoms) ^{3/2} . nm ^{-9/2}]	D_N^{matrix} [m ² s ⁻¹]		$[N]^{interface}$ [at.%]	$[N]_{matrix}^{strain}$ [at.%]	total [at.%]
460	0.56	0.82	0.1011	$1.4 \cdot 10^{-14}$	0.14	1.05	0.42	1.47
480	0.54	0.80	0.0934	$4.0 \cdot 10^{-14}$	0.17	0.98	0.37	1.35
520	0.52	0.78	0.0895	$15.5 \cdot 10^{-14}$	0.26	0.92	0.26	1.18

¹ the maximum solubility of nitrogen in ferrite, $[N]_{\alpha-Fe}^o$, at the corresponding nitriding temperature, as calculated from data in Ref. [9].

The values found for the (effective) diffusion coefficient of nitrogen in the maraging steel matrix are much lower than those for the diffusion of nitrogen in a pure α -Fe (ferrite) matrix [74]. This effect may be discussed as follows:

- (i) The presence of nitride particles and intermetallic phase particles could act as obstacles for nitrogen diffusion (“labyrinth-effect” [105]). This effective decrease of the diffusion coefficient will be more pronounced at a lower nitriding temperature due to the generally smaller size of the nitride precipitate particles and the corresponding more homogeneous distribution of precipitate phase.
- (ii) A successive “trapping, de-trapping and re-trapping” effect of nitrogen in Fe-Me-N configurations could occur (i.e. without that direct formation of MeN_n nitride takes place), especially in the case/core transition zone where not all Mo has already precipitated as nitride. This effect, as described in Ref. [24,

106], leads to an effective reduction of the diffusion coefficient as nitrogen is temporarily immobilised.

5.4.3 Nitriding of age-hardened maraging steel (specimens “B”)

5.4.3.1 Microstructure

Specimens of type “B” were age hardened (to maximum hardness; see Fig. 5.5) for 2 h at 480 °C prior to nitriding. Thus, no further increase in precipitated volume fraction of intermetallic phases is expected to occur.

Cross sections of maraging steel specimens nitrided for 7 h and 17 h, respectively, with a nitriding potential of $0.5 \text{ atm}^{-1/2}$ at 440 °C are shown in Figs. 5.10a and b. The typical plate-like microstructure of maraging steels [35, 95] can be seen in the unnitrided core. The diffusion zone adjacent to the surface (the extent of the diffusion zone has been indicated with a black dashed line in the figures) shows an etching contrast different from the unnitrided core. No hints of austenite can be seen in the micrographs, which is compatible with the XRD phase analysis discussed below (see Fig. 5.13).

In the light optical micrographs (Figs. 5.10a and b) no difference in the microstructure of the unnitrided core of the age hardened specimen can be observed as compared to that of the only solution annealed specimen (Figs. 5.3a and b).

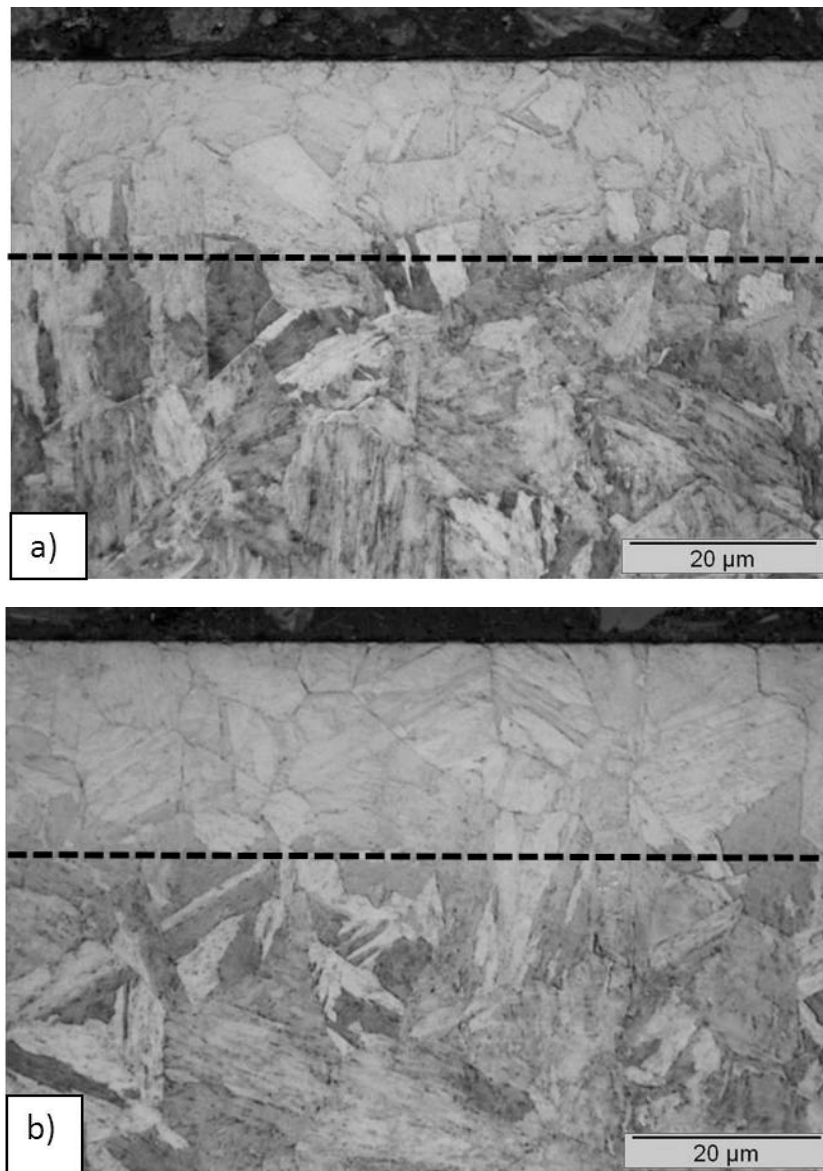


Fig. 5.10: LM-micrographs of specimens (type “B”) after a nitriding time of (a) 7 h and (b) 17 h, at the temperature of 440 °C and $r_N = 0.5 \text{ atm}^{-1/2}$. The extent of the nitrided zone has been marked with a dashed line.

Due to the preceding age-hardening treatment no (further) precipitation of intermetallic compound is expected upon nitriding. The precipitation of nitrides upon nitriding at 440 °C is strongly time-dependent, as indicated by the continuous increase in surface hardness and in compressive residual surface stress (Figs. 5.11 and 5.12). The maximum surface hardness (950 HV) is reached after a nitriding time of 17 h. Similar to

the specimens nitrided in the solution annealed condition (cf. Fig. 5.4), prolonged nitriding leads to decrease of the surface hardness due to nitride-particle coarsening and coherency loss (Fig. 5.11; cf. section 5.4.2.1). The acceleration observed in hardness increase and surface stress increase after the first few hours of nitriding at 440 °C suggests that then distinct nitride precipitation takes place. The (initial) dissolution of nitrogen in a ferrite matrix already leads to an increase in hardness of about 100 HV by solid solution strengthening [81] and also leads to the development of moderate compressive residual stresses in the surface region [107].

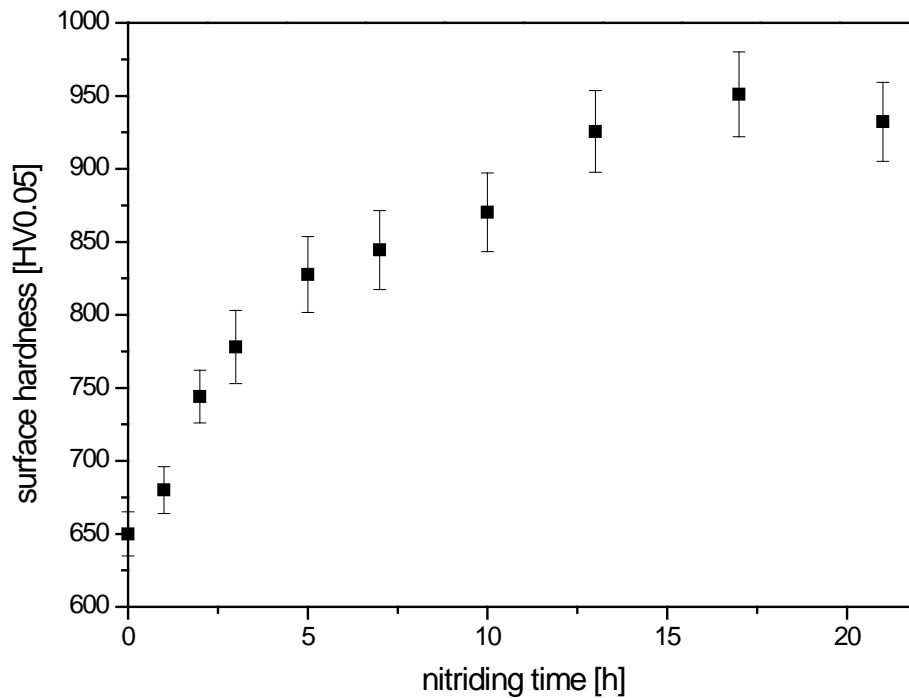


Fig. 5.11: Surface microhardness as function of nitriding time for specimens (type “B”) nitrided at the temperature of 440 °C employing a nitriding potential of $0.5 \text{ atm}^{-1/2}$.

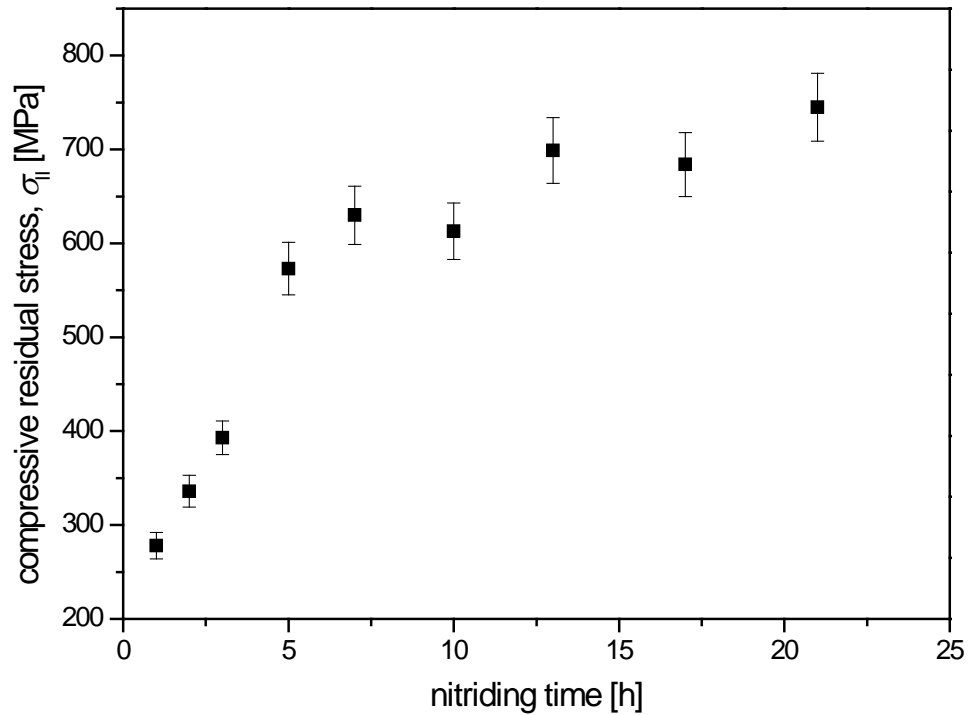


Fig. 5.12: Compressive residual stress at and parallel to the surface, σ_{\parallel} , as function of nitriding time for specimens (type “B”) nitrided at the temperature of 440 °C employing a nitriding potential of $0.5 \text{ atm}^{-1/2}$.

In the X-ray diffraction patterns recorded before and after nitriding from the surface of the specimens (see Fig. 5.13) reflections originating from the cubic martensitic matrix can be seen. No indications for austenite or separate (nitride) reflections (reflections from the cubic Mo_2N -type nitride precipitates, which occur very close to the cubic martensite reflections (see Fig. 5.7b: Mo_2N reflections occur at low-angle side of the ferrite reflections)) are detected. The presence of intermetallic precipitates is not revealed by separate reflections in the X-ray diffraction patterns likely due to the coherent nature of these precipitates [35, 36].

Because the nitride forming element, Mo, is incorporated in intermetallic precipitates at the beginning of the nitriding of the age hardened specimens ("B"), the formation of nitride precipitates requires more time (at the same nitriding temperature) than in case of nitriding the solution annealed specimens ("A") which obstructs identification of separate nitride reflections in the X-ray diffraction patterns in an early stage of nitriding (cf. Fig. 5.13); an intensity hump at the lower 2θ side of the ferrite reflections hints at the presence of reflections from Mo_2N -type precipitates (see arrows after a nitriding time of 21 h in Fig. 5.13).

Upon nitriding strong broadening of the matrix reflections occurs, indicated by increasing values of the integral breadth, β , as shown in Fig. 5.14 (note that the value of β for the unnitrided specimens "B" is smaller than for unnitrided specimens "A" ($1.14^\circ 2\theta$ vs. $1.42^\circ 2\theta$, cf. Figs. 5.14 and 5.8): the age hardening applied for specimens "B" leads to pronounced reduction of the crystal imperfection inherent to the cubic martensite microstructure resulting by quenching after the solution annealing. This broadening is, especially in the early stages of nitriding, accompanied with a strong asymmetry of the 200 reflection, (see Fig. 5.14), which hints at the precipitation of submicroscopical Mo_2N -type nitrides, diffracting coherently with the matrix, as observed upon nitriding of binary Fe-Mo alloy [65] and as discussed for the nitrated solution annealed specimens in section 5.4.2.1.

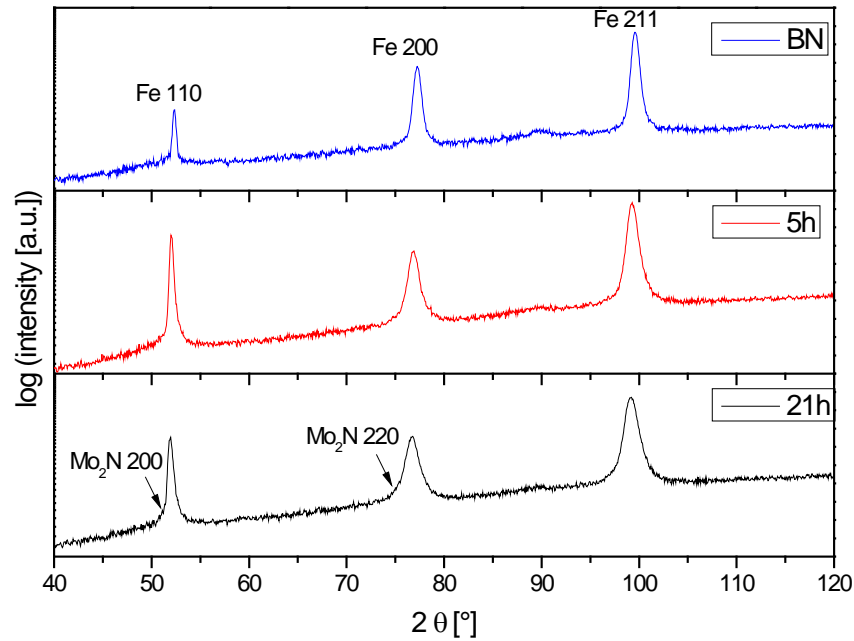


Fig. 5.13: X-ray diffraction patterns of specimens (type “B”) after precipitation hardening before nitriding (BN) and after nitriding for 5 h and 21 h, respectively, at the temperature of 440 °C and a nitriding potential of $0.5 \text{ atm}^{-1/2}$. Reflections originating from the cubic martensitic matrix (denoted as “Fe”) can be discerned. Weak intensity humps at the low-angle side of these reflections hint at the presence of weak, overlapping reflections from Mo_2N -type precipitates (indicated with arrows), especially after a nitriding time of 21 h.

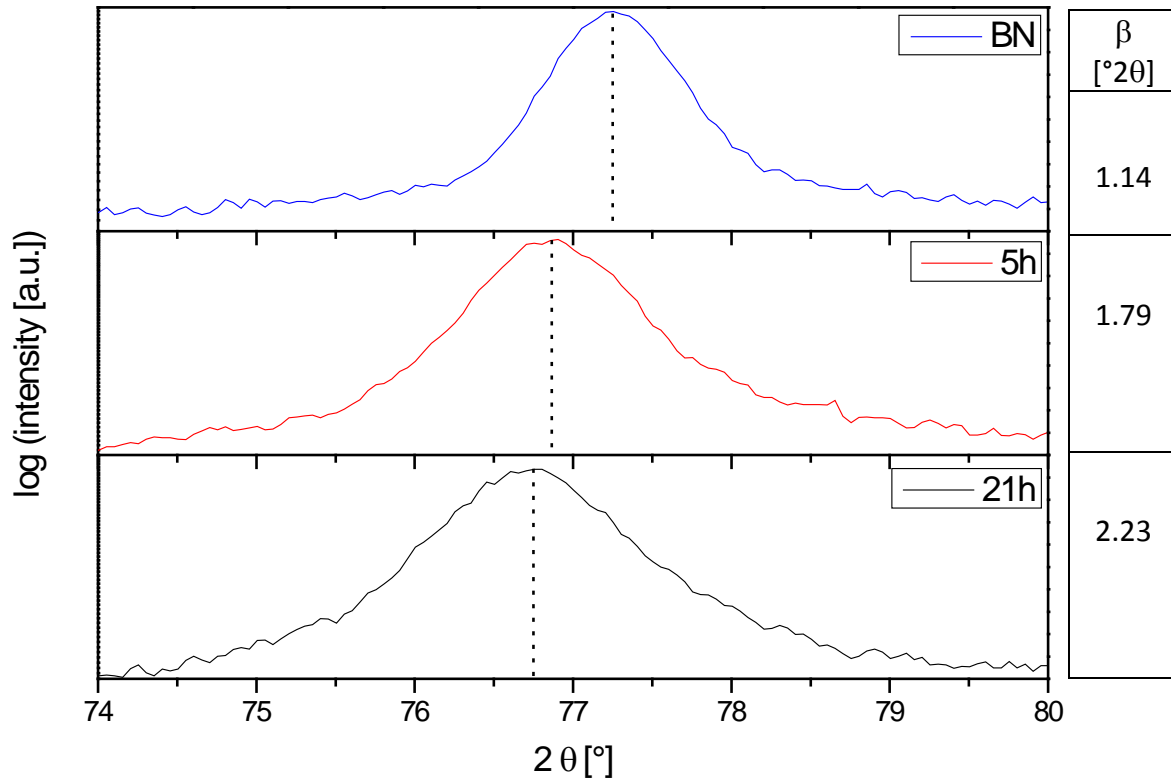


Fig. 5.14: The 200 α -Fe reflection of specimens (type “B”) before nitriding (BN) and after nitriding for 5 h and 21 h, respectively, at the temperature of 440 °C with a nitriding potential of 0.5 atm^{-1/2}. Extensive (asymmetric) broadening is revealed by the integral breadth, β , indicated at the right side of the figure, strongly increasing with increasing nitriding time.

5.4.3.2 Nitriding kinetics

The time and temperature dependent development of the nitrogen concentration-depth profile has been determined by GDOES (cf. section 5.3.4.4). In contrast with specimens “A”, the total amount of nitrogen in the surface region increases with increasing nitriding time (cf. Figs. 5.9 and 5.15). This can be ascribed to the finite time needed to establish a local equilibrium/steady state at the surface between the gas atmosphere and the specimen. This effect can be more pronounced at the low nitriding temperature of 440 °C, pertaining to specimens “B”, than at the higher nitriding temperatures (460 °C – 520 °C) employed for specimens “A” [73, 108]. Moreover, the

much slower precipitation of Mo-nitride in case of specimens “B” (where Mo initially is incorporated in intermetallic particles after the age hardening) can contribute to a more gradual increase of the total nitrogen concentration at the surface.

Numerical fitting of the model described in section 5.2 to these data led to results as shown in Fig. 5.15. Starting values for the fitting parameters were obtained as follows. From the absorption-isotherm measurements (see sec. 5.4.1): b (0.63) and C_N^S (for the longest nitriding time: 0.40 at.%; for the shorter nitriding time the solubility of pure, unstrained ferrite (0.14 at.% as given in Ref. [9]). The starting value for the diffusion coefficient of nitrogen was obtained by fitting the crude model according to Eq. (5.1) to the experimentally obtained data (diffusion layer thickness as function of nitriding time). As initial value for the solubility product, thermodynamic data for the Gibbs energy of formation of Mo_2N from [109] were taken to estimate the solubility product according to [101]. The solubility product, the composition parameter b and the diffusion coefficient should, at constant temperature, not depend on nitriding time. Therefore, the model was fitted to simultaneously the three nitrogen concentration-depth profiles shown in Fig. 5.15 with as fit parameters: constant b , constant D_N^{matrix} and constant K_{MeN_n} and variable C_N^S (one for each nitriding time). The resulting values for the fit parameters have been gathered in Table 5.5. Within experimental accuracy, the fitted nitrogen concentration-depth profiles agree well with the experimentally determined nitrogen concentration-depth profiles.

After the shortest nitriding time of 3 h (Fig. 5.15), the corresponding equilibrium solubility of nitrogen in an unstrained ferrite matrix (corresponding to 0.14 at.% for these nitriding conditions, [9]) has already been surpassed but the equilibrium solubility of nitrogen in maraging steel, as determined from the absorption isotherm (0.40 at.%, cf. section 5.4.1), has not been attained yet. This equilibrium level of (dissolved and also total amount of) nitrogen for this particular temperature is reached at the surface of the specimen after a nitriding time of 17 h (see also hardness data in Fig. 5.11). Hence, for this nitriding time, the values for C_N^S and b can be utilized to calculate the amounts of

mobile and immobile excess nitrogen (see also Table 5.5). The result implies a large amount of mobile excess nitrogen (0.26 at.%; cf. section 5.4.1), dissolved in the strained matrix. The occurrence of *immobile* excess nitrogen (i.e. nitrogen adsorbed at the precipitate/matrix interface) is confirmed by the composition parameter b , which is noticeably larger than 1/2. Comparing the composition parameter, b , of specimens “A” with specimens “B”, it follows that the amount of immobile excess nitrogen is much higher in case of nitriding solution annealed specimens (“A”), suggesting that, upon nitriding specimens “A”, smaller, coherent nitride precipitates develop giving rise to a higher amount of interfacially adsorbed nitrogen. This statement is also supported by the higher hardness values reached after nitriding of specimens “A” as compared to specimens “B” (compare Figs. 5.4 and Fig. 5.11).

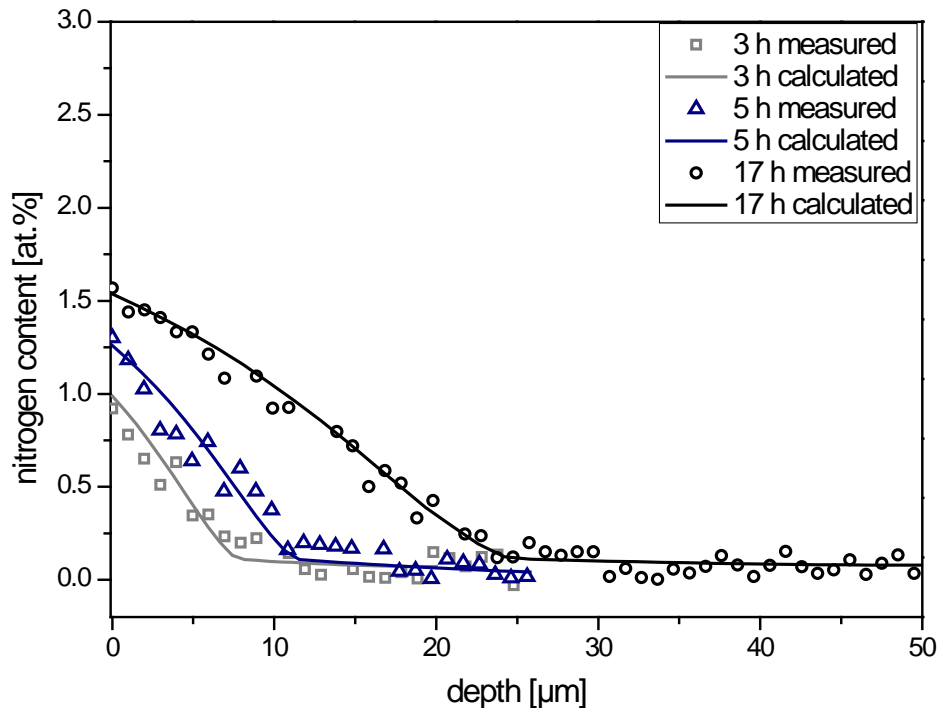


Fig. 5.15: Measured and model fitted (solid line) nitrogen concentration-depth profiles for the specimen (type “B”) nitrided at the temperature of 440 °C for 3 h (square data points), for 5 h (triangle data points) and for 17 h (round data points), each with a nitriding potential of 0.5 atm^{-1/2}. The corresponding refined values of the fit parameters are given in Table 5.5.

Table 5.5: The refined values of the fit parameters of the model fitted to the measured nitrogen concentration-depth profiles and the excess N quantities derived from these fit parameters, for the specimens (type “B”) nitrided at the temperature of 440 °C for different times.

nitriding time [h]	fitting parameters				$[N]_{\alpha-Fe}^o$ [at.%] ¹	excess nitrogen at the surface		
	C_N^S [at.%]	b	K_{MeN_n} [(atoms) ^{3/2} . nm ^{-9/2}]	D_N^{matrix} [m ² s ⁻¹]		$[N]^{interface}$ [at.%]	mobile [at.%]	total [at.%]
3	0.23	0.63	0.35	$1.18 \cdot 10^{-14}$	0.14	-	-	-
5	0.3	0.63	0.35	$1.18 \cdot 10^{-14}$	0.14	-	-	-
17	0.4	0.63	0.35	$1.18 \cdot 10^{-14}$	0.14	0.45	0.26	0.71

¹ the maximum solubility of nitrogen in ferrite, $[N]_{\alpha-Fe}^o$, at the corresponding nitriding temperature, as calculated from data in Ref. [9].

5.5 Final remarks on the difference in nitriding response of solution annealed (“A”) and age-hardened (“B”) specimens

It has to be recognized that in age hardened specimens (“B”), prior to nitriding, all Mo has precipitated as intermetallic compound (age hardening conditions prior to nitriding had been chosen such that maximum hardness achievable by aging was reached [35, 36]), whereas in the solution annealed specimens all Mo is dissolved in the cubic, martensite matrix. This results in a higher hardness before nitriding for the age hardened specimens (650 HV0.05 vs. 300 HV0.05; cf. Figs. 5.4 and 5.11).

As consequence, upon nitriding the solution annealed specimens (“A”) and as compared to the age hardened specimens (“B”) (i) a larger hardness increase and a higher hardness are obtained for specimens “A” upon nitriding and (ii) higher amounts of excess nitrogen (both mobile and immobile) occur for specimens “A” (cf. Table 5.5 and Table 5.4). This can be discussed as follows. Upon nitriding specimens “A” a higher amount of Mo nitride can precipitate in the early stage of nitriding as all Mo is initially dissolved in the matrix. Even after nitrogen saturation has been realized at the surface for specimens “B” (likely after about 17 h at 440 °C; see Fig. 5.11), this maximum hardness is lower than the maximum hardness for specimens “A” (see Fig. 5.4). This indicates that the nitride precipitates in specimens “A” are smaller and likely largely coherent with the matrix (cf. section 5.4.2.1).

5.6 Conclusions

The nitriding behaviour of Mo-containing maraging steel can be summarized as follows:

- Upon nitriding, largely coherent Mo₂N-type nitrides develop, surrounded by a tetragonally distorted matrix. These nitrides cause a strong increase in hardness.
- The development of the nitrogen concentration-depth profiles in maraging steel upon nitriding can be successfully modelled with a combined diffusion and precipitation kinetic model, provided that the role of excess nitrogen is recognized. The model employs the following fit parameters: the composition parameter of the nitride (expressing the presence of immobile, i.e. adsorbed excess nitrogen at the nitride/matrix interface), the solubility of nitrogen in the matrix (recognizing the presence of mobile, i.e. additionally in the strained matrix, dissolved excess nitrogen), the diffusion coefficient of nitrogen in the matrix and the solubility product of the nitride precipitates.
- Nitrogen-absorption isotherms determined for the maraging steel allowed distinction of the different kinds of (excess-) nitrogen taken up and thus provided starting values of the fitting parameters for the kinetic model.
- The diffusion coefficient of nitrogen in the maraging steel matrix is much lower than for nitrogen diffusion in pure ferrite. This may be ascribed to the microstructure of the maraging steel (trapping, de-trapping and re-trapping of nitrogen at e.g. lattice defects) and the occurrence of a labyrinth-effect due to precipitated particles.
- Nitriding kinetics are faster in the only solution annealed specimens in association with rapid saturation of the total amount of nitrogen in the surface region. In case of the age hardened specimens a more gradually preceding nitriding reaction takes place due to the necessary preceding dissolution of the intermetallic compound particles in favour of the developing nitride particles.
- The amounts of (mobile and immobile) excess nitrogen taken up are much larger in case of the solution annealed specimens indicating the occurrence of finer and more coherent nitride platelets, than in case of the age hardened specimens.

- In view of technological application, nitriding of maraging steels can best be applied without application of a prior age hardening treatment: distinctly more nitrogen is taken up more rapidly and a higher hardness is obtained.

5.7 Acknowledgement

We are grateful to Dr. K.S. Jung and Dipl.-Ing. B. Rheingans for helpful discussions and to Dipl.-Ing. P. Kress (all with the Max Planck Institute for Intelligent Systems) for assistance with the nitriding experiments.

CHAPTER 6

Summary

6.1 Introduction

Gaseous nitriding is a very powerful tool to improve the surface mechanical (fatigue and wear) and chemical (corrosion resistance) properties of iron-based workpieces and steels. Among the technologically important thermochemical surface heat treatments, such as carburizing, nitrocarburizing and nitriding, which can be carried out in liquid (salt bath), plasma or gaseous environments, gas nitriding is the most often applied treatment because of its unique controllability. The desired microstructure and therefore the resulting surface properties of a material can be precisely set and controlled upon gaseous nitriding.

Gas nitriding is usually carried out at temperatures ranging from 400 – 580 °C in ammonia/hydrogen gas mixtures. At these temperatures, ammonia dissociates catalytically at the surface of the workpiece and atomic nitrogen diffuses into the surface of the ferrite matrix. Depending on the nitriding conditions, such as temperature and nitriding potential r_N , which is defined as the ratio of the partial pressures of

ammonia and hydrogen $\left(r_N = \frac{p(\text{NH}_3)}{p(\text{H}_2)^{3/2}} \right)$, different phases can be formed at the surface

of the workpiece, according to the Fe-N phase diagram: α -Fe (with nitrogen dissolved in the octahedral interstices of the matrix), and the iron nitrides γ' -Fe₄N_{1-x} and ϵ -Fe₃N_{1+y} (in this order with increasing nitrogen content). The formation of iron nitrides at the surface leads to the development of a so-called compound layer which largely influences the resistance to wear and corrosion. Beneath the compound layer, nitride forming alloying elements can precipitate as nitrides in the so-called diffusion zone, which has a strong influence on the fatigue behaviour.

Despite its wide adoption in industry, fundamental research about the nitriding process is still needed as the application of this technique in industry is often based on phenomenology and experience.

Fundamental investigations have been carried out extensively for binary iron-based alloys containing relatively strong nitride formers such as Ti and V. However, there is still a great scientific and industrial interest in gaining detailed understanding of nitriding binary iron-based alloys, especially for relatively weak nitride formers (such as Mo, W, Si), as these systems are not very well understood. The literature results, if at all available, often contradict each other, especially in case of molybdenum.

The present thesis focuses on the nitriding behaviour of binary Mo-containing iron-based alloys and, with the thus gained insight, on the nitriding behaviour of a Mo-containing maraging steel.

6.2 Experimental

The Fe-Mo alloys were prepared by melting appropriate amounts of pure Fe and Mo in a protective argon gas atmosphere in an inductive furnace. The melts were cast in a copper mould to obtain cylindrical rods (\varnothing : 10 mm, l : 100 mm). The chemical composition and the amount of impurities were determined by chemical analysis (inductively coupled plasma - optical emission spectroscopy (for Mo); combustion method (for C and S) and carrier gas hot extraction (for O and N)). The ingots were cold rolled to sheets, out of which rectangular specimen were cut. These specimens were then mechanically ground and polished (last polishing step: 1 μ m diamond suspension). The polished specimen were encapsulated in a quartz tube filled with argon and then subsequently heat treated at 800 °C for 1.5 h in a muffle furnace to achieve recrystallization of the cold deformed microstructure.

The commercially available maraging steel sheet was supplied by Imphy alloys, Arcelor Group, France. Out of these sheets, rectangular specimens were cut and prepared in the same way as the binary Fe-Mo specimens. After polishing, the specimens were solution annealed at 880 °C for 0.5 h.

Before nitriding, the specimen were polished (final step: 1 μm diamond suspension) and cleaned ultrasonically with ethanol.

6.3 Nitriding

Nitriding was performed in a multizone quartz-tube furnace with an ammonia/hydrogen gas mixture at different temperatures from 440 °C to 580 °C (constancy of temperature: ± 1 °C). The gas fluxes were adjusted by mass-flow controllers and the total gas flow (500 ml/min) was set such that the linear gas flow was sufficient to avoid any significant thermal decomposition of ammonia in the nitriding atmosphere.

6.4 Specimen characterization

For light microscopic investigations, cross-sections were prepared (ground and polished) and etched with Nital (2 vol.-%).

Microhardness measurements on polished (uneched) cross-sections were carried out before and after nitriding employing a Vickers microhardness tester.

Phase analysis by means of X-ray diffraction was performed for all specimens before and after nitriding. Identification of the detected phases was conducted by comparing the 2θ peak positions of the phases with reference data.

To determine the residual stresses, the conventional $\sin^2\psi$ -method was applied. In case of specimens exhibiting a remaining fibre-texture after recrystallization, the crystallite group method was applied for the determination of the residual stress.

The structure and morphology of the nitride precipitates were investigated by transmission electron microscopy (TEM). TEM specimens were prepared at selected depths of the nitrided zone by grinding mechanically, dimpling and Ar-ion milling. Bright field image (BF), dark field image (DF) and selected area diffraction patterns (SADPs) were taken to determine the crystal structure and morphology of the formed nitride precipitates.

Elemental concentration-depth profiles were revealed by electron probe microanalysis (EPMA) performed on polished cross-sections perpendicular to the surface, or by glow discharge optical emission spectroscopy (GDOES).

For quantitative analysis of excess nitrogen uptake (i.e. nitrogen adsorbed at the precipitate/matrix interface and additionally dissolved in the strained matrix due to alloying element nitride precipitation), nitrogen absorption isotherms were determined. To this end, thin foils were homogeneously through nitrated and subsequently denitrated. The nitrogen uptake at constant temperature applying different nitriding potentials was followed by weight gain measurements.

6.5 Results

6.5.1 Molybdenum-nitride precipitation in recrystallized and cold rolled Fe-1at.% Mo alloy

Upon nitriding Fe-1at.% Mo alloy under conditions such that no compound layer can be formed at the surface, cubic Mo₂N-type precipitates develop as platelets of several hundreds of nm length and thickness of a few atomic layers occurs according to a Bain-type orientation relationship. In case of the recrystallized specimens the platelets are largely coherent (diffracting coherently with the matrix) giving rise to strongly asymmetric ferrite-matrix diffraction peaks. In case of the cold rolled specimens development of the Mo₂N-type precipitation occurs much earlier and the nitride platelets are at least partially incoherent (giving rise to separate nitride reflections in the diffraction patterns). Upon prolonged treatment a discontinuous precipitation reaction initiating at ferrite-matrix grain boundaries takes place replacing the submicroscopical Mo₂N-type platelets by a lamellar α -Fe/MoN (hexagonal crystal structure) microstructure with a Burgers-type orientation relationship, involving parallelism of close packed planes in both phases. In case of the recrystallized specimens the discontinuous precipitation reaction eventually brings about a full transformation of Mo₂N-type precipitates to MoN-type precipitates. In case of the cold rolled specimens

the $\text{Mo}_2\text{N} \rightarrow \text{MoN}$ transformation occurs only partially: the driving force for the discontinuous precipitation reaction is much smaller in case of the cold rolled specimen (much less (misfit-) strain energy and nitrogen supersaturation).

The discontinuous transformation leads to a pronounced increase in the nitrogen concentration upon transformation due to the change in stoichiometry ($\text{Mo}_2\text{N} \rightarrow \text{MoN}$). The composition analysis of the Mo_2N -type nitrides (submicroscopical) and of the MoN -type nitrides (lamellae) suggests no incorporation of significant amounts of Fe in the nitrides.

6.5.2 Defect-dependent nitride surface-layer development upon nitriding of Fe-1at.% Mo alloys

The defect density of iron-based Fe-Me alloy, with Me as an (effectively) weak nitride former (e.g. Me = Mo), has a dramatic effect on the constitution and morphology of the iron-nitride based compound layer developing upon nitriding. This is described in the following.

Upon nitriding *cold rolled* Fe-1at.%Mo alloy *immediate* precipitation of Mo_2N (dislocation facilitated nucleation) occurs, leading to a low nitrogen supersaturation of the ferrite matrix. γ' nucleates (only) at the surface resulting in the development of a compact layer of γ' , incorporating (by overrunning the formed) Mo_2N particles. The γ' layer growth can be described by a modified parabolic growth law, accounting for the initial delay in the nucleation of γ' . Growth of the nitride layer is rate controlled by diffusion of nitrogen through the layer.

Upon nitriding *recrystallized* Fe-1at.%Mo alloy (strongly) *delayed* precipitation of Mo_2N occurs (if at all): no Mo_2N can be found in the matrix even after 64 h of nitriding at 480 °C. This is a consequence of the high volumetric misfit between the ferrite matrix and the Mo_2N nitride. Because the solubility of Mo in γ' is low, γ' nitride cannot precipitate easily. These obstacles for Mo-nitride and γ' -nitride precipitation lead to a high nitrogen supersaturation of the ferrite matrix over an extended depth range.

Eventually, the chosen route for elimination of this high nitrogen supersaturation is precipitation of γ' at the cost of dissolution of Mo in γ' (under para-equilibrium conditions). Plates of γ' nitride, once nucleated, grow rapidly across the extended depth range of high nitrogen supersaturation. The relatively high growth rate of these plates is at least partly due to short-circuit diffusion of nitrogen through ferrite grains adjacent to the surface (no compact γ' layer occurs). The γ' plates exhibit a Nishiyama-Wassermann orientation relationship with the ferrite matrix. The equilibrium solubility of Mo in γ' nitride is low. This leads to the emergence of ε phase and a hitherto unknown (precursory) Mo-nitride phase, next to γ' phase in the compound layer, upon nitriding the recrystallized Fe-Mo specimens, and also the cold rolled specimens in a beginning stage of nitriding. Upon continued nitriding the ε phase and the unknown (precursory) Mo-nitride phase in the surface adjacent part of the compound layer dissolve and equilibrium Mo-nitride phases emerge.

6.5.3 Microstructural and surface residual stress development during low-temperature gaseous nitriding of Fe-3.07at.% Mo alloy

Upon low-temperature nitriding of Fe-3.07at.% Mo alloy, precipitation of nano-sized platelets along $\{100\}$ planes of the ferrite matrix occurs. Strongly asymmetric X-ray diffraction ferrite-peak broadening and streaks along $\langle 100 \rangle$ ferrite directions in the selected area electron diffraction pattern suggest that the nitride precipitates are largely coherent with the surrounding ferrite matrix, which is distorted tetragonally due to the precipitate/matrix misfit. The precipitation process is not instantaneous upon nitrogen saturation of the ferrite matrix: a gradual development of high hardness and high compressive residual stress occurs.

Adopting the composition Mo_2N for the largely coherent nitride platelets, it follows that a distinct amount of “excess nitrogen” is taken up.

6.5.4 Nitriding behaviour of maraging steel: experiment and modelling

Upon nitriding of maraging steel, largely coherent Mo_2N -type nitrides develop, surrounded by a tetragonally distorted matrix. These nitrides cause a strong increase in hardness and compressive residual stress. In case of age hardening the specimens prior to nitriding, all Mo has precipitated as intermetallic compound, whereas in the solution annealed specimens all Mo is dissolved in the cubic, martensite matrix. This results in hardness which is twice as high as the hardness of the solution annealed specimens before nitriding. As consequence, upon nitriding the solution annealed specimens ("A") and as compared to the age hardened specimens ("B") (i) a larger hardness increase and a higher hardness are obtained for specimens "A" upon nitriding and (ii) higher amounts of excess nitrogen (both mobile and immobile) occur for specimens "A". This can be discussed as follows. Upon nitriding specimens "A" a higher amount of Mo nitride can precipitate in the early stage of nitriding as all Mo is initially dissolved in the matrix.

The development of the nitrogen concentration-depth profiles in maraging steel upon nitriding can be successfully modelled with a combined diffusion and precipitation kinetic model, provided that the role of excess nitrogen is recognized. The model employs the following fit parameters: the composition parameter of the nitride (expressing the presence of immobile, i.e. adsorbed excess nitrogen at the nitride/matrix interface), the solubility of nitrogen in the matrix (recognizing the presence of mobile, i.e. additionally in the strained matrix, dissolved excess nitrogen), the diffusion coefficient of nitrogen in the matrix and the solubility product of the nitride precipitates.

Nitrogen-absorption isotherms determined for the maraging steel allowed distinction of the different kinds of (excess-) nitrogen taken up and thus provided starting values of the fitting parameters for the kinetic model.

The diffusion coefficient of nitrogen in the maraging steel matrix is much lower than for nitrogen diffusion in pure ferrite. This may be ascribed to the microstructure of the maraging steel (trapping, de-trapping and re-trapping of nitrogen at e.g. lattice defects) and the occurrence of a labyrinth-effect due to precipitated particles.

Nitriding kinetics are faster in the only solution annealed specimens in association with rapid saturation of the total amount of nitrogen in the surface region. In case of the age hardened specimens a more gradually preceding nitriding reaction takes place due to the necessary preceding dissolution of the intermetallic compound particles in favour of the developing nitride particles.

The amounts of (mobile and immobile) excess nitrogen taken up are much larger in case of the solution annealed specimens indicating the occurrence of finer and more coherent nitride platelets, than in case of the age hardened specimens.

In view of technological application, nitriding of maraging steels can best be applied without application of a prior age hardening treatment: distinctly more nitrogen is taken up more rapidly and a higher hardness is obtained.

CHAPTER 7

Zusammenfassung

7.1 Einleitung

Das Gasnitrieren ist ein sehr leistungstarkes Verfahren um die Oberflächeneigenschaften (Ermüdung und Abrasion), sowie die chemischen Eigenschaften (Korrosionsbeständigkeit) von eisenbasierten Werkstücken und Stählen zu verbessern. Unter den technologisch bedeutsamen thermochemischen Oberflächenverfahren wie dem Aufkohlen, Nitrocarburieren und Nitrieren, die in flüssigen, plasma- oder gasförmigen Medien durchgeführt werden können, ist das Gasnitrieren aufgrund seiner einzigartigen Kontrollierbarkeit das am weitesten verbreitete Verfahren. Die gewünschte Mikrostruktur und damit einhergehend die resultierenden Oberflächeneigenschaften eines Materials können während des Gasnitrierprozesses präzise eingestellt und kontrolliert werden.

Das Gasnitrieren wird normalerweise bei Temperaturen im Bereich von 400 – 580 °C in Ammoniak/Wasserstoff-Gasmischungen durchgeführt. Bei diesen Temperaturen dissoziiert Ammoniak katalytisch an der Oberfläche des Werkstückes und atomarer Stickstoff diffundiert in die Oberfläche der ferritischen Matrix. In Abhängigkeit von den Nitrierbedingungen wie Temperatur und Nitrierkennzahl k_N , welche definiert ist

als das Verhältnis der Partialdrücke von Ammoniak und Wasserstoff $\left(k_N = \frac{p(\text{NH}_3)}{p(\text{H}_2)^{3/2}} \right)$,

können verschiedene Phasen an der Oberfläche des Werkstückes gebildet werden, gemäß dem Fe-N-Phasendiagramm: α -Fe (mit auf den Oktaederlücken der ferritischen Matrix gelöstem Stickstoff), sowie die Eisennitride γ' -Fe₄N_{1-x} und ϵ -Fe₃N_{1+y} (in dieser Reihenfolge mit zunehmendem Stickstoffgehalt). Die Bildung von Eisennitriden an der Oberfläche führt zur Entstehung einer so genannten Verbindungsschicht, die ihrerseits sehr stark das Verhalten gegenüber abrasivem Verschleiß und Korrosion verbessert.

Trotz der weit verbreiteten industriellen Anwendung besteht ein großer Bedarf an Grundlagenforschung bezüglich des Nitrierprozesses, da die Anwendung dieser Technik in der Industrie oft auf Phänomenologie und Erfahrung beruht.

Umfangreiche Grundlagenuntersuchungen wurden bereits an binären Eisenbasislegierungen mit relativ starken Nitridbildnern wie Ti und V durchgeführt. Gleichwohl besteht weiterhin ein großes wissenschaftliches und industrielles Interesse detailliertes Verständnis bezüglich des Nitrierverhaltens von binären eisenbasierten Legierungen zu erlangen, insbesondere für schwächere Nitridbildner (wie Mo, W, Si), da diese Systeme nicht gut verstanden sind. Die Literaturergebnisse, falls überhaupt verfügbar, widersprechen sich oft gegenseitig, insbesondere im Falle von Mo.

Die vorliegende Arbeit konzentriert sich auf das Nitrierverhalten von solchen Mo-enthaltenden, eisenbasierten Legierungen und, mit den dadurch erlangten Erkenntnissen, auf das Nitrierverhalten von Mo-enthaltenden Maragingstählen.

7.2 Experimententeil

Die Fe-Mo Legierungen wurden durch Einschmelzen entsprechender Mengen an reinem Fe und Mo unter Schutzgasatmosphäre in einem Induktionsofen hergestellt. Die Schmelzen wurden in Kupferkokillen abgegossen, um einen zylindrischen Stab (\emptyset : 10 mm, l : 100 mm) zu erhalten. Die chemische Zusammensetzung und der Gehalt an Verunreinigungen wurde mittels chemischer Analyse bestimmt (induktiv gekoppeltes Plasma – optische Emissionsspektroskopie (für Mo), Verbrennungsmethode (für C und S) und Trägergas-Heißextraktion (für O und N)). Die Abgüsse wurden zu Blechen kaltgewalzt, aus denen dann rechteckige Proben geschnitten wurden. Diese Proben wurden dann mechanisch geschliffen und poliert (abschließende Polierstufe: 1 μ m Diamantsuspension). Die polierten Proben wurden in eine mit Argongas gefüllte Quarzampulle eingekapselt und anschließend bei 800 °C für 1,5 h in einem Muffelofen wärmebehandelt, um die Rekristallisation der verformten Mikrostruktur zu erzielen.

Das kommerziell erhältliche Maraging-Stahl Blech wurde von Imphy alloys, Arcelor Group, Frankreich, bezogen. Aus diesem Blech wurden ebenfalls rechteckige Proben

geschnitten und gleichermaßen präpariert wie die Fe-Mo Proben. Nach dem Polieren wurden die Proben bei 880 °C für 0,5 h Lösungsgeglüht.

Vor dem Nitrieren wurden die Proben poliert (finale Polierstufe: 1 µm Diamantsuspension) und mittels Ethanol im Ultraschallbad gereinigt.

7.3 Nitrieren

Das Nitrieren wurde in einem Mehrzonen-Quartztrofen mittels Ammoniak/Wasserstoff-Gasmischungen bei verschiedenen Temperaturen im Bereich von 440 °C bis 580 °C (Temperaturkonstanz: ± 1 °C) durchgeführt. Die Gasflüsse wurden durch Massflow-Controller geregelt, wobei der gesamte Gasdurchfluss (500 ml/min) so gewählt wurde, dass der erzielte lineare Gasdurchfluss ausreichte, um jegliche signifikante, thermisch bedingte Ammoniakzersetzung in der Nitrieratmosphäre zu vermeiden.

7.4 Probencharakterisierung

Für die lichtmikroskopischen Untersuchungen wurden Querschliffe hergestellt (geschliffen und poliert) und anschließend mit Nital (2 Vol.-%) geätzt.

Mikrohärtemessungen wurden an polierten (ungeätzten) Querschliffen vor und nach dem Nitrieren mittels Vickers Mikrohärteprüfung durchgeführt

Eine Phasenanalyse mithilfe von Röntgendiffraktometrie wurde bei allen Proben vor und nach dem Nitrieren durchgeführt. Die Identifikation der Phasen erfolgte durch Vergleich der 2θ Reflexpositionen der Phasen mit Referenzdaten.

Die Bestimmung der Eigenspannungen erfolgte nach der konventionellen $\sin^2\psi$ -Methode. Für den Fall einer nach der Rekristallisation verbleibenden Fasertextur wurde die Kristallitgruppenmethode zur Bestimmung der Eigenspannungen herangezogen.

Die Struktur und Morphologie der Nitrid-Ausscheidungen wurde mittels Transmissions-Elektronenmikroskopie (TEM) untersucht. TEM-Proben aus definierten Tiefen der nitrierten Zone wurden durch mechanisches Schleifen, Dimpeln und Argon-Ionendünnen hergestellt. Hellfeld-, Dunkelfeldaufnahmen, sowie Beugungsbilder

wurden aufgenommen, um die Kristallstruktur und Morphologie der gebildeten Nitrid-Ausscheidungen zu bestimmen.

Elementspezifische Konzentrations-Tiefenverläufe wurden mithilfe der Elektronenstrahl-Mikroanalyse an polierten Querschliffen senkrecht zur Oberfläche, sowie durch Glimmentladungsspektroskopie, erstellt.

Für die quantitative Analyse der Aufnahme an Überschuss-Stickstoff (an der Grenzfläche zwischen Nitrid-Ausscheidung und Matrix adsorbierter, bzw. zusätzlich in der durch Nitrid-Ausscheidungen gedehnten Matrix gelöster Stickstoff) wurde eine Absorptionsisotherme erstellt. Hierzu wurde eine dünne Folie homogen durchnitriert und anschließend denitriert. Die Stickstoffaufnahme bei konstanter Temperatur und verschiedenen Nitrierkennzahlen wurde gravimetrisch bestimmt.

7.5 Ergebnisse

7.5.1 Molybdänitrid-Ausscheidungen in rekristallisierter und kalt gewalzter Fe-1at.% Mo-Legierung

Beim Nitrieren einer Fe-1at.% Mo-Legierung unter solchen Bedingungen, die keine Verbindungsschichtbildung an der Oberfläche erlauben, entstehen Ausscheidungen vom Typ Mo_2N als Plättchen mit einer Länge von mehreren hundert nm und einer Dicke von nur wenigen Atomlagen gemäß einer Bain-Orientierungsbeziehung zur Matrix. Im Falle rekristallisierter Proben sind die Plättchen in hohem Maße kohärent (beugen kohärent mit der Matrix) und führen daher zu stark asymmetrischen Ferrit-Matrix Beugungsreflexen. Im Falle kaltgewalzter Proben entstehen die Ausscheidungen vom Typ Mo_2N viel früher und die Plättchen sind zumindest teilweise inkohärent (führen daher zu separaten Nitrid-Reflexen im Beugungsbild). Bei längerer Nitrierdauer findet eine diskontinuierliche Ausscheidungsreaktion statt, welche an den Korngrenzen der Ferrit-Matrix startet und die submikroskopischen Plättchen vom Typ Mo_2N durch eine lamellare $\alpha\text{-Fe/MoN}$ (hexagonale Kristallstruktur) Mikrostruktur mit einer Orientierungsbeziehung nach Burgers ersetzen, was eine Parallelität der dichtest

gepackten Ebene in beiden Phasen zur Folge hat. Im Falle rekristallisierter Proben führt die diskontinuierliche Ausscheidung letztlich zu einer vollständigen Umwandlung der Ausscheidungen vom Typ Mo_2N zu MoN . Im Falle kaltgewalzter Proben tritt die $\text{Mo}_2\text{N} \rightarrow \text{MoN}$ -Umwandlung nur partiell auf: die Triebkraft für die diskontinuierliche Ausscheidungsreaktion ist wesentlich kleiner im Falle von kaltgewalzten Proben (wesentlich geringere (Fehlpassungs-) Verformungsenergie und Stickstoff-Übersättigung).

Die diskontinuierliche Umwandlung führt zu einem verstärkten Anstieg der Stickstoff-Konzentration während der Umwandlung aufgrund der Stöchiometrieänderung ($\text{Mo}_2\text{N} \rightarrow \text{MoN}$). Die Zusammensetzungsanalyse der (submikroskopischen) Nitride vom Typ Mo_2N und der (lamellaren) Nitride vom Typ MoN gibt keinen Hinweis auf eine Eisenaufnahme in den Nitriden.

7.5.2 Defekt-abhängige Bildung nitrierter Oberflächenschichten beim Nitrieren von Fe-1at.% Mo Legierungen

Die Defektdichte eisenbasierter Fe-Me-Legierungen, wobei Me ein schwacher Nitridbildner repräsentiert (wie beispielsweise $\text{Me} = \text{Mo}$), hat einen starken Einfluss auf die Konstitution und Morphologie der sich beim Nitrieren bildenden Eisennitrid-basierten Verbindungsschicht. Dies wird im Folgenden verdeutlicht.

Beim Nitrieren einer *kaltgewalzten* Fe-1at.% Mo-Legierung tritt sofortige Ausscheidung von Mo_2N auf (versetzungsbegünstigte Keimbildung), welche zu einer geringen Stickstoffübersättigung der ferritischen Matrix führt. Keimbildung von γ' findet (ausschließlich) an der Oberfläche statt, wodurch sich daraus resultierend eine geschlossene Verbindungsschicht bildet, die Mo_2N Partikel (durch „Überrennung“ der gebildeten Partikel) inkorporiert. Das Wachstum der γ' -Schicht kann durch ein modifiziertes Wachstumsgesetz beschrieben werden, das die ursprüngliche Verzögerung in der Keimbildung von γ' berücksichtigt. Den geschwindigkeitsbestimmende Schritt beim Wachstum der nitrierten Schicht stellt die Diffusion von Stickstoff durch die nitrierte Schicht dar.

Beim Nitrieren einer *rekristallisierten* Fe-1at.% Mo-Legierung tritt (stark) verzögerte Ausscheidung von Mo_2N auf (falls überhaupt): Kein Mo_2N kann in der Matrix gefunden werden, noch nichteinmal nach einer Nitrierzeit von 64 h bei einer Nitriertemperatur von 480 °C. Dies ist eine Konsequenz der großen Volumenfehlpassung zwischen der ferritischen Matrix und der Mo_2N Nitride. Bedingt dadurch, dass die Löslichkeit von Mo in γ' gering ist, wird die γ' -Ausscheidung erschwert. Diese Erschwerungen der Mo- und γ' -Nitrid-Ausscheidungen führen zu einer starken Stickstoffübersättigung der Matrix über einen ausgedehnten Tiefenbereich. Letztendlich könnte die Ausscheidung von γ' auf Kosten des Auflöses von Mo in γ' die bevorzugte Route zur Eliminierung dieser starken Stickstoffübersättigung sein (unter Paragleichgewichtsbedingungen). Die einmal gebildeten γ' -Plättchen wachsen sehr schnell in dem Bereich der starken Stickstoff-Übersättigung. Die hohe Wachstumsrate dieser Plättchen wird, zumindest teilweise, durch Kurzschluss-Diffusion von Stickstoff durch zur Oberfläche benachbarte Ferritkörner hervorgerufen (es entsteht keine geschlossene γ' -Schicht). Die γ' -Plättchen weisen eine Nishiyama-Wassermann Orientierungsbeziehung zur ferritischen Matrix auf. Die Gleichgewichtslöslichkeit von Mo in γ' ist sehr gering. Dies führt zum Auftreten der ε -Phase und einer bis dato unbekannt (Präkursor-) Mo-Nitridphase, neben der γ' -Phase in der Verbindungsschicht während des Nitrierens von rekristallisierten Fe-Mo-Proben, sowie ebenfalls bei den kaltgewalzten Proben zu Beginn des Nitrierens in dem zur Oberfläche benachbarten Teil der Verbindungsschicht. Bei fortschreitendem Nitrieren lösen sich die ε -Phase und die unbekannt (Präkursor-) Phase in dem zur Oberfläche benachbarten Teil der Verbindungsschicht und es bildet sich die Gleichgewichts-Mo-Nitridphase.

7.5.3 Entwicklung der Mikrostruktur und Oberflächen-Eigenstressungen beim Niedertemperatur-Nitrieren einer Fe-3,07at.% Mo-Legierung

Während des Niedertemperatur-Nitrierens einer Fe-3,07at.% Mo-Legierung erfolgt die Ausscheidung von nano-skalierten Plättchen entlang der {100}-Ebenen der ferritischen Matrix. Stark asymmetrische Röntgenbeugungs-Reflexverbreiterung und „Streaks“ entlang $\langle 100 \rangle$ Ferrit-Ebenen in den elektronenmikroskopischen Feinbereichsbeugungsbildern weisen darauf hin, dass die Nitrid-Ausscheidungen in hohem Maße kohärent zur umgebenden Matrix sind, die wiederum aufgrund der Ausscheidungs/Matrix-Fehlpassung tetragonal verzerrt ist. Der Ausscheidungsprozess startet nicht unverzüglich nach der Sättigung der Matrix mit Stickstoff: die Ausbildung einer hohen Härte und hohen Druckeigenstressungen erfolgt sukzessive.

Die Annahme einer Zusammensetzung von Mo_2N für die in hohem Maße kohärenten Nitrid-Plättchen lässt auf eine deutliche Menge an aufgenommenem „Überschuss-Stickstoff“ schließen.

7.5.4 Nitrierverhalten von Maragingstählen: Experiment und Modellierung

Während des Nitrierens von Maragingstählen bilden sich weitestgehend kohärente Nitrid-Ausscheidungen vom Typ Mo_2N , die von einer tetragonal verzerrten Matrix umgeben sind. Diese Nitride rufen einen starken Anstieg der Härte und Druckeigenstressungen hervor. Im Falle des Ausscheidungshärtens der Proben vor dem Nitrieren wird der gesamte Gehalt an Mo beim Ausscheidungshärten als intermetallische Verbindung ausgeschieden, wohingegen bei den lösungsgeglühten Proben der gesamte Gehalt an Mo in der kubischen, martensitischen Matrix gelöst ist. Dies resultiert in einer im Vergleich zu lösungsgeglühten Proben doppelt so hohen Härte vor dem Nitrieren. Als Folge davon weisen die lösungsgeglühten Proben („A“) im Vergleich zu den ausscheidungsgehärteten Proben („B“) nach dem Nitrieren (i) einen stärkeren Härteanstieg und höhere Härtewerte und (ii) höheren Gehalt an

Überschussstickstoff (mobil und immobil) auf. Dies kann wie folgt diskutiert werden. Während des Nitrierens von Proben „A“ kann zu Beginn eine größere Menge an Mo-Nitrid ausgeschieden werden, da Mo ursprünglich substitutionell in der Matrix gelöst ist.

Das sich ausbildende Stickstoff-Konzentrationstiefenprofil in Maragingstählen kann erfolgreich mittels eines kombinierten kinetischen Diffusions- und Ausscheidungsmodells modelliert werden, unter der Voraussetzung der Beachtung des Einflusses des Überschussstickstoffs. Das Modell beruht auf folgenden Fitparametern: der Stöchiomtrikoeffizient des Nitrids (berücksichtigt die Anwesenheit von immobilem, d.h. an der Grenzfläche zwischen Nitrid-Ausscheidung und Matrix adsorbierten Überschuss-Stickstoffs), die Löslichkeit von Stickstoff in der Matrix (berücksichtigt die Anwesenheit von mobilem, d.h. zusätzlich in der gedehnten Matrix gelöstem Überschuss-Stickstoff), den Diffusionskoeffizient von Stickstoff in der Matrix, sowie das Löslichkeitsprodukt der Nitridausscheidungen.

Für den Maragingstahl bestimmte Stickstoff-Absorptionsisothermen erlauben die Unterscheidung zwischen den beim Nitrieren aufgenommenen, verschiedenen Arten von (Überschuss-) Stickstoff und bieten daher Startwerte für die Fitparameter für das kinetische Modell.

Der Diffusionskoeffizient von Stickstoff in dem Maragingstahl ist sehr viel niedriger als für die Stickstoffdiffusion in reinem Ferrit. Dies könnte auf die Mikrostruktur von Maragingstahl zurückgeführt werden (das „Einfangen“ von Stickstoff an z.B. Gitterdefekten) sowie auf das Auftreten eines Labyrinth-Effekts durch die ausgeschiedenen Partikel.

Im lösungsgeglühten Zustand ist die Nitrierkinetik deutlich schneller, verbunden mit einer schnellen Sättigung des gesamten Stickstoffgehalts in der Oberflächenregion. Im Falle von ausscheidungsgehärteten Proben tritt eine gradueller fortschreitende Nitrierreaktion auf, aufgrund des fortschreitenden Auflöses der Partikel der intermetallischen Verbindungen zugunsten der Bildung der Nitrid-Partikel.

Der Gehalt an Überschuss-Stickstoff (mobil und immobil) ist viel höher im Falle von vor dem Nitrieren lösungsgeglühten Proben, was auf das, im Vergleich zu

ausscheidungsgehärteten Proben, Auftreten von feineren und kohärenteren Nitridplättchen schließen lässt.

Im Hinblick auf die technologische Anwendung empfiehlt sich eine direkte Nitrierung im lösungsgeglühten Zustand, d.h. ohne vorherige Ausscheidungshärtung: deutlich mehr Stickstoff wird in kürzerer Zeit aufgenommen und eine höhere Härte wird erzielt.

REFERENCES

- [1] M.H. Biglari, C.M. Brakman, E.J. Mittemeijer, *Phil. Mag. A* 72, (1995), p. 1281.
- [2] S.S. Hosmani, R.E. Schacherl, L. Litynska-Dobrzynska, E.J. Mittemeijer, *Phil. Mag.* 88, (2008), p. 2411.
- [3] S.S. Hosmani, R.E. Schacherl, E.J. Mittemeijer, *Acta Mater.* 53, (2005), p. 2069.
- [4] S. Meka, S.S. Hosmani, A.R. Clauss, E.J. Mittemeijer, *Int. J. Mater. Res.* 99, (2008), p. 808.
- [5] A.R. Clauss, E. Bischoff, S.S. Hosmani, R.E. Schacherl, E.J. Mittemeijer, *Metall. Mater. Trans. A* 40A, (2009), p. 1923.
- [6] K.S. Jung, S.R. Meka, R.E. Schacherl, E. Bischoff, E.J. Mittemeijer, *Metall. Mater. Trans. A* 43A, (2012), p. 934.
- [7] K.S. Jung, R.E. Schacherl, E. Bischoff, E.J. Mittemeijer, *Surf. Coat. Technol.* 204, (2010), p. 1942.
- [8] E.J. Mittemeijer, J.T. Slycke, *Surf. Eng.* 12, (1996), p. 152.
- [9] E.J. Mittemeijer, M.A.J. Somers, *Surf. Eng.* 13, (1997), p. 483.
- [10] E. Lehrer, *Z. Elektrochem.* 36, (1930), p. 383.
- [11] R. Hoffmann, E.J. Mittemeijer, M.A.J. Somers, *HTM* 51, (1996), p. 7.
- [12] H. Wriedt, N. Gokcen, R. Nafziger, *Journal of Phase Equilibria* 8, (1987), p. 355.
- [13] H.H. Podgurski, H.E. Knechtel, *T Metall Soc Aime* 245, (1969), p. 1595.
- [14] H.H. Podgurski, R.A. Oriani, F.N. Davis, J.C.M. Li, Y.T. Chou, *T Metall Soc Aime* 245, (1969), p. 1603.
- [15] P.M. Hekker, H.C.F. Rozendaal, E.J. Mittemeijer, *J. Mater. Sci.* 20, (1985), p. 718.
- [16] S.S. Hosmani, R.E. Schacherl, E.J. Mittemeijer, *Mater. Sci. Technol.* 21, (2005), p. 113.
- [17] S.S. Hosmani, R.E. Schacherl, E.J. Mittemeijer, *J. Mater. Sci.* 43, (2008), p. 2618.
- [18] R.E. Schacherl, P.C.J. Graat, E.J. Mittemeijer, *Z. Metallkd.* 93, (2002), p. 468.
- [19] R.E. Schacherl, P.C.J. Graat, E.J. Mittemeijer, *Metall. Mater. Trans. A* 35A, (2004), p. 3387.
- [20] S.S. Brenner, S.R. Goodman, *Scr. Metall.* 5, (1971), p. 865.
- [21] J.H. Driver, J.M. Papazian, *Acta Metall.* 21, (1973), p. 1139.

- [22] J.H. Driver, D.C. Unthank, K.H. Jack, *Phil. Mag.* 26, (1972), p. 1227.
- [23] K.H. Jack, *Heat Treatment 73 The Metals Society Book* 163, (1975), p. 39.
- [24] J.D. Kamminga, T.P.C. Klaver, K. Nakata, B.J. Thijsse, G.C.A.M. Janssen, *J. Comput. Aided Mater. Des.* 10, (2003), p. 1.
- [25] A. Krawitz, *Scr. Metall.* 11, (1977), p. 117.
- [26] R. Wagner, S.S. Brenner, *Acta Metall.* 26, (1978), p. 197.
- [27] D.H. Jack, *Acta Metall.* 24, (1976), p. 137.
- [28] H.H. Podgurski, F.N. Davis, *Acta Metall.* 29, (1981), p. 1.
- [29] D.S. Rickerby, S. Henderson, A. Hendry, K.H. Jack, *Acta Metall.* 34, (1986), p. 1687.
- [30] S.S. Hosmani, R.E. Schacherl, E.J. Mittemeijer, *Acta Mater.* 54, (2006), p. 2783.
- [31] M.A.J. Somers, R.M. Lankreijer, E.J. Mittemeijer, *Phil. Mag. A* 59, (1989), p. 353.
- [32] E. Macherauch, V. Hauk (editors). *Origin, measurement and evaluation of residual stresses. Residual stresses in science and technology.*, Vol. 1, DGM Informationsgesellschaft m.b.H., Oberursel, 1987.
- [33] P.J. Withers, H.K.D.H. Bhadeshia, *Mater. Sci. Technol.* 17, (2001), p. 355.
- [34] E. Mittemeijer, *Journal of Heat Treating* 3, (1983), p. 114.
- [35] R.F. Decker, S. Floreen, *Maraging Steels: Recent Developments and Applications*, TMS-AIME, Warrendale, 1988.
- [36] S. Floreen, *Metall. Rev.* 13, (1968), p. 13.
- [37] J.B. Lecomte, C. Servant, G. Cizeron, *J. Mater. Sci.* 20, (1985), p. 3339.
- [38] W. Sha, A. Cerezo, G.D.W. Smith, *Metall. Trans. A* 24, (1993), p. 1221.
- [39] M. Fukamachi, Y. Kawabe, K. Nakazawa, S. Muneki, *J. Jpn. Inst. Met.* 47, (1983), p. 237.
- [40] Mihalisi.Jr, C.G. Bieber, *Jom-J Min Met Mat S* 18, (1966), p. 1033.
- [41] G.P. Huffman, H.H. Podgurski, *Acta Metall.* 23, (1975), p. 1367.
- [42] H.J. Grabke, *Ber. Bunsenges. Physik. Chem.* 72, (1968), p. 533.
- [43] D. Liedtke, U. Baudis, J. Boßlet, U. Huchel, H. Klümper-Westkamp, W. Lerche, H.J. Spies, *Wärmebehandlung von Eisenwerkstoffen Nitrieren und Nitrocarburieren*, 3rd ed., Expert Verlag, Renningen, 2006.
- [44] M.A.J. Somers, *Heat Treat. Met.* 27, (2000), p. 92.

- [45] N.E.V. Diaz, S.S. Hosmani, R.E. Schacherl, E.J. Mittemeijer, *Acta Mater.* 56, (2008), p. 4137.
- [46] V.D. Yakhnina, F.Z. Izmailov, *Met. Sci. Heat Treat.* 18, (1976), p. 480.
- [47] D.L. Speirs, W. Roberts, P. Grieveson, K.H. Jack: 425, I.S.I, Sheffield, International Symposium on Metallurgical Chemistry, 1971
- [48] B. Gault, F. Danoix, K. Hoummada, D. Mangelinck, H. Leitner, *Ultramicroscopy* 113, (2012), p. 182.
- [49] M.H. Biglari, C.M. Brakman, E.J. Mittemeijer, S. van der Zwaag, *Metall. Mater. Trans. A* 26, (1995), p. 765.
- [50] J.L. Pouchou, F. Pichoir, *Rech. Aerosp.*, (1984), p. 167.
- [51] JCPDS-International Centre for Diffraction Data, PCPDFWIN. 2002.
- [52] E.J. Mittemeijer, *Fundamentals of Materials Science*, Springer Verlag, Heidelberg, Berlin, 2010.
- [53] W.G. Burgers, *Physica* 1, (1934), p. 561.
- [54] J.G.M. van Berkum, R. Delhez, T.H. de Keijser, E.J. Mittemeijer, *Acta Crystallogr., Sect. A* 52, (1996), p. 730.
- [55] L. Cheng, A. Bottger, T.H. de Keijser, E.J. Mittemeijer, *Scr. Metall. Mater.* 24, (1990), p. 509.
- [56] W.B. Pearson, *A Handbook of Lattice Spacings and Structures of Metals and Alloys*, Vol. 1, Pergamon Press, Oxford, 1958.
- [57] I. Manna, S.K. Pabi, W. Gust, *Int. Mater. Rev.* 46, (2001), p. 53.
- [58] D.B. Williams, E.P. Butler, *Int. Met. Rev.* 3, (1981), p. 153.
- [59] R. Danoix, L. Legras, B. Hannoyer, J. Dulcy, F. Danoix: 351, The Minerals, Metals and Materials Society, Phoenix, AZ, USA, PTM-international conference on solid-solid transformations in inorganic materials, 2005
- [60] J.R. Davis (editor) *ASM handbook*, Vol. 4, ASM International, Metals Park, Ohio, 1991.
- [61] E.J. Mittemeijer, J.T. Slycke, *Heat Treat. Met.* 23, (1996), p. 67.
- [62] S.R. Meka, E. Bischoff, R.E. Schacherl, E.J. Mittemeijer, *Phil. Mag.* 92, (2012), p. 1083.
- [63] M.A.J. Somers, E.J. Mittemeijer, *Metall. Mater. Trans. A* 26, (1995), p. 57.

- [64] R.A. Greff, W.D. Leslie, E.A. Setzkorn, J. Am. Oil Chem. Soc. 41, (1964), p. 63.
- [65] H. Selg, E. Bischoff, R. Schacherl, T. Waldenmaier, E.J. Mittemeijer, Metall. Mater. Trans. A submitted, (2012).
- [66] K. Schwerdtfeger, P. Grieveson, E.T. Turkdogan, T Metall Soc Aime 245, (1969), p. 2461.
- [67] J. Crank, *The Mathematics of Diffusion*, 2nd ed., Oxford University Press, Oxford, 1975.
- [68] T. Woehrle, A. Leineweber, E.J. Mittemeijer, Metall. Mater. Trans. A submitted, (2012).
- [69] H. Du, J. Agren, Metall. Mater. Trans. A 27, (1996), p. 1073.
- [70] B.J. Kooi, M.A.J. Somers, E.J. Mittemeijer, Metall. Mater. Trans. A 27, (1996), p. 1063.
- [71] H. Du, J. Agren, Z. Metallkd. 86, (1995), p. 522.
- [72] T. Liapina, A. Leineweber, E.J. Mittemeijer, Metall. Mater. Trans. A 37A, (2006), p. 319.
- [73] H.C.F. Rozendaal, E.J. Mittemeijer, P.F. Colijn, P.J. Van der Schaaf, Metall. Trans. A 14, (1983), p. 395.
- [74] J.D. Fast, M.B. Verrijp, J Iron Steel I 176, (1954), p. 24.
- [75] S.S. Hosmani, R.E. Schacherl, E.J. Mittemeijer, Int. J. Mater. Res. 97, (2006), p. 1545.
- [76] S.S. Hosmani, R.E. Schacherl, E.J. Mittemeijer, J. Mater. Sci. 44, (2009), p. 520.
- [77] J. Takada, Y. Oizumi, H. Miyamura, H. Kuwahara, S. Kikuchi, Oxid. Met. 26, (1986), p. 19.
- [78] H. Miyamura, J. Takada, H. Kuwahara, S. Kikuchi, J. Mater. Sci. 21, (1986), p. 2514.
- [79] S. Meka, R. Schacherl, E. Bischoff, E.J. Mittemeijer, HTM J. Heat Treatm. Mat. 66, (2011), p. 103.
- [80] H. Selg, E. Bischoff, R. Schacherl, J. Schwarzer, E.J. Mittemeijer, HTM J. Heat Treatm. Mat. 2, (2011), p. 5.
- [81] M. Nikolussi, A. Leineweber, E.J. Mittemeijer, Phil. Mag. 90, (2010), p. 1105.
- [82] A.L. Schwab, J.P. Meijaard: *How to draw Euler angles and utilize Euler*

parameters, ASME, 2006

- [83] Z. Nishiyama, Science Reports of the Tohoku Imperial University, 23, (1934), p. 637.
- [84] A. Wassermann, Ber Dtsch Chem Ges 66, (1933), p. 1392.
- [85] X.C. Xiong, A. Redjaimia, M. Goune, J. Mater. Sci. 44, (2009), p. 632.
- [86] U. Dahmen, P. Ferguson, K.H. Westmacott, Acta Metall. 35, (1987), p. 1037.
- [87] E.C. Bain, T Am I Min Met Eng 70, (1924), p. 21.
- [88] D.L. Speirs. precipitation in iron-molybdenum-nitrogen alloys. Ph.D. Newcastle: University of Newcastle upon Tyne, 1969.
- [89] U. Welzel, E.J. Mittemeijer, European Powder Diffraction Epdic 8 443-4, (2004), p. 131.
- [90] U. Welzel, E.J. Mittemeijer, J. Appl. Phys. 93, (2003), p. 9001.
- [91] Landolt-Börnstein (editor) *The Landolt-Börnstein Database*, Physical Chemistry IV, Springer Materials, 1995.
- [92] J.E. Lowther, J. Alloys Compd. 364, (2004), p. 13.
- [93] H.J. Goldschmidt, J. Helmut, *Interstitial Alloys*, London, 1967.
- [94] F. Cajner, D. Landek, S. Solic, H. Cajner, Surf. Eng. 22, (2006), p. 468.
- [95] K. Shetty, S. Kumar, P.R. Rao, Surf. Coat. Technol. 203, (2009), p. 1530.
- [96] J.L. Meijering, *Advances in Materials Research*, Wiley-Interscience, New York, 1971.
- [97] M.H. Biglari, C.M. Brakman, E.J. Mittemeijer, S. van der Zwaag, Phil. Mag. A 72, (1995), p. 931.
- [98] M.M. Yang, A.D. Krawitz, Metall. Trans. A 15, (1984), p. 1545.
- [99] K. Bongartz, D.F. Lupton, H. Schuster, Metall. Trans. A 11, (1980), p. 1883.
- [100] K. Bongartz, W.J. Quadackers, R. Schulten, H. Nickel, Metall. Trans. A 20, (1989), p. 1021.
- [101] Y. Sun, T. Bell, Mat Sci Eng a-Struct 224, (1997), p. 33.
- [102] U. Welzel, J. Ligot, P. Lamparter, A.C. Vermeulen, E.J. Mittemeijer, J. Appl. Crystallogr. 38, (2005), p. 1.
- [103] D. Gerlich, R.B. Roberts, G.K. White, R. Tainsh, J. Mater. Sci. 25, (1990), p. 2249.
- [104] P.F. Colijn, E.J. Mittemeijer, H.C.F. Rozendaal, Z. Metallkd. 74, (1983), p. 620.

- [105] A. Engstrom, L. Hoglund, J. Agren, Metall. Mater. Trans. A 25, (1994), p. 1127.
- [106] X.F. Hu, Q.L. Ge, Z.L. Wu, Acta Metall. Mater. 41, (1993), p. 1625.
- [107] E.I. Mittemeijer, Härterei-Technische Mitteilungen 36, (1981), p. 57.
- [108] P.B. Friehling, F.W. Poulsen, M.A.J. Somers, Z. Metallkd. 92, (2001), p. 589.
- [109] I. Barin, *Thermochemical Data of Pure Substances*, VCH, Weinheim, Basel, 1995.

Danksagung

Die vorliegende Dissertation entstand im Zeitraum von März 2009 bis August 2012 am Institut für Materialwissenschaft der Universität Stuttgart, sowie am Max-Planck-Institut für Intelligente Systeme (ehemals Max-Planck-Institut für Metallforschung), Stuttgart, in Kooperation mit der Robert Bosch GmbH, Zentralbereich Forschung und Vorausbentwicklung, Schwieberdingen. Nachfolgend möchte ich allen danken, die zum Gelingen dieser Arbeit beigetragen haben.

An erster Stelle gebührt mein Dank meinem Doktorvater, Herrn Prof. Dr. Ir. E.J. Mittemeijer für das mir entgegengebrachte Vertrauen, ein solch breitgefächertes und interessantes Thema bearbeiten zu dürfen. Sein herausragendes wissenschaftliches Interesse und seine Begeisterungsfähigkeit haben mich immer wieder aufs Neue fasziniert und motiviert. Für die zielführenden und inspirierenden Diskussionen, die dem Gelingen dieser Arbeit in großem Maße dienlich waren, möchte ich ihm recht herzlich danken.

Herrn Prof. Dr. J. Bill möchte ich für die freundliche Übernahme des Mitberichts danken, sowie Herrn Prof. Dr. T. Schleid für seine Bereitschaft, den Prüfungsvorsitz zu übernehmen.

Für die Anfertigung einer Dissertation ist die Unterstützung durch Kollegen unerlässlich. Hierfür möchte ich der gesamten Abteilung Mittemeijer meinen Dank aussprechen. Namentlich erwähnen möchte ich insbesondere meinen langjährigen Bürokollegen Thomas Wöhrle, sowie Sairam, Kyung Sub, Gayatri, Silke, Bastian, Katharina und Jendrik, mit deren Hilfe wissenschaftliche und auch kulturelle Fragestellungen im Rahmen unserer regelmäßigen Meetings erörtert wurden.

Ein weiterer Dank gebührt meinem täglichen Betreuer, Herrn Dr. R. Schacherl, für seine Unterstützung während meiner Zeit als Doktorand in seiner Arbeitsgruppe, sowie Herrn Dr. E. Bischoff und Herrn Dr. A. Leineweber für ihre stetige Diskussionsbereitschaft.

Des Weiteren möchte ich Herrn Dr. G. Eckstein für die freundliche Aufnahme in seine Abteilung bei der Robert Bosch GmbH danken. Meinen Betreuern Seitens der Robert Bosch GmbH, Herrn Dr. J. Schwarzer und insbesondere Herrn Dr. T. Waldenmaier, der mir durch seine unermüdliche Diskussions- und Hilfsbereitschaft helfend zur Seite stand, gebührt mein außerordentlicher Dank.

Zu guter Letzt gebührt den wichtigsten Personen in meinem Leben, meiner Freundin Silke, sowie meinen Eltern und meiner Schwester für die mir entgegengebrachte Unterstützung in jeglicher Form, sowie den durch sie stets erfahrenen Rückhalt ein ganz besonderer, nicht in Worte fassbarer Dank.

Curriculum Vitae

Persönliche Daten

Name	Holger Selg
geboren am	11. September 1983 in Riedlingen/Donau
Nationalität	Deutsch

Schulbildung

1990 - 1994	Grundschule Langenenslingen
1994 - 2003	Kreisgymnasium Riedlingen, mit dem Abschluss der allgemeinen Hochschulreife

Universitäre Ausbildung

2003-2008	Studium der Werkstoffwissenschaft, Universität Stuttgart
2008-2009	Diplomarbeit am Max-Planck-Institut für Metallforschung und Institut für Materialwissenschaft, Universität Stuttgart. Thema der Diplomarbeit: „ <i>Microstructure of severly plastically deformed metals</i> “

Promotion

März 2009 – August 2012	Promotion zum Dr. rer. nat. bei der Robert-Bosch GmbH in Kooperation mit dem Max-Planck-Institut für Intelligente Systeme (ehemals Max-Planck-Institut für Metallforschung), Abteilung von Prof. Dr. Ir. E.J. Mittemeijer und dem Institut für Materialwissenschaft, Universität Stuttgart. Thema der Promotion: „ <i>Nitriding of Fe-Mo Alloys and Maraging Steel: Structure, Morphology and Kinetics of Nitride Precipitation</i> “
-------------------------	---------------------------------------------------------------------------------------------------------------------------------------------------------------------------------------------------------------------------------------------------------------------------------------------------------------------------------------------------------------------------------------------------------------------------------------

Erklärung über die Eigenständigkeit der Dissertation

Ich versichere, dass ich die vorliegende Arbeit mit dem Titel
„Nitriding of Fe-Mo Alloys and Maraging Steel: Structure, Morphology and Kinetics of
Nitride Precipitation“

selbständig verfasst und keine anderen als die angegebenen Quellen und Hilfsmittel
benutzt habe; aus fremden Quellen entnommene Passagen und Gedanken sind als
solche kenntlich gemacht.

Name: _____

Unterschrift: _____

Datum: _____